Current issues with modelling convective storms in HARMONIE

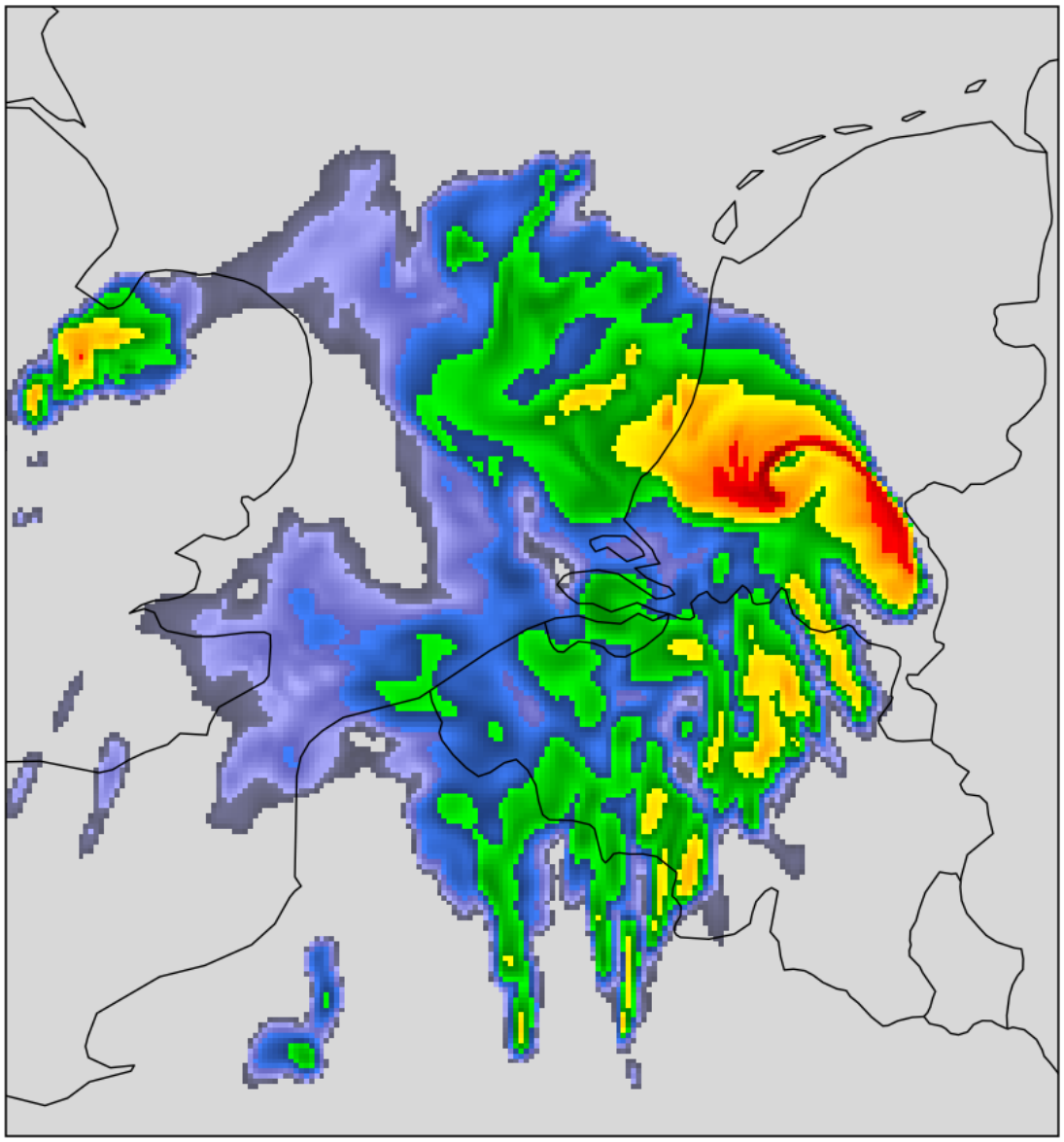

Bram van't Veen

Supervisors
Sander Tijm (KNMI)
Aarnout J. van Delden (UU)

Koninklijk Nederlands
Meteorologisch Instituut
Ministerie van Infrastructuur en Milieu

Utrecht University

Abstract

The performance of HARMONIE on simulating convective storms has been studied by comparing simulated and observed three-dimensional radar reflectivity fields and satellite images. This comparison was performed over two domains; one over the Netherlands and one over the Central US. Case studies lead to a list of five (potential) issues. Most important are the severe underestimation of the number of simulated shallow showers, a potential problem with initiating severe thunderstorms under the turbulence scheme HARATU, and a large underestimation (overestimation) of the area covered by weak (intense) precipitation.
The underestimation of the number of shallow showers is related to the shallow convection scheme, and it has been shown that this scheme adjusts vertical temperature and dew point profiles in a way that is unfavourable for initiating showers. For the potential issue with initiating severe thunderstorms it has been shown that using HARATU leads to a drier boundary layer and steeper temperature lapse rates just above the boundary layer, effects that influence initiation of storms.
Results of a detailed analysis of distributions of observed and simulated radar reflectivity confirm that the model greatly underestimates the area covered by relatively weak stratiform precipitation, and greatly overestimates the area covered by the more intense convective precipitation. It is shown that the model's horizontal resolution has very little effect on these distributions, suggesting that improvement should mainly come from improvement of the microphysics. Literature suggests that a better representation of convective regions within storms is critical for improving on this issue, as is switching to a double-moment microphysics scheme.

Contents

Chapter 1

Introduction

The HARMONIE (HIRLAM-ALADIN Research on Mesoscale Operational NWP in Euromed) model is used operationally by KNMI as a basis for weather forecasts. Its horizontal resolution of 2.5 km allows the model to explicitly resolve deep convection, e.g. thunderstorms, making it an important basis for the operational prediction of thunderstorms by KNMI. Except for producing dangerous lightning, thunderstorms can be accompanied by damaging winds, hail and tornadoes, making accurate warnings very important. Because more accurate model forecasts of convective storms would greatly benefit the warning process, a comprehensive evaluation of the model's performance on simulating convective storms is desired, as it forms the basis for further improvement.

During years of using the model, a few issues with modelling of convection have already been noted. Tijm (2018) presented an overview of these issues, showing a case in which the model greatly underestimated the amount of shallow showers over the Netherlands and surroundings during cold air outbreaks over the North Sea, noting that it might be related to the influence of a parameterization of shallow convection. Another case showed a potential second problem, with a lack of initiation of an intense (supercell) storm when using a new (the current) turbulent scheme, which was in fact simulated when using the previous turbulence scheme. Finally, running the model for an additional case under several configurations of the model physics showed the (strong) influence that the model physics has on the development and evolution of convective storms. These findings formed the basis for further evaluation of the model performance in this new work.

This report is organized as follows. Chapter 2 provides a description of the HARMONIE model, with emphasis on the relevant model physics. It also includes a description of a few important updates from recent years, and an overview of the model configurations that are used in the comparison with observed convection. Chapter 3 describes in detail the basis for comparing simulated with observed convection. The main quantity that will be used for this comparison is the equivalent reflectivity factor (short; reflectivity), which can be derived from measurements by precipitation radars, and can also be simulated from model output of hydrometeor contents. Next, chapter 4 describes the observational data that has been used, together with two other methods to compare model with observations or models among themselves. These methods are comparing (simulated) satellite images and comparing box-averaged skew-T log-P diagrams. Chapter 5 provides an overview of all (potential) issues that have been found in a more detailed examination of cases than what had been performed at the time of Tijm (2018). In addition, potential causes have been found for some of these issues, and these are described too in this chapter. Given that thus far the presence of these issues has been based on model runs for just a few cases, a more comprehensive analysis of some issues is desired. This is the topic of chapter 6, where results of a comprehensive analysis of simulated precipitation patterns are presented.

Important for a detailed examination of model output was the development of an interactive viewer for the output, which formed the starting point of this project. It supports interactive drawing of lines to request vertical cross sections, and drawing of points or rectangular boxes to request (box-averaged) skew-T log-P diagrams. It has been used to generate a number of the figures that appear in this report, for instance figure 3.11.

Chapter 2

HARMONIE model setup

2.1 Background

The HARMONIE-AROME model is developed, maintained and validated as part of the shared ALADIN-HIRLAM system by a collaboration of 26 countries in Europe and northern Africa (Bengtsson et. al., 2017). The HIRLAM research program was initiated in 1985 and currently consists of the National Meteorological Services of 10 countries, including the Netherlands. The ALADIN collaboration started in 1991, and currently has 16 member countries. On 5 December 2005, a cooperation agreement between the ALADIN and HIRLAM consortia was signed with the primary objective of providing the members with a state-of-the-art NWP model for short- and very-short-range forecasting including nowcasting, for both research and development activities and operational usage. In 2014 the ALADIN and HIRLAM consortia further agreed on the formation of a single united consortium by 2020, and are currently working on this.
The development of the AROME model was started by the ALADIN consortium, and there are currently two main setups of the model; HARMONIE-AROME (hereafter referred to as HARMONIE) and AROME-France (Seity et. al., 2011). These setups use the same dynamical core, and differ mainly in their physical parameterizations.

2.2 Basic configuration

HARMONIE uses the nonhydrostatic core developed by the ALADIN consortium, based on the fully compressible Euler equations (Bengtsson et. al., 2017). The equations are discretized in time and space, using a semi-Lagrangian advection scheme on an A grid and a semi-Implicit two-time-level scheme, with spectral representation of most prognostic variables based on a double Fourier decomposition. With the current operationally used settings, HARMONIE obtains its boundary conditions from the ECMWF model. Sixty-five levels are used in the vertical, with the model top at 10 hPa and the lowest level at 12 m AGL. A hybrid vertical coordinate is used, with a pressure coordinate system used for the upper levels, and a sigma coordinate system for the lower levels. The horizontal resolution is 2.5 km, with a model time step of 75 s.

2.3 Model physics

This section describes the current state of model physics, with emphasis on the microphysics, turbulence and shallow convection schemes.

2.3.1 Radiation

The default shortwave radiation scheme is the Morcrette scheme from ECMWF, that uses 6 spectral intervals. For longwave radiation, the default scheme contains 16 spectral bands and uses the Rapid Radiative Transfer Model. Full radiation calculations are performed every 15 minutes.

2.3.2 Surface

Surface physics are simulated by the scheme SURFEX, which is developed mainly by Météo France in cooperation with the scientific community. Each grid box is represented by four surface tiles; sea or ocean, lakes, urban areas and nature (soil and vegetation). Each tile is modeled with a specific surface model, and the total

flux of the grid box is computed as a weighted sum of the individual fluxes, with weights being given by the grid cell fractions occupied by the tiles.

2.3.3 Turbulence

HARMONIE uses the HARATU (HARMONIE with RACMO Turbulence) turbulence scheme (Bengtsson et. al., 2017), originally developed by Lenderink and Holtslag (2004) for use in the regional climate model RACMO. It uses a framework with a prognostic equation for the turbulent kinetic energy (TKE), combined with a diagnostic mixing length scale.
This length scale formulation essentially consists of two parts: one for stable conditions and one for near-neutral to convective conditions. For near-neutral to convective conditions the mixing length scale is computed by averaging over two length scales; an 'upward' and a 'downward' length scale. The upward (downward) length scale is computed by integrating upward (downward) over a function that depends on the local stability, up to the upper (lower) boundary of the mixing domain.
For (strongly) stable conditions, a generally accepted form based on local stability and turbulent kinetic energy is used.

2.3.4 Shallow convection

With its 2.5-km horizontal resolution, HARMONIE is able to rougly resolve deep convection explicitly (Bengtsson et. al., 2017). However, shallow convection still needs to be parameterized. In HARMONIE this is done in an eddy-diffusivity mass-flux framework, of which the eddy diffusivity part (turbulence) part is described by the turbulence scheme HARATU. The shallow convection scheme is applied until a cloud reaches a maximum depth of 4 km.

For the mass flux, a dual mass-flux approach is used in which two updrafts are distinguished; a dry updraft that never reaches the condensation level, and a moist updraft that condenses and becomes a cloud. As indicated in figure 2.1, three different convective boundary layer regimes are considered. The convective upward mass flux inside the updrafts is described by

$$\frac{\partial M}{\partial z} = (\varepsilon - \delta)M, \tag{2.1}$$

where M is the convective vertical mass flux, ε the fractional entrainment and δ the fractional detrainment. Entrainment describes inflow of environmental air into the updraft (diluting the updraft), whereas detrainment describes outflow of updraft air into the environment.
The profile of entrainment is defined to be solely dependent on the actual and inversion height, and is sketched in figure 2.1 for the three convective boundary layer regimes.
For detrainment, a formulation is used that is able to capture the order of magnitude variations in detrainment due to cloud layer depth. Further, the influence of environmental conditions on detrainment is taken into account by making detrainment dependent on a parameter χ_c, that increases with increasing relative humidity and buoyancy excess of the updraft.

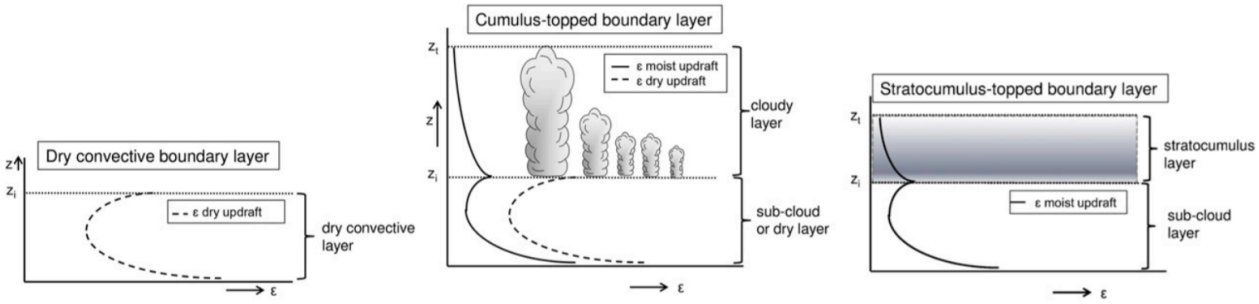

Figure 2.1: Schematic diagram of the three convective boundary layer regimes and their corresponding entrainment formulations. From Bengtsson et. al (2017).

2.3.5 Microphysics

Microphysical processes are described by the single-moment ICE3 bulk microphysics scheme (Pinty and Jabouille 1998; Lascaux et al. 2006). Liquid processes are parameterized mainly by the Kessler scheme for warm clouds (Kessler 1969), but autoconversion of cloud droplets into raindrops is prescribed by the Kogan

autoconversion parameterization (Khairoutdinov and Kogan 2000). For ice, three solid hydrometeor species are included in the ICE3 scheme, i.e. cloud ice, snow and a combination of graupel and hail. Inclusion of an extra prognostic variable for hail is still in research mode (ICE4).

Hydrometeor size distributions are prescribed to be generalized Gamma distributions (Mascart and Bougeault 2011):

$$n(D) = N \cdot g(D), \quad g(D) = \frac{\alpha}{\Gamma(\nu)} \lambda^{\alpha\nu} D^{\alpha\nu-1} \exp\left(-(\lambda D)^{\alpha}\right). \tag{2.2}$$

Here N denotes the total number concentration for the hydrometeor class, D denotes the maximum particle dimension, and $n(D)$ represents the number concentration of particles with maximum particle dimension D. Taking $\alpha = 1$ and $\nu = 1$ leads to a Marshall-Palmer distribution, which is used for raindrops. Values for α and ν for the other hydrometeor classes are given in table 2.1, which also lists values for the parameters that follow below. An expression for the slope parameter λ is given in (2.10).

For future reference, moments M of these generalized Gamma distributions are given by

$$M(p) = \int_0^{\infty} D^p g(D) dD = \frac{G(p)}{\lambda^p}, \quad G(p) = \frac{\Gamma(\nu + p/\alpha)}{\Gamma(\nu)}. \tag{2.3}$$

Power law relationships are used to relate the particle mass to the maximum particle dimension D as

$$m(D) = aD^b, \tag{2.4}$$

and the terminal particle fall speeds are prescribed by

$$v(D) = cD^d (\rho_{d0}/\rho_d)^{0.4}, \tag{2.5}$$

where ρ_d is the density of dry air, and ρ_{d0} a reference air density.

The hydrometeor mixing ratio can be calculated as

$$r = \frac{1}{\rho} \int_0^{\infty} m(D) n(D) dD = \frac{aNM(b)}{\rho}. \tag{2.6}$$

The total number concentration has to be obtained by another means. Caniaux (1993) established based on a compilation of various published experimental observations that for precipitating ice, N can be related to the slope parameter λ as

$$N = C\lambda^x. \tag{2.7}$$

By taking $C = N_0$ and $x = -1$ we can also apply this relation to rain drops, as substitution in (2.2) leads to the classical Marshal-Palmer distribution used for rain drops;

$$n(D) = N_0 \exp(-\lambda D). \tag{2.8}$$

For cloud ice and cloud water, N has to be diagnosed by another means.

By combining (2.3) and (2.6) we can find an expression for λ in terms of ρr and N as

$$\lambda = \left(\frac{\rho r}{G(b) a N}\right)^{-\frac{1}{b}}. \tag{2.9}$$

For the precipitating particles, i.e. rain, snow and graupel, using (2.7) allows us to write this as

$$\lambda = \left(\frac{\rho r}{aCG(b)}\right)^{\frac{1}{x-b}}. \tag{2.10}$$

For ice particles, experimental evidence and a sensitivity study have lead to relate C and x by (Caniaux 1993)

$$\log_{10} C = -3.55x + 3.89. \tag{2.11}$$

Generalized Gamma distributions for the three precipitating hydrometeor classes are shown in figures 2.2-2.4, as a function of the hydrometeor content ρr.

Table 2.1: Values for the set of parameters used to describe each hydrometeor class (from Mascart and Bougeault 2011).

Parameters	r_i	r_s	r_g	r_r	r_c
α	3	1	1	1	3 on sea; 1 on land.
ν	3	1	1	1	1 on sea; 3 on land.
a	0.82	0.02	19.6	524	524
b	2.5	1.9	2.8	3	3
c	800	5.1	124	842	$3.2 \cdot 10^7$
d	1.00	0.27	0.66	0.8	2
C		5	$5 \cdot 10^5$	$8 \cdot 10^6$	
x		1	-0.5	-1	

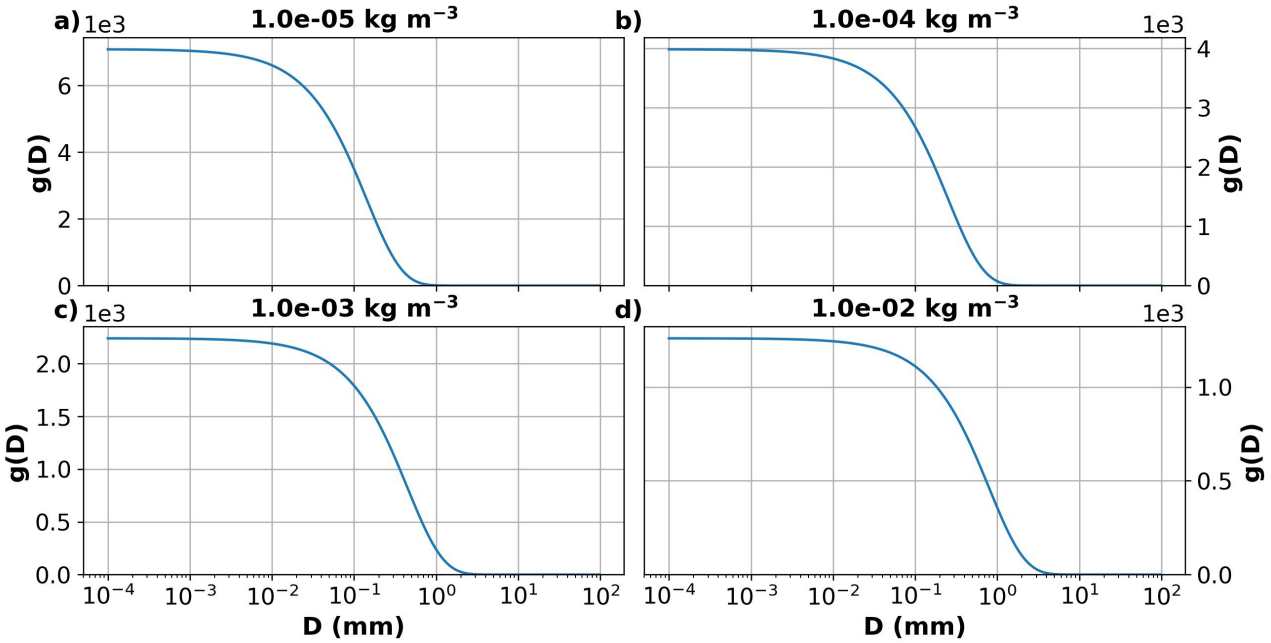

Figure 2.2: generalized Gamma distributions g (eq. 2.2) as a function of the maximum particle dimension D using the parameter values given in table 2.1) for values of rain content (ρr) given by a) 10^{-5}, b) 10^{-4}, c) 10^{-3} and d) 10^{-2} kg/m^3.

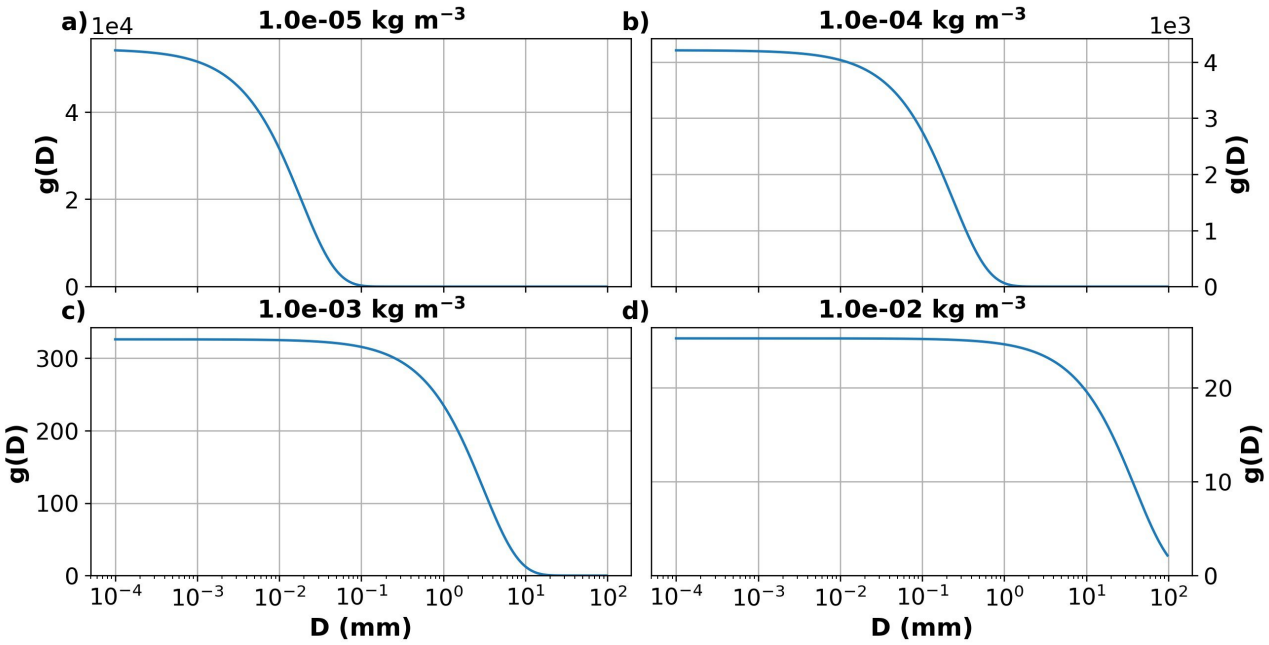

Figure 2.3: As in figure 2.2, but for snow.

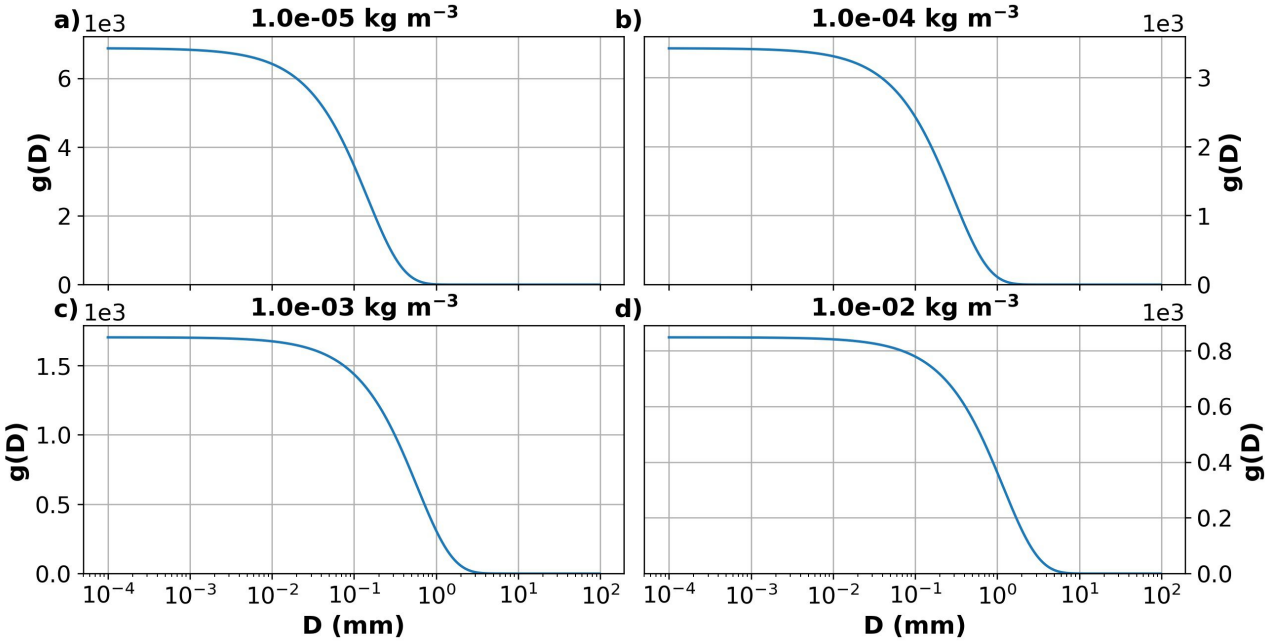

Figure 2.4: As in figure 2.2, but for graupel.

The evolution of the hydrometeor species is governed by a lot of processes, that can be separated into warm processes, involving only liquid water, and cold processes, involving (also) ice. An overview of all these processes is given in figure 2.5, with a corresponding description provided in table 1 in appendix A.

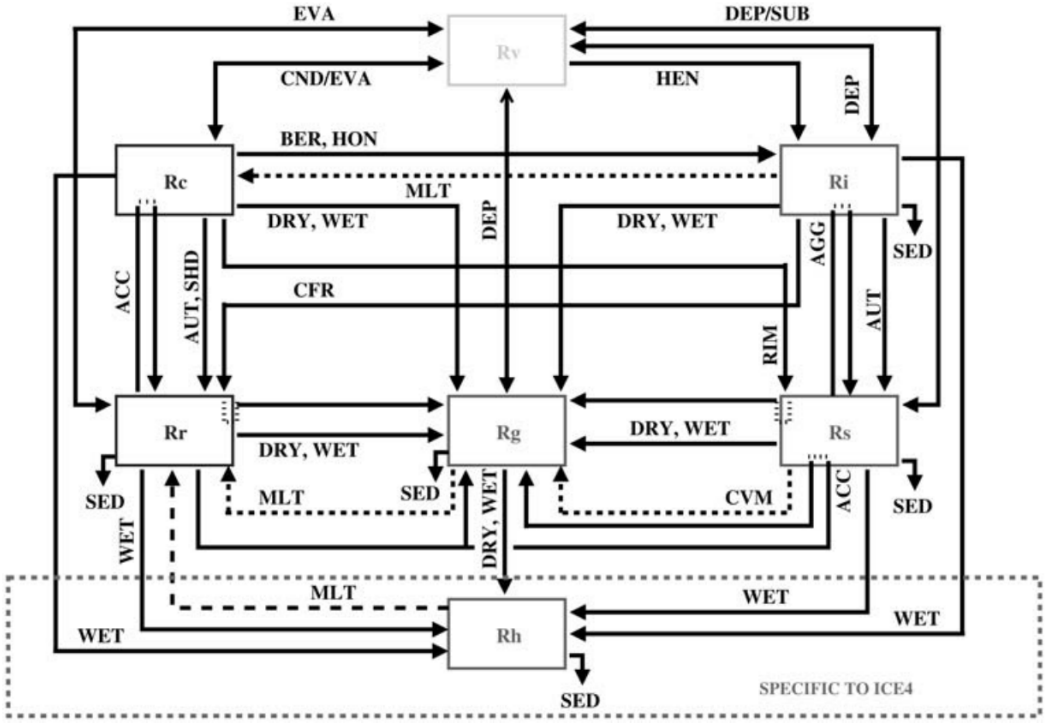

Figure 2.5: Processes determining the evolution of the hydrometeor mixing ratios, as included in the HARMONIE microphysics scheme. R_v, R_c, R_r, R_i, R_s, R_g, and R_h refer to the mixing ratios of water vapour, cloud droplets, raindrops, pristine ice, snow/aggregates, graupel, and hail respectively. Processes specific to ICE4, with hail as an extra prognostic variable, are drawn at the bottom. Table 1 in appendix A provides a description of all processes in ICE3 that convert hydrometeor species. SED indicates sedimentation of hydrometeors. From Lascaux et. al. (2006).

2.4 Important recent upgrades of model physics

Model physics have changed in a few important ways in recent years, when moving from cycle 36 towards the most recent cycle 40h1.1.1. The most important changes are the introduction of a new turbulence scheme HARATU and an upgrate of the cloud microphysics. Both are described in more detail below.

2.4.1 Introduction of HARATU

The new turbulence scheme HARATU has been introduced to solve issues with the representation of the boundary layer, i.e. too low boundary layers heights and cloud base, and too much cloud cover and fog, in particular over sea (de Rooy 2014). Introduction of HARATU was motivated by results of the Atlantic Stratocumulus to Cumulus Transition Experiment, which revealed that the old turbulence scheme CBR (Cuxart et. al. 2001), named after the creators, substantially underestimated cloud-top entrainment for that case, which is therefore increased in HARATU.
Compared to CBR, there are in HARATU considerable changes in the length-scale formulation and the constants used (Bengtsson et. al., 2017). The CBR scheme uses one master length scale, which is multiplied by a number of stability dependent functions. In HARATU these stability corrections are part of the length-scale formulation.

Based on an analysis by de Rooy and de Vries (2017), the implementation of HARATU has considerably reduced the cloud cover, and resulted in an increase in the cloud base heights compared to the CBR scheme. Furthermore the wind climatology of the model is considerably improved, with also improvements of the standard and absolute errors of the wind forecasts.

2.4.2 OCND2 update to cloud microphysics

It has been observed that the original microphysics scheme generates cloud ice too quickly when temperatures inside the clouds are between -5° and -10°C, where in reality some supercooled liquid would be expected (Bengtsson et. al., 2017). Also, the original scheme removed most supersaturation with respect to ice for

temperatures below -20°C, where in reality supersaturation in such conditions is common.
To address these weaknesses in the representation of clouds in cold conditions, an update named 'OCND2' has been introduced (Müller et. al. 2017). The main difference compared to the original scheme is that the fraction of the grid box with cloud ice is no longer handled by the large-scale condensation and thermodynamic adjustment scheme, but instead is parameterized using a cloud scheme based on the critical relative humidity with respect to ice. In the original scheme, both cloud water and ice where diagnosed as they were functions of temperature only. Under OCND2, cloud ice is treated by the rest of the ICE3 microphysics.
Other updates include a reduction of the deposition rate of ice-phase water species, a reduction of ice nucleolus concentration in temperatures between 0° and -25°C, and use of the Kogan parameterization for the process of rain drop activation from cloud droplets.

Mainly in wintertime under cold conditions, the OCND2 update improves the representation of mixed-phase and pure ice clouds, by increasing (decreasing) the amount of liquid (ice) water in low-level clouds. As a result a cold bias in 2-m temperature is reduced, as is an existing dry bias in relative humidity throughout the lower atmosphere in winter.

2.5 Model configurations for comparing observed and simulated convection

Four model configurations have been selected for the comparison between observed and simulated convection. In addition to the current (reference) HARMONIE configuration (REF), three additional configurations are included, with certain important parameterizations disabled, or with certain recent updates being made undone. In the first of these the turbulence scheme HARATU is replaced by the previously used CBR scheme (NOHAR), undoing the replacement of the turbulence scheme. In the second the OCND2 update to the cloud microphysics has been made undone, such that the old microphysics scheme is used (NOOC). In the third, the shallow convection scheme has been disabled (NOSHAL).
By including these three additional configurations in the comparison, we can analyse the effect that these updates/schemes have on simulated convection. Table 2.2 provides a summary of these four model configurations. In addition to these four basic configurations, sometimes a configuration is used in which multiple updates are undone and/or schemes are disabled. These configurations have names such as NOHAR_NOSHAL, for a configuration in which both HARATU is replaced and the shallow convection scheme is disabled.

Table 2.2: Model configurations used in the comparison between observed and simulated convection.

Name	**Description**
REF	Current (reference) HARMONIE configuration
NOHAR	As REF, but without the replacement of the old turbulence scheme CBR by HARATU
NOOC	As REF, but without the OCND2 update to the microphysics scheme
NOSHAL	As REF, but with the shallow convection scheme disabled

Chapter 3

Comparing simulated with observed convection

Simulated convection can be compared with observed convection by considering measures like precipitation intensity or hydrometeor content. For considering three-dimensional storm structures, measures of hydrometeor content seem more useful. Observationally, a measure of hydrometeor content is provided by precipitation radars in the form of the equivalent reflectivity factor. This quantity can also be simulated from model output of hydrometeor contents, making it suitable for comparison.

In what follows, first an introduction to measuring radar reflectivity by precipition radars is given in section 3.1. Section 3.2 then describes how the equivalent reflectivity factor can be calculated from measured radar reflectivity. For brevity and because of common usage, in what follows the equivalent reflectivity factor is usually referred to as reflectivity, except when confusion with actual radar reflectivity is possible.
Next, section 3.3 describes how reflectivity can be calculated from model output of hydrometeor contents. In order to have radar observations available on the whole HARMONIE grid, it is necessary to combine observations from multiple radars into a composite. This process is described in section 3.4. There are however a number of factors that could lead to errors in measurements of reflectivity, which thus complicate the comparison between observed and simulated reflectivity fields, and these are addressed in section 3.5.

3.1 Measuring precipitation by precipitation radars

A precipitation radar transmits pulses of electromagnetic signals, and subsequently waits to receive signals that are scattered backward by objects encountered by the pulse. These pulses are transmitted at a certain pulse repetition frequency (PRF), that determines the distance that a certain pulse can travel before the next is transmitted as (Yuter 2002)

$$r_{max} = \frac{c}{2PRF}. \tag{3.1}$$

The receiver of the radar detects and amplifies the received signals, and averages the characteristics of the returned pulses over defined time periods. Antennas are used to focus the transmitted energy and direct it along a narrow angular beam, of which the size and shape is determined by the antenna shape. Most precipitation radars use a circular parabolic antenna. The energy in the radar beam is maximum along the center, and decreases outward with increasing distance to the center. The width of this beam is defined as the angular diameter where the power is exactly half the maximum power.

Radar wavelengths vary between precipitation radars, and an overview of common wavelength bands is provided in table 3.1. Radars with smaller wavelengths have as disadvantage that they are much more prone to beam attenuation by air molecules and precipitation than radars with larger wavelengths, as described in more detail in section 3.5.1. However, radars with larger wavelengths require a larger and more expensive antenna to focus the beam, making it more expensive to operate such radars.

Table 3.1: Precipitation radar frequencies, wavelengths and applications per frequency band (from Yuter, 2002).

Band designation	Nominal frequency	Nominal wavelength	Applications
S	2-4 GHz	15-8 cm	Surface-based radars
C	4-8 GHz	8-4 cm	Mobile and surface-based radars
X	8-12 GHz	4-2.5 cm	Mobile and surface-based radars
K_u	12-18 GHz	2.5-1.7 cm	Mobile and spaceborne radars
K_a	27-40 GHz	1.1-0.75 cm	Mobile and spaceborne radars

The relationship between transmitted and backscattered received power from precipitation targets is expressed by the 'radar equation', in terms of the radar's hardware characteristics and the distance between transmitter and target.
For an isotropic transmitter and isotropic target, the power incident at at a target at distance r_1 is given by

$$P_i = \frac{P_t A_t}{4\pi r_1^2}, \tag{3.2}$$

where A_t is the cross-sectional area of the target, and P_t is the transmitted power. Under the assumption that the target does not absorb any power and radiates the energy it receives isotropically, the power scattered towards a receiver of effective cross-sectional area A_e, at distance r_2 from the target, is given by

$$P_r = \frac{P_t A_t A_e}{(4\pi)^2 r_1 r_2}. \tag{3.3}$$

For precipitation radars, the transmitted energy is focused with an antenna. The antenna gain is defined as the ratio of the power per unit area along the axis of the focused beam and the power per unit area of an isotropic transmitter. For a circular parabolic antenna, it can be approximated in general as a function of the horizontal (θ_H) and vertical (θ_V) beam widths in radians, or for the receiving antenna as a function of the radar wavelength λ and A_e, as

$$G \approx \frac{\pi^2}{\theta_H \theta_V} \approx \frac{4\pi A_e}{\lambda^2}. \tag{3.4}$$

The gain for the transmitting antenna requires replacing P_t by GP_t in (3.3), and given that usually precipitation radars use a single antenna for both transmitting and receiving, we can also replace A_e by $G\lambda^2/(4\pi)$. Further, $r_1 = r_2$ for backscattering towards the transmitting radar, such that (3.3) can be rewritten as

$$P_r = \frac{P_t G^2 \lambda^2 \sigma}{(4\pi)^3 r^4}. \tag{3.5}$$

Here, σ is the backscattering cross section, which is defined as the apparent area, that if scattered isotropically, would return to the receiver an amount of power equal to the power actually received.

Precipitation particles usually fill the volume illuminated by the radar, requiring another expression for the power received by the radar by backscattering from one 'resolution volume'. This resolution volume is defined as the incremental volume along the beam from which scattered energy is received simultaneously at the radar. This approximately cylindrical resolution volume has dimensions

$$V_{res} = \pi \left(r\frac{\theta_H}{2} \right) \left(r\frac{\theta_V}{2} \right) \frac{c\tau}{2}. \tag{3.6}$$

Here, τ is the pulse duration in seconds, and $c\tau/2$ is the height of the cylinder (the factor $1/2$ comes in because the backscattered energy from the front edge of the pulse at time $t_0 + \tau/2$ and range $r_0 + c\tau/2$ arrives at the same instant as backscattered energy from the trailing edge of the pulse at time $t_0 + \tau$ and range r_0). A visual representation of a resolution volume is provided in figure 3.1.

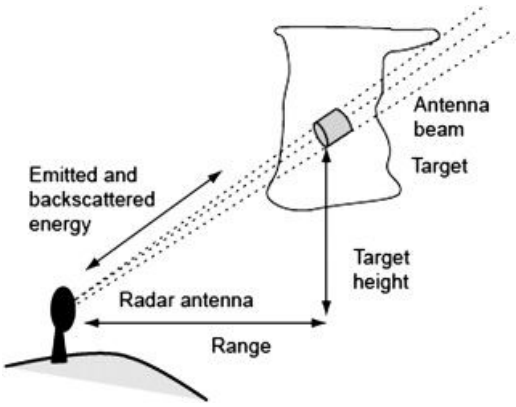

Figure 3.1: Drawing illustrating the process of scanning the atmosphere with a precipitation radar. From Shelton (2009).

To account for the actual distribution of power within a beam generated by a circular parabolic antenna, a correction factor of $1/(2\ln 2)$ is applied to (3.6). Multiplying (3.5) by this resolution volume and replacing σ by the sum of the backscattering cross sections of all particles within the volume, results in a version of the radar equation that is applicable to distributed scatterers, and that is used in signal processors of precipitation radars;

$$\bar{P}_r = \frac{P_t G^2 \lambda^2 \theta_H \theta_V c\tau}{1024(\ln 2)\pi^2 r^2} \sum_{V_{unit}} \sigma_i. \tag{3.7}$$

The overbar indicates that the received power is averaged over multiple consecutive pulses, usually 50 or more. The sum over all backscattering cross sections in a unit volume V_{unit} is called the radar reflectivity, and is thus mathematically given by

$$\eta = \sum_{V_{unit}} \sigma_i, \tag{3.8}$$

To be of value in precipitation studies, $\bar{P}_r$ must be related to the physical characteristics of the precipitation particles. As described in the following section, a useful quantity called 'equivalent reflectivity factor' provides more information about these physical characteristics, and can be related to the radar reflectivity η.

3.2 Equivalent reflectivity factor

Small spherical hydrometeors that satisfy the criterion

$$D_i \lesssim \frac{\lambda}{16} \tag{3.9}$$

fall within the Rayleigh scattering regime (Yuter 2002), for which σ_i can be related to the hydrometeor diameter D_i and λ as

$$\sigma_i = \frac{\pi^5 |K|^2 D_i^6}{\lambda^4}. \tag{3.10}$$

Here, $|K|^2$ is a dielectric constant, that is different for water and ice. Larger particles fall within the Mie scattering regime, for which the backscattered returned power fluctuates as a function of the wavelength, as shown in figure 3.2.

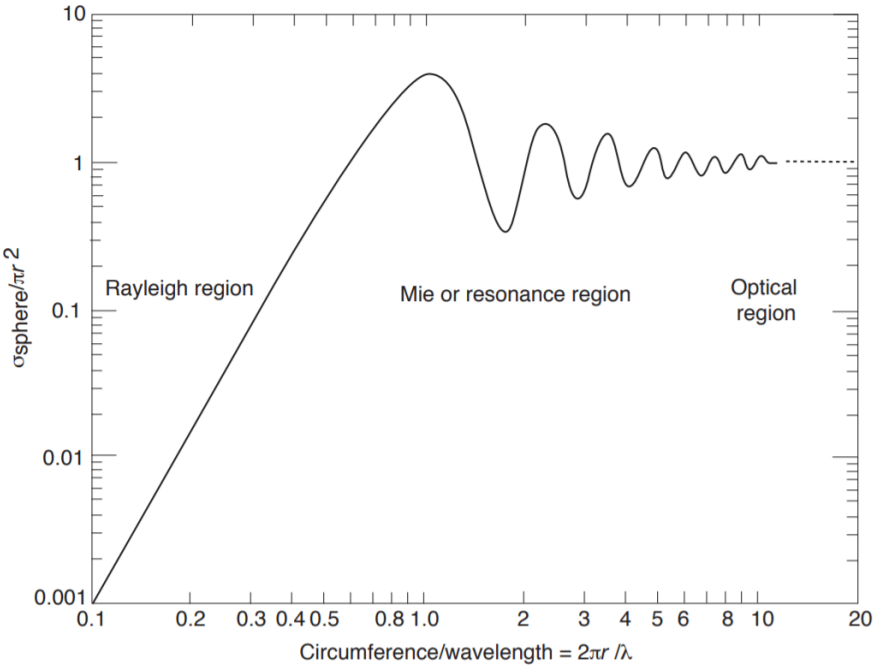

Figure 3.2: Normalized backscattering cross section area of a perfectly conducting sphere as a function of circumference divided by radar wavelength. Since water drops are not perfectly conducting, the transition from Rayleigh to Mie scattering for the radar reflectivity of spherical water drops occurs at $2\pi r/\lambda \sim 0.2$. From Yuter (2002).

For nonspherical hydrometeors, Marshall and Gunn (1952) showed that in the Rayleigh scattering regime for a weak dieletric like ice, the radar cross section of an irregularly shaped particle is the same as that of a sphere with the same mass. For irregularly shaped ice particles D_i represents the diameter of that sphere, i.e. the equivalent diameter. Substituting (3.10) into (3.8) gives

$$\eta = \frac{\pi^5 |K|^2}{\lambda^4} \sum_i n_i D_i^6. \tag{3.11}$$

From (3.11) it follows that one can define a radar reflectivity factor Z, that is proportional to the radar reflectivity but independent of the radar wavelength, as

$$Z = \sum_i n_i D_i^6 \rightarrow \int_0^\infty n(D) D^6 dD, \tag{3.12}$$

where the integral version is applicable when a continuous number density distribution is available. Under the Rayleigh approximation Z can be calculated as

$$Z \overset{\text{Rayleigh}}{=} \frac{\eta \lambda^4}{|K|^2 \pi^5}. \tag{3.13}$$

A difficulty with calculating Z as in (3.13) is however that the dielectric constant $|K|^2$ is dependent on the phase of the hydrometeors, which is generally unknown (Smith 1984). For this reason an equivalent reflectivity factor Z_e has been introduced, which uses the value $|K|^2 = |K_w|^2 = 0.93$ as valid for water, and is thus given by

$$Z_e = \frac{\eta \lambda^4}{|K_w|^2 \pi^5}. \tag{3.14}$$

Under the Rayleigh approximation, Z_e equals Z for rain drops. For ice particles, where $|K|^2 = |K_i|^2 = 0.176$ in (3.13), Z_e and Z are related as

$$Z_e \overset{\text{Rayleigh}}{=} \frac{|K_i|^2}{|K_w|^2} Z. \tag{3.15}$$

The equivalent reflectivity factor Z_e can be described as the radar reflectivity factor of a target consisting of water drops with diameters that are small compared with the radar wavelength, which would produce the same

reflectivity as that of a target with unknown properties (AMS glossary 2019).
Because Z_e can take on values that differ many orders of magnitude, it is commonly expressed on a logarithmic scale relative to a radar reflectivity factor $Z_0 = 1$ mm^6 m^{-3}, in decibels (dB) relative to Z (dBZ) as

$$dBZ = 10 \log_{10} \left(\frac{Z_e}{Z_0} \right). \tag{3.16}$$

This quantity is usually shown on radar displays, and as noted in the introduction of chapter 3, it will in what follows mainly be referred to simply as reflectivity, except when more precise terminology is preferrable. It is this quantity that will be used to compare modelled convection with observed convection, and we thus need to estimate it from model output, which is the topic of the next section.

3.3 Estimating reflectivity from model output

Calculating Z_e as in (3.14) requires knowledge about η, and thus about the backscattering cross sections of the hydrometeors. As described in section 3.2, we can apply the Rayleigh approximation for particles that satisfy condition (3.9), in which case we can simply calculate Z_e from Z, given by (3.12). We first need to know however to what extent the Rayleigh approximation is applicable.

Caumont et al. (2006) used four different methods to calculate simulated reflectivity fields in the Meso-NH model, that uses the same hydrometeor size distributions as HARMONIE. These methods use Rayleigh scattering (spheres), Mie scattering (spheres), Rayleigh-Gans scattering for spheroids, and T-matrix scattering for spheroids. Figure 3.3 shows for rain drops the difference in reflectivity relative to that produced by the Rayleigh method for the three other methods, for rain contents up to $6 \cdot 10^{-3}$ kg/m^3, and radar wavelengths of 5 and 10 cm. The maximum difference is reached for $M_r = 6 \cdot 10^{-3}$ kg/m^3, and is about 2.5 dB for $\lambda = 5$ cm, and about 1.5 dB for $\lambda = 10$ cm. For ice particles, table 4 in Caumont et al. (2006) shows a maximum difference of 0.1 dB between reflectivities produced by the Rayleigh and Mie scattering methods for a certain period with intense precipitation, showing that for ice particles the discrepancies are even smaller than the already limited differences for rain content (when expressed in dB).
Based on these results it seems unnecessary to apply a more complex theory for scattering than that of Rayleigh for calculating simulated reflectivity fields. The remainder of this section develops an expression for the equivalent reflectivity factor Z_e that can be calculated from HARMONIE output, based on the Rayleigh approximation.

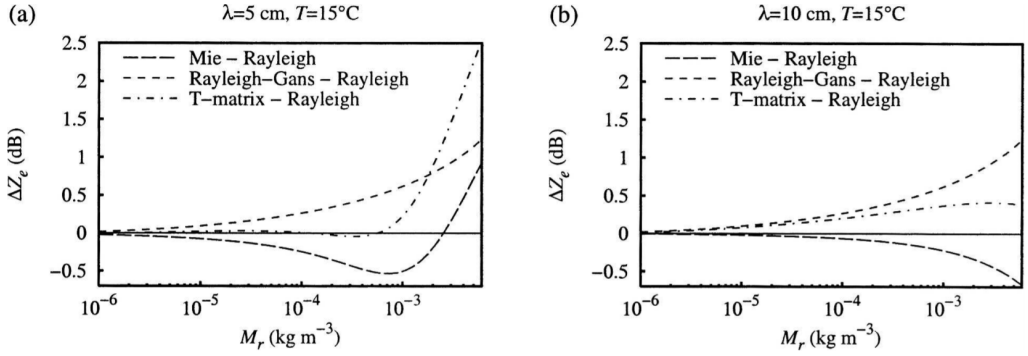

Figure 3.3: Departures from Rayleigh scattering by raindrops in terms of equivalent reflectivity factors (reflectivities) as functions of rainwater contents (M_r) for (a) $\lambda = 5$ cm and (b) $\lambda = 10$ cm at 15°C. The Rayleigh and Mie solutions are applicable to spheres, whereas the RayleighGans and T-matrix solutions are computed for spheroids. From Caumont et al. (2006).

A first step in calculating Z_e from model output is to calculate Z as in (3.12) using the integral version, as continuous number density distributions are available.
For this we need to use equivalent diameters, i.e. the diameter of a sphere with the same mass as the actual particle. Using (2.4), it can easily be shown that the equivalent diameter is given by

$$D_{eq} = \left(\frac{6a}{\pi \rho_x} \right)^{\frac{1}{3}} D^{\frac{b}{3}}, \tag{3.17}$$

where ρ_x is the density of the hydrometeor. Substituting (3.17) into (3.12) gives

$$Z = \left(\frac{6a}{\pi \rho_x} \right)^2 \int_0^\infty n(D) D^{2b} dD = \left(\frac{6a}{\pi \rho_x} \right)^2 N M(2b) = \left(\frac{6a}{\pi \rho_x} \right)^2 N \frac{G(2b)}{\lambda^{2b}}, \tag{3.18}$$

where (2.2) and (2.3) have been used for the last two equations. Recall that λ is related to the hydrometeor mixing ratios, and given by (2.9) as

$$\lambda = \left(\frac{\rho r}{G(b) a N} \right)^{-\frac{1}{b}}. \tag{3.19}$$

For the precipitating particles, for which $N = C\lambda^x$ as in (2.7), one can finally arrive at

$$Z = \left(\frac{6a}{\pi \rho_x} \right)^2 C G(2b) \lambda^{x-2b}. \tag{3.20}$$

For ice particles, calculating Z_e requires multiplying Z by the ratio of dielectric constants, $|K_i|^2/|K_w|^2 = 0.189$. If one prefers to replace ρ_x in (3.17) by ρ_l, the density of liquid, then the ratio of densities $(\rho_l/\rho_w)^{1/3}$ should be included in the multiplication factor, giving a value of 0.224 (Smith 1984).

3.3.1 Comparison to implementation in HARMONIE

Simulated reflectivity is also calculated in the post-processing system of HARMONIE (script src/arpifs/adiab/gpprs0d.F90). In this system the contributions from rain, snow and graupel are calculated as described above. Differences are given by the inclusion/exclusion of the contribution from cloud ice, and the inclusion/exclusion of the effect of melt on the reflectivity of graupel. Both effects are included in the post-processing system, while excluded here. This has been done for the following reasons:

1. The contribution from cloud ice and cloud water hydrometeors is very marginal, because of their small diameters and the fact that the integrand of (3.12) is proportional to D^6.

2. As explained in section 3.5.3, cross sections through reflectivity in stratiform precipitation will show a bright band when precipitation falls through the freezing level, in the melting layer. It has been decided to exclude this melting layer from the comparison, given that its altitude may vary between model and reality, leading to discrepancies in reflectivity in CAPPI composites due to discrepancies in the altitude of the freezing level. These latter discrepancies are not focused on here, and thus there is no need to correctly simulate the melting layer.
   Also, the bright band will appear broader in radar observations than in the model (especially in regions far away from any radar), due to the increase in radar beam width with increasing distance. Thus even if observed and simulated freezing level would be equal, and if the model correctly simulates the bright band, it would still appear differently in radar observations due to their limited vertical resolution.

3.3.2 Interpolating simulated reflectivity onto a constant-altitude grid

As described in section 2.2, the current HARMONIE setup uses 65 hybrid vertical levels, for which the simulated reflectivity can be computed. In order to facilitate comparison with radar observations, these values are interpolated onto a constant-altitude grid. Simple linear vertical interpolation between the (centers of) the hybrid levels is used to estimate values at the selected constant altitude, in a manner similar to that described in section 3.4.2.4.
An example of simulated reflectivity at different altitudes is shown in figure 3.4.

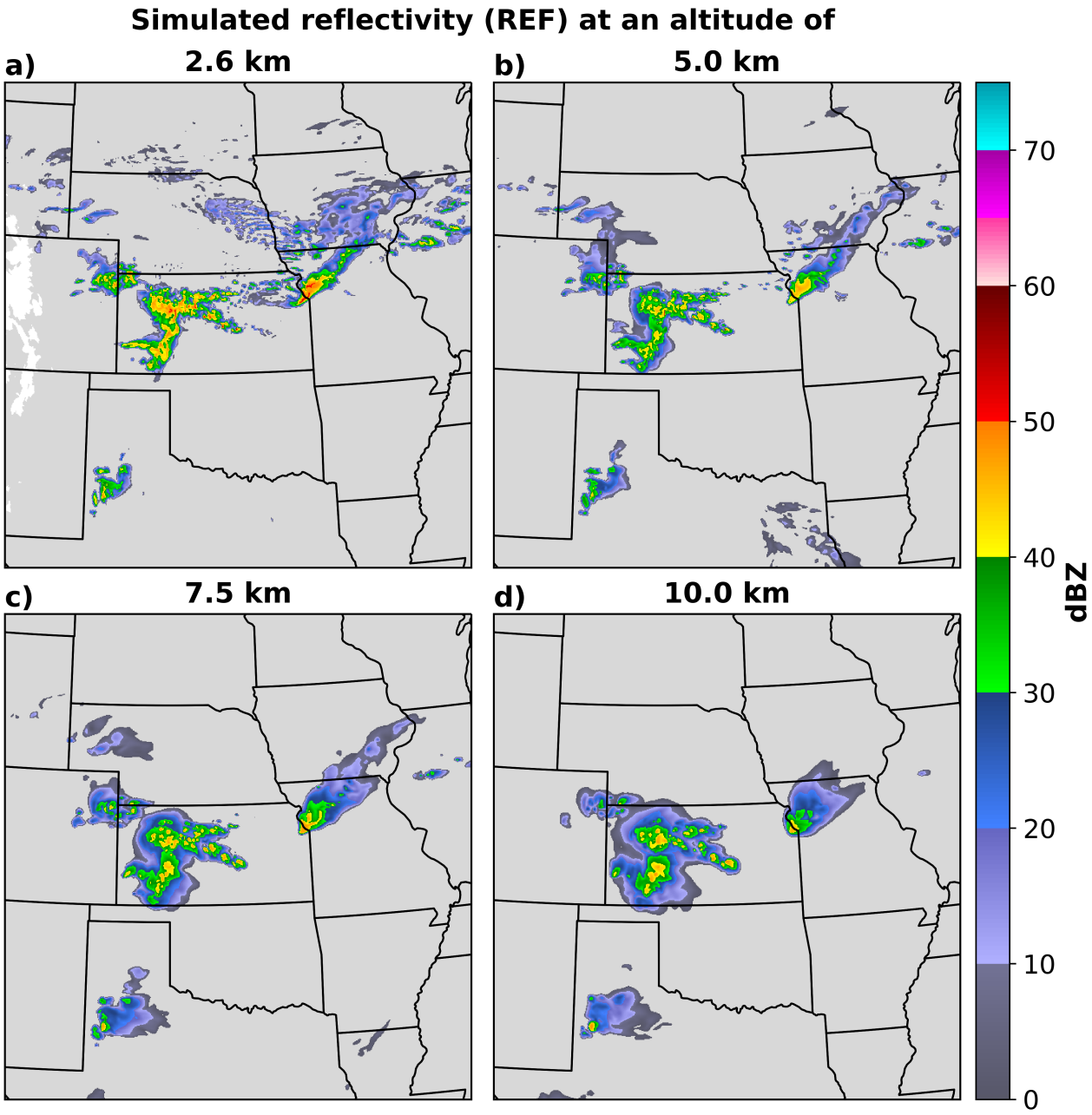

Figure 3.4: Simulated reflectivity at May 7, 2019, 4 UTC, over the Central US, for altitudes of a) 2.6, b) 5.0, c) 7.5 and d) 10.0 km. White colors indicate that the terrain reaches above the given altitude. Light grey indicates reflectivity values below 0 dBZ. The data originates from the +10h forecast of a run with the REF configuration for May 6, 18 UTC.

3.4 Obtaining constant-altitude radar composites

Precipitation radars typically use a scan strategy in which the scanning pattern is repeated after a certain time, usually about five minutes. One such a repetition of the scanning pattern provides a radar volume, that consists of multiple individual scans obtained under different elevation angles (the angle that the radar antenna makes with a geopotential surface). As an example, the scans in a typical US NEXRAD volume are indicated in figure 3.5.

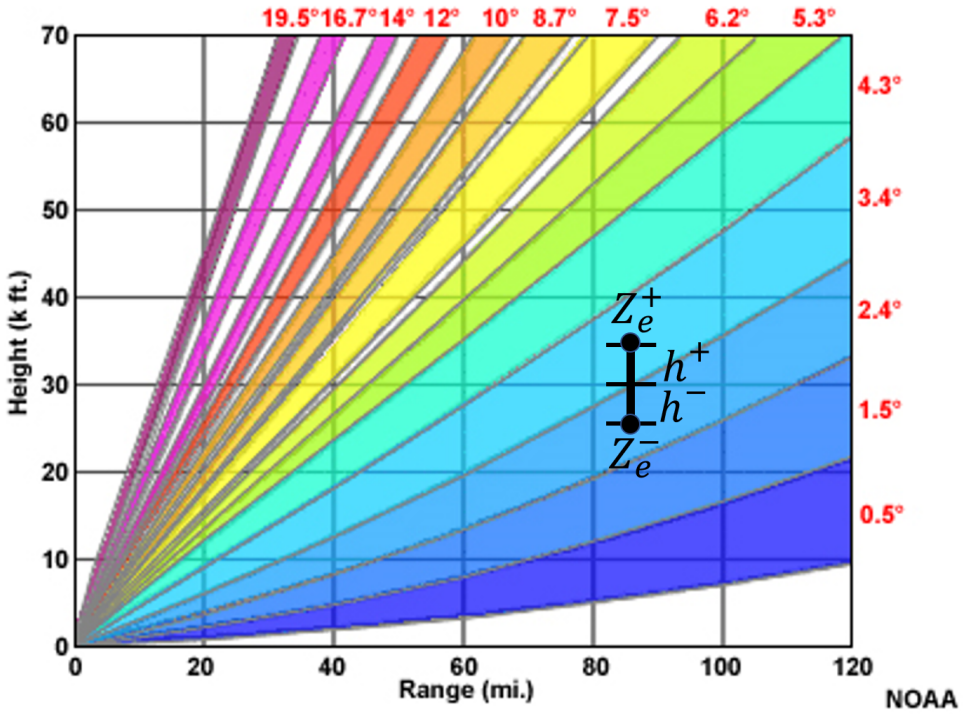

Figure 3.5: Schematic diagram showing the area scanned by a NEXRAD precipitation radar for different elevation angles, in range-height plane. These radars provide an angular beam width of about 1°. Also indicated is the interpolation procedure to obtain a CAPPI at an altitude of 30 kft (section 3.4.2.4).

It varies per country and operating institute whether these radar volumes are available publicly, and if so, whether this also holds for archived data. Institutes that publicly provide both recent and archived radar volumes are e.g. the KNMI and the NOAA (US NEXRAD data). Additionally, it varies per institute whether these radar volumes are quality-controlled (i.e. corrected for presence of ground clutter and possibly other nonprecipitation echoes), or not. As discussed in section 4.1.2, quality control is necessary for US NEXRAD volumes provided by the NOAA.

In order to get reflectivity available for the whole HARMONIE grid at different altitudes, it is necessary to combine reflectivities from multiple radars. This requires mapping of reflectivities from individual radars (provided in spherical coordinates) onto the cartesian HARMONIE model grid, where the reflectivity at a grid cell in the composite is usually taken to be a weighted average of reflectivities from surrounding radars. Except for the choice of the weighting function, also important is the interpolation method used in the horizontal and vertical. This interpolation is desired, as for a composite for a given altitude, not every composite grid cell is covered by a resolution volume from an individual radar. In contrast, other grid cells are covered by multiple resolution volumes from a single radar, also requiring consideration.
Further, different radar scans are performed at different times, and radar volumes from different radars might start and end at different times, as is the case for the US NEXRADs. Due to this latter point, one has to decide between either combining radar scans from different radar volumes within a specified time interval, or using complete radar volumes that start and end at different times.

3.4.1 Existing approaches

A few existing approaches for creating these radar composites are documented in literature. Langston et al. (2007) designed a method to create four-dimensional radar mosaics. Depending on the user's choice, it uses one of three methods to interpolate the radar data from the spherical radar grid onto the cartesian composite grid. These methods are nearest-neighbour (NN) mapping in both the horizontal and vertical, linear interpolation in the vertical (VI) plus NN, and VI plus two-dimensional horizontal linear interpolation (VHI). Zhang et al. (2005) concluded that VI is suitable for most cases, except for the occurrence of a bright band (section 3.5.3), where VHI produces better results.
Associated with the mapping are 'remapping weights', which are determined for each grid cell in the spherical radar grid, and provide for each composite grid cell that is 'influenced' by it a weight associated with their reflectivity value. The total weight for the contribution of a spherical radar grid cell to a composite grid cell influenced by it, follows by multiplying the remapping weight w_{remap} by a distance-dependent weight w_{dist},

and a time-dependent weight w_t, giving

$$w = w_{remap} \cdot w_{dist} \cdot w_t. \tag{3.21}$$

The last two weights are given by $w_{dist} = \exp(-r^2/R^2)$ and $w_t = \exp(-t^2/T^2)$, with R and T adaptable length and time scales, that determine how fast the weights decrease with increasing distance to the radar for w_{dist}, and time difference with respect to the analysis time for w_t.
Reflectivity scans up to 10 minutes old are stored and allowed to contribute to the composite.

Homeyer et al. (2017) designed another method, used to create the three-dimensional Gridded NEXRAD WSR-88D Radar dataset (GridRad). This method shares many of the characteristics of the method of Langston et al. (2007). The weights are expressed as in (3.21), with the same expressions for w_{dist} and w_t as used by Langston et al., using $R = 150$ km and $T = 150$ s.
Differences appear in the remapping of the spherical radar data onto the cartesian composite grid. In the horizontal, spherical radar grid cells contribute only to the nearest GridRad column. Further, a different method is used to deal with the vertical spacing between reflectivity scans of a single radar. They do not apply vertical interpolation during the remapping of the spherical radar data onto the composite grid. Further, they do not allow a single radar scan to contribute to a depth larger than 1.5 km, to limit the altitude error that could be made when including spherical radar grid cells that span a large vertical depth, which for a radar with an angular beam width of 1 degree would be more than 3 km for distances greater than 180 km.
Finally, only radar scans for which the central time differs by less than 3.8 minutes from the analysis time are allowed to contribute to the composite.

3.4.2 A different compositing method

The two methods described in the preceding section have as disadvantage that although they incorporate the time difference between the analysis time and the central time of the radar scan into the weights, they still combine data obtained at times that potentially differ by more than 5 minutes, smoothing the data. Given that the focus of this research is on precipitation *patterns* instead of *exact locations*, it has been decided that further limitation of data smoothing is desired, even if that leads to a larger positional error with respect to the analysis time.
For this reason, a clearly different method is developed to create the constant-altitude radar composites, which is described in the remainder of this section.

3.4.2.1 Overview of the method

For a given analysis time and altitude for a composite, and at a specific location within the composite, the nearest reflectivity measurements from different radars for that location could potentially differ in time by about 5 minutes, for a typical radar scanning strategy. Averaging these measurements, even when using weights that decrease with increasing time difference, could lead to considerable smoothing of the reflectivity field in the resulting composite, which is undesired as described above. For this reason, it has been decided to let the reflectivities in the composite be mainly determined by the nearest radar, by choosing a data weighting function that decreases very rapidly with increasing distance.

Further, for most precipitation radars the antenna elevation angle either increases or decreases monotonically in time during a single radar volume, except perhaps for a few elevation angles that are scanned more than once during a volume. An example of a 'Volume Coverage Pattern' for US NEXRADs, with repetitions of the lowest scan, is shown in figure 3.6. Scans that are repeated during the volume can be excluded from contribution to the composite (except for the first occurrence), such that for the remaining scans the elevation angle changes monotonically in time. A consequence of this is that within a single radar volume, consecutive radar scans in the vertical differ in time by usually not more than 30 seconds, limiting data smoothing when applying vertical interpolation between radar scans. Thus by letting only one single complete radar volume per radar contribute to the composite, instead of all scans within a certain time window from potentially multiple volumes as is done in the methods described in section 3.4.1, data smoothing is further reduced.

The combined effect of these decisions leads to a method that produces a composite, in which data smoothing due to averaging data from multiple radars/elevations that are obtained at different times, is very limited. As described before, the main disadvantage is however that the positional error (i.e. the difference between true position at analysis time, and position within the composite) is larger compared to what is the case for the methods described in section 3.4.1. Details of the method are described below.

Elevation Angles (VCP 12)	VCP 12 Elevation Duration	SAILS	SAILSx2	SAILSx3
0.5°	31 Sec	31 Sec	31 Sec	31 Sec
0.9°	31 Sec	31 Sec	31 Sec	31 Sec
1.3°	31 Sec	31 Sec	31 Sec	31 Sec
0.5°				31 Sec
1.8°	15 Sec	15 Sec	15 Sec	15 Sec
0.5°			31 Sec	
2.4°	14 Sec	14 Sec	14 Sec	14 Sec
3.1°	14 Sec	14 Sec	14 Sec	14 Sec
0.5°		31 Sec		
4.0°	14 Sec	14 Sec	14 Sec	14 Sec
0.5°				31 Sec
5.1°	14 Sec	14 Sec	14 Sec	14 Sec
6.4°	14 Sec	14 Sec	14 Sec	14 Sec
0.5°			31 Sec	
8.0°	13 Sec	13 Sec	13 Sec	13 Sec
0.5°				31 Sec
10.0°	13 Sec	13 Sec	13 Sec	13 Sec
12.5°	13 Sec	13 Sec	13 Sec	13 Sec
15.6°	13 Sec	13 Sec	13 Sec	13 Sec
19.5°	13 Sec	13 Sec	13 Sec	13 Sec
Duration	243 Sec	274 Sec	305 Sec	336 Sec

Figure 3.6: Overview of elevation angles, scanning order and scan durations for Volume Coverage Pattern 12 of the US NEXRADs, for different numbers of scans of the lowest elevation. Adapted from https://radarlab.wordpress.com/2015/04/.

3.4.2.2 Selection of radar volumes that contribute to the composite

For a given analysis time t_c for the composite and a given radar, the method selects the volume for which the central time t_v (average between start and end time of volume) is closest to t_c. In order to prevent issues in case of problems with data delivery, with gaps in the provided data, the time difference between t_c and t_v is not allowed to be more than 4 minutes.
If there are two radar volumes for which $|t_c - t_v|$ is equal, then the first volume is always chosen. This is for instance relevant when the volumes are provided with a regular 5-minute interval, as is the case for e.g. the KNMI.

3.4.2.3 Relating range to radar beam altitude

Projecting the data of individual radar scans onto a constant-altitude grid requires first a means to estimate the beam altitude above radar level. Apart from the elevation angle, also the curvature of earth's surface and refraction within the atmosphere influence the beam altitude. A common model for the path of a radar beam is given by the Effective Earth's Radius Model (Doviak and Zrnić 1993). In this model, earth's radius is multiplied by a certain constant to account for the effects of refraction on the beam path, giving an effective earth radius. A common value used for this multiplication constant is 4/3, assuming normal refraction. Using this model, an expression for the radar beam altitude is given by

$$h = \sqrt{r^2 + (k_e a)^2 + 2 r k_e a \sin\theta_e} - k_e a, \tag{3.22}$$

where r is the range (distance to the radar), and θ_e is the elevation angle of the radar antenna.
Equation (3.22) provides the altitude above radar level. With knowledge of the radar elevation above (mean) sea level (ASL), these values can be converted to altitude ASL, simply referred to as altitude in what follows.

3.4.2.4 Generating a constant-altitude plan position indicator for a single radar

The next step is to generate constant-altitude plan position indicators (CAPPIs) for every individual radar that contributes to the composite, which provide (interpolated) reflectivity at a fixed altitude. To generate them, first for each elevation angle reflectivity is interpolated onto the CAPPI grid, that in this step is still taken to

be a horizontal polar grid. Next, reflectivity at each CAPPI grid cell is taken to be the weighted mean of the nearest reflectivities above and below the CAPPI altitude, as

$$Z_e(i,j) = \frac{h^- Z_e^+(i,j) + h^+ Z_e^-(i,j)}{h^- + h^+}. \tag{3.23}$$

Here, $Z_e(i,j)$ denotes CAPPI reflectivity at grid cell (i,j), expressed in dBZ. $Z_e^{+(-)}$ denotes the nearest reflectivity above (below) the CAPPI altitude, and $h^{+(-)}$ the altitude difference between $Z_e(i,j)$ and $Z_e^{+(-)}$. A visualization is provided in figure 3.5.

3.4.2.5 Generating a constant-altitude composite

CAPPIs from individual radars are projected onto the HARMONIE model grid, which has a lambert conformal conic projection, in order to have reflectivity available for the whole grid. For this constant-altitude composite, the reflectivity at grid cell (i,j) is given by

$$\zeta(i,j) = \frac{\sum_{k=1}^{N} w_k(r_k)\zeta_k(i,j)}{\sum_{k=1}^{N} w_k(r_k)}. \tag{3.24}$$

Here N is the number of radars contributing to the composite, $\zeta_k(i,j)$ is the CAPPI reflectivity from radar k closest to grid cell (i,j), and w_k is a weight given to $\zeta_k(i,j)$, that is dependent on its distance to the radar, r_k. As argued in section 3.4.2.1, the weights w_k should decrease very rapidly with increasing range. It has been decided to express the w_k as

$$w_k(r_k) = r_k^{-10}, \tag{3.25}$$

such that essentially, the reflectivity at a certain composite grid cell is determined almost purely by reflectivities from the nearest radar.

As an example, a map of maximum relative weight given to contributions from a single radar is provided in figure 3.7, for different altitudes, and for a grid covering the Central US, using US NEXRAD data. For this map we indeed see that for most of the grid this maximum relative weight is close to 1, indicating that the composite reflectivity is determined almost purely by a single radar. Note however that the values are dependent on the scanning strategies used for the radars, as explained in the caption of the figure.

A map of composite reflectivity for the same time and altitudes is provided in figure 3.8. One artefact of the compositing method is the appearance of ring-shaped patterns in reflectivity around the upper boundary of precipitation cores, as is the case especially for 10.0 km altitude in figure 3.8. The appearance of these patterns is a disadvantage of interpolating only in the vertical, and of using mainly data from a single radar, which leads to an alternating pattern of over- and underestimation of the altitudes of dBZ surfaces. They could also appear around the lower boundary of precipitation cores, but a better vertical resolution of the data here limits this.
The goal of this research is to compare simulated convection with observed convection, and as will be explained in chapter 6, this involves the calculation of dBZ distributions for certain altitudes. If reflectivity would be constant over the whole domain, these dBZ distributions would be substantially affected, because the artefact would cause reflectivity to take on values within a larger interval surrounding the true value. The variation of reflectivity within the domain should partly average out this effect however, thus limiting it. For this reason this artefact is not expected to greatly influence the results, though its effect has not been quantified in any manner.

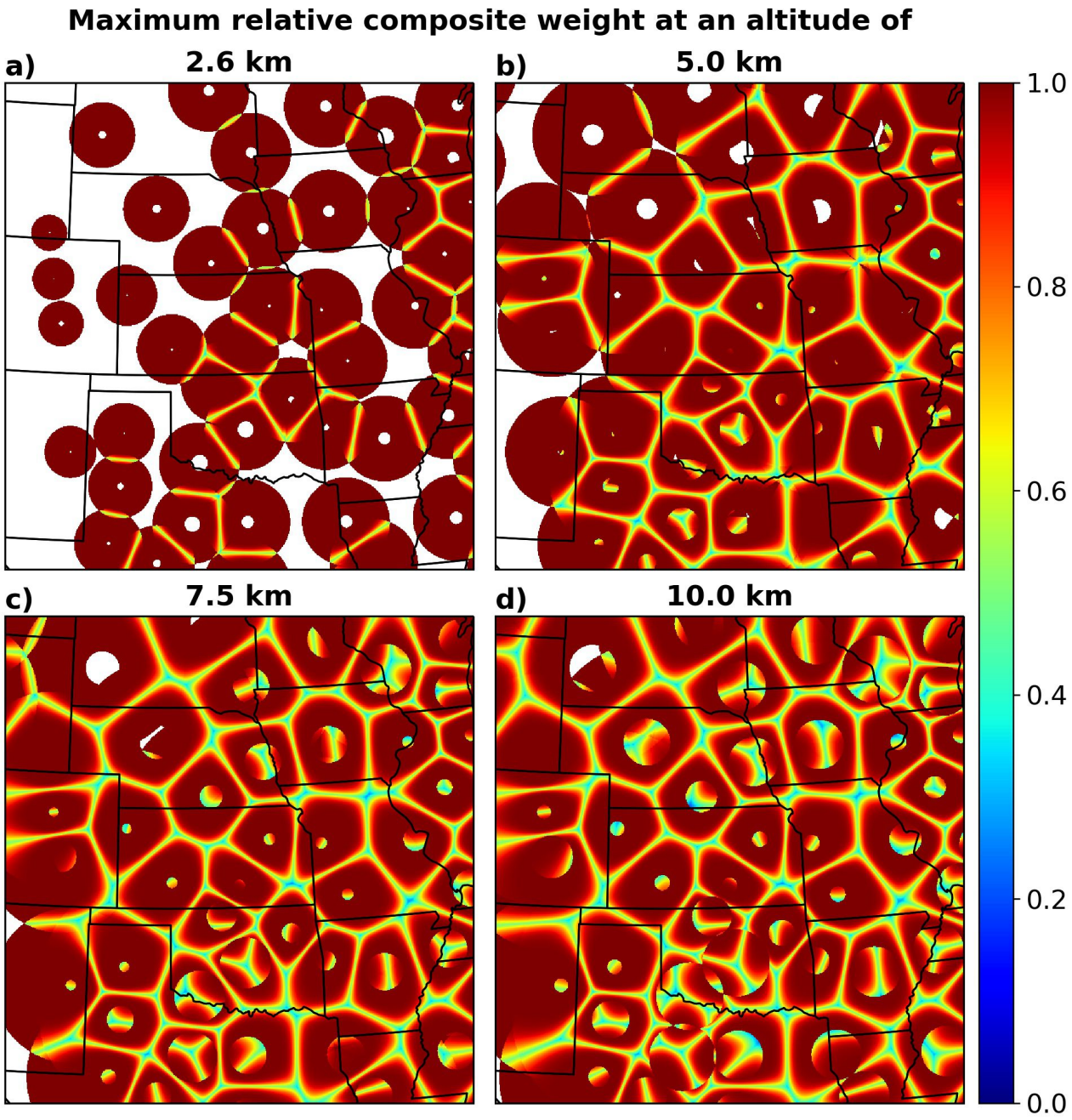

Figure 3.7: Maximum relative weight given to contributions from a single radar in determining the composite reflectivity at May 7, 2019, 4 UTC, over the Central US, for altitudes of a) 2.6, b) 5.0, c) 7.5 and d) 10.0 km. White colors indicate that none of the radars provided data for that part of the composite. Note that the values are dependent on the scanning strategies that are used for different radars, and thus could could vary in time. The smaller the maximum elevation angle that is used (small maximum angles are used for instance when no precipitation is present within the radar range), the larger the 'cone of silence', and thus the larger the area surrounding a radar for which data from other radars must be used.

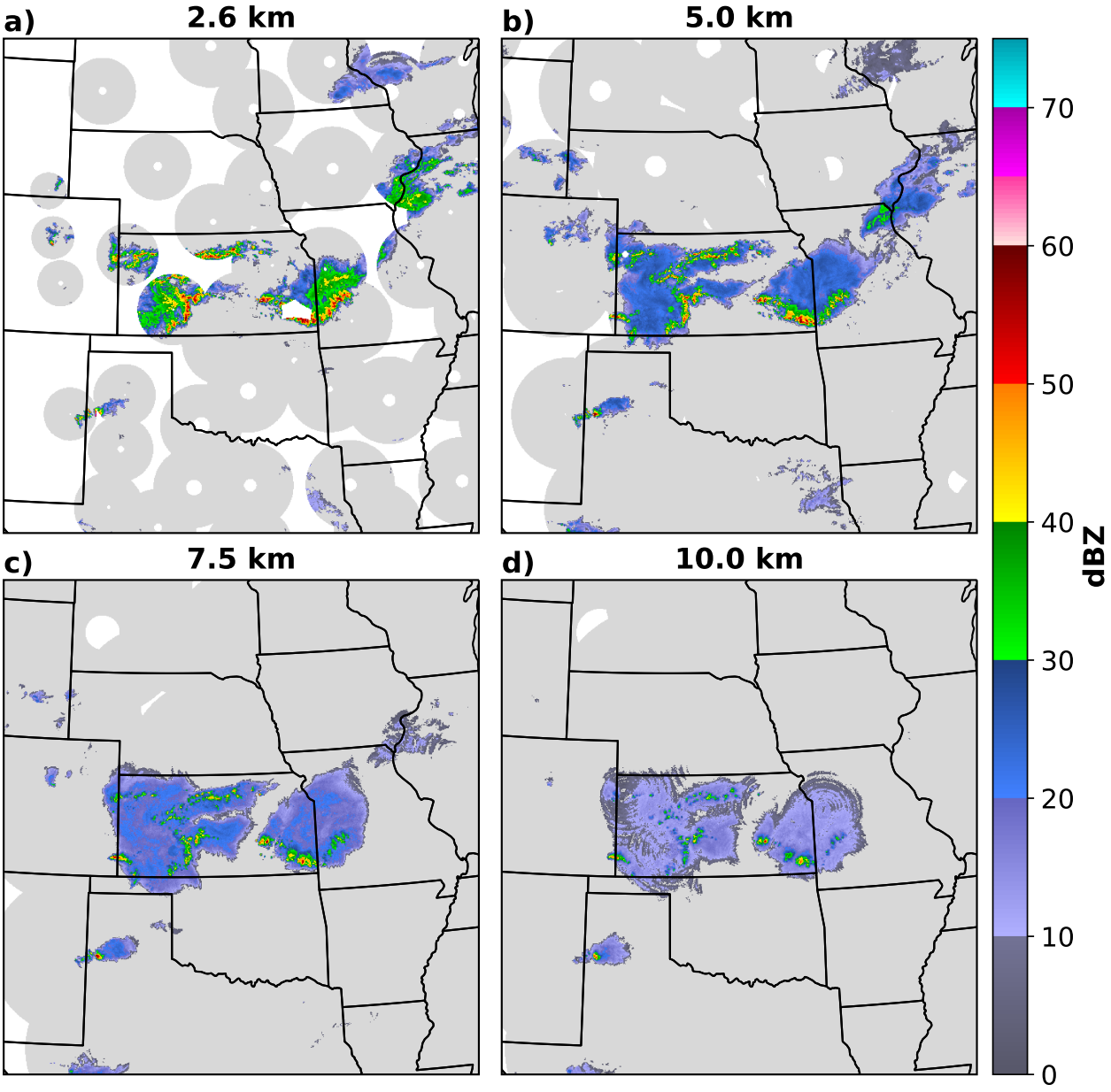

Figure 3.8: Composite reflectivity (quality-controlled) at May 7, 2019, 4 UTC, over the Central US, for altitudes of a) 2.6, b) 5.0, c) 7.5 and d) 10.0 km. White colors indicate that none of the radars provided data for that part of the composite. Light grey indicates reflectivity values below 0 dBZ.

3.5 Factors complicating comparison of observed and simulated reflectivity

In addition to the artefact mentioned in section 3.4.2.5, there are other factors complicating the comparison between observed and simulated reflectivity. This section provides an overview of the most important complicating factors, that require consideration when interpreting the results in chapters 5 and 6.

3.5.1 Attenuation by precipitation

The radar beam will get attenuated by air molecules along its path, and if present, also cloud and precipitation particles (Yuter 2002). Gaseous attenuation by air molecules, which is dominated by oxygen, is usually corrected for automatically in the radar's signal processor. This is not the case for cloud and precipitation particles, for which attenuation could thus influence the reflectivity composites.

For radar wavelengths $\geq$ 5 cm (C- and S-band radars, see table 3.1), the attenuation caused by cloud

droplets ($\leq$ 0.2 mm) is sufficiently minimal to be ignored. Attenuation in rainfall and snow is a function of radar wavelength, temperature, particle type and particle-size distribution. At reflectivities $>$ 40 dBZ, which can occur within heavy rainfall, attenuation can become significant at C- and X-band wavelengths. For S-band radars, significant attenuation can occur when the beam passes through regions containing hail or exceptionally heavy rainfall ($\zeta > 55$ dBZ).
Figure 3.9 shows calculated specific attenuation as a function of reflectivity for rain for wavelengths of 3.2 (X-band), 5 (C-band) and 10 (S-band) cm. For a significant but still relatively small specific attenuation of 0.01 dB/km, we see that for the X-band wavelength this is already reached for reflectivities below 40 dBZ, while for the S-band wavelength this requires about 60 dBZ. At this point, complete attenuation ($>$ 10 dB/km) occurs already for X-band radars, with very substantial attenuation of more than 1 dB/km for C-band radars. Given that reflectivities above 60 dBZ can be observed in intense precipitation cores (which is probably however not purely rain), it is clear that attenuation by precipitation is a very serious problem for X- and C-band radars, while it is rather limited for S-band radars. This is one of the main reasons for performing part of the comparison between modelled and observed convection over the United States (with the S-band US NEXRAD system), instead of over Europe, as discussed in more detail in section 6.1.2.

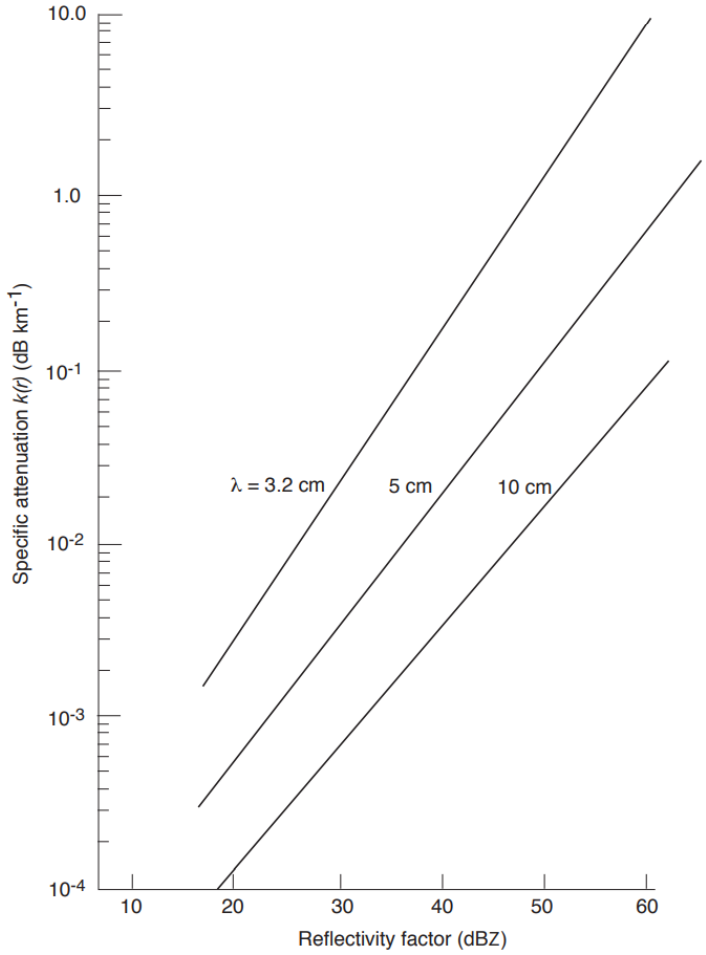

Figure 3.9: Calculated specific attenuation versus reflectivity at $\lambda = 3.2$, 5, and 10 cm. Computations assume $T = 18$ C and Laws and Parson drop size distribution. From Yuter (2002), based on Doviak and Zrnić (1993).

3.5.2 Nonstandard refraction

As explained in section 3.4.2.3, estimation of the radar beam height is based on the Effective Earth's Radius Model, which assumes a certain profile for the index of refraction ('standard refraction', with a constant vertical gradient of the index of refraction). In the case of large temperature and/or moisture inversions, the vertical gradient of refractivity is anomalously large. This causes the radar beam to be bent downward more sharply than under standard refraction, a situation referred to as anomalous propagation. As an example, computed beam paths for a sharp near-surface temperature inversion (below 0.1 km) are shown in figure 3.10, showing that especially the lower elevation angles can be strongly affected, with the possibility that the beam reaches the ground.
In this case of nonstandard refraction, using the Effective Earth's Radius Model leads to overestimation of

the beam altitude. Meteorological conditions associated with moisture and temperature inversions include nocturnal radiation cooling, advection of warm dry air over cooler bodies of water, and deposition of cool moist air at the surface by downdrafts in precipitating storms (Yuter, 2002).
Pronounced nonstandard refraction leads to the appearance of large regions of 'ground clutter' (echoes from objects on the ground) in radar imagery. These can be removed by quality control, but the effect of nonstandard refraction on altitude estimates for other echoes remains, and is not corrected for.

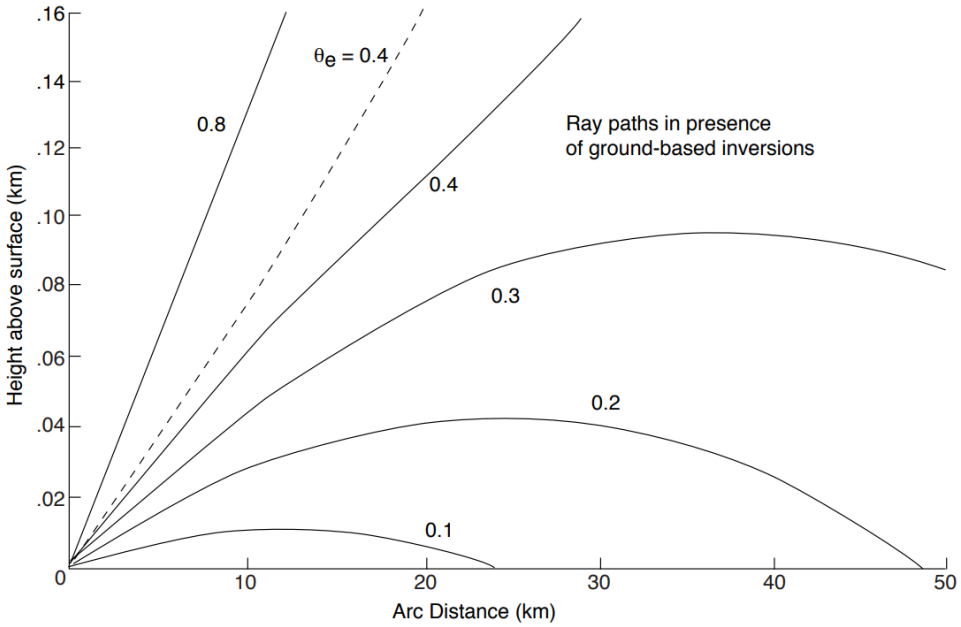

Figure 3.10: Ray paths (solid lines) in arc distance coordinates for radar beams of different elevation angles computed in an atmospheric model with a surface-based temperature inversion to 100-m altitude. The arc distance is the great circle distance along the surface of a sphere with a radius 4/3 times that of the earth. The curvature of a sphere with a 4/3 earth radius compensates for the standard refraction in the atmosphere such that in a height-arc distance coordinate system, a standard atmosphere ray path (i.e., no inversion) is nearly a straight line (dashed line). From Yuter (2002), originating from Doviak and Zrnić (1993).

3.5.3 Bright band

The bright band is a radar signature of the melting layer; a narrow horizontal layer of stronger reflectivity in precipitation at the level in the atmosphere where snow melts to form rain (AMS glossary 2019).
A first factor responsible for its occurrence is the tendency of ice crystals to aggregate and form larger snowflakes when temperatures approach the 0°C level, leading to an increase in reflectivity towards the melting level. As these snowflakes cross the melting level, melting starts, and a water film begins to form on the melting snowflake. Due to the difference in dielectric factor for water and ice, the reflectivity of this snowflake may increase by as much as 6.5 dB.
Further melting occurs below the melting level, resulting in rain drops that are smaller and have a larger fall velocity, causing a decrease in their number density. The combined effect of smaller particles and a lower number density explains the decrease in reflectivity below the melting level, such that a small band of higher reflectivity is established around the melting level, usually centered around 100 m below the 0°C level.

The bright band is observed primarily in stratiform precipitation, as the strong convective currents in active showers and thunderstorms tend to destroy the horizontal stratification that is essential for creating and sustaining a bright band. An example of a bright band in the composite reflectivity is shown in figure 3.11.
As mentioned in section 3.3.1, the bright band will not appear in simulated reflectivity. This needs to be considered when comparing simulated with observed reflectivity.

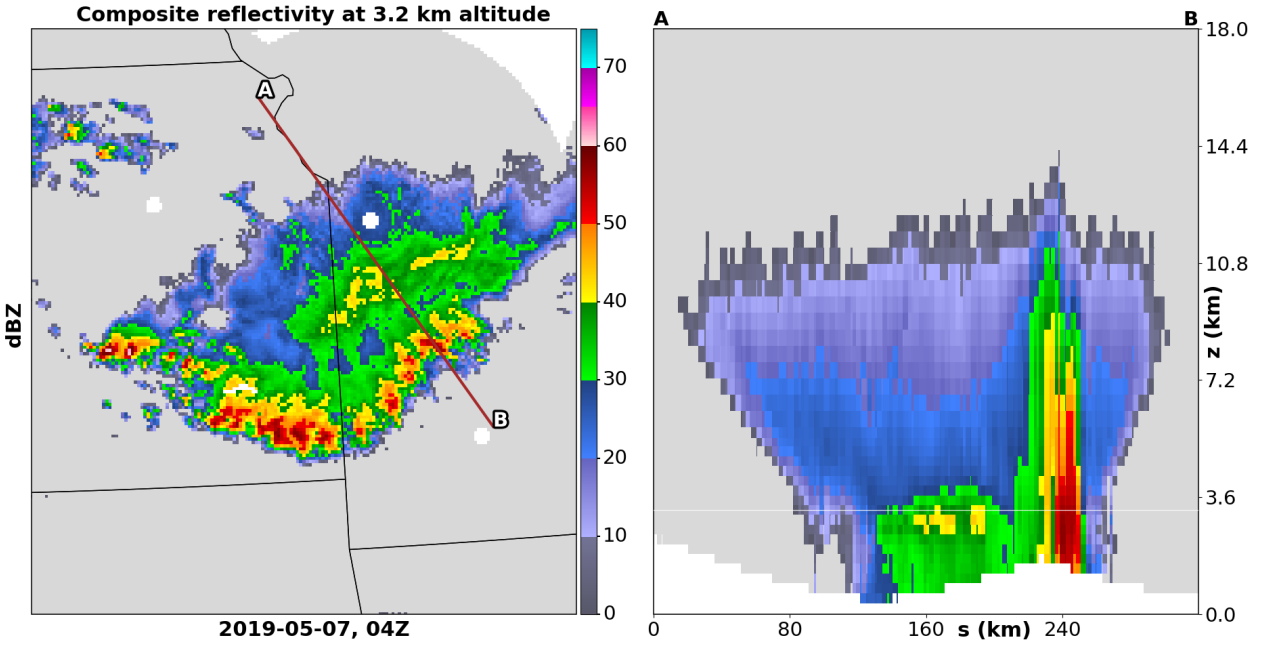

Figure 3.11: Example of a bright band signature, apparent in a cross section through the composite reflectivity, at about 3 km altitude in the stratiform part of a squall line over the states Kansas and Missouri.

3.5.4 Nonprecipitation radar returns

Besides ground clutter, mentioned in section 3.5.2, there are other types of nonprecipitation (NP) radar echoes. These other NP radar echoes include electromagnetic interferences from man-made telecommunication transmitters and sun spikes, biological scatterers (birds, bats and insects), and sea clutter (Tang et al. 2014). As an example, composite reflectivity without quality control is displayed in figure 3.12, showing large regions of nocturnal biological echoes.

These NP echoes should preferentially be removed, to prevent them from appearing in the composite reflectivity. This process is called quality control (QC), and should remove as little actual precipitation echoes as possible. For the US NEXRADs, a relatively simple custom QC algorithm has been developed and applied, described in appendix B.

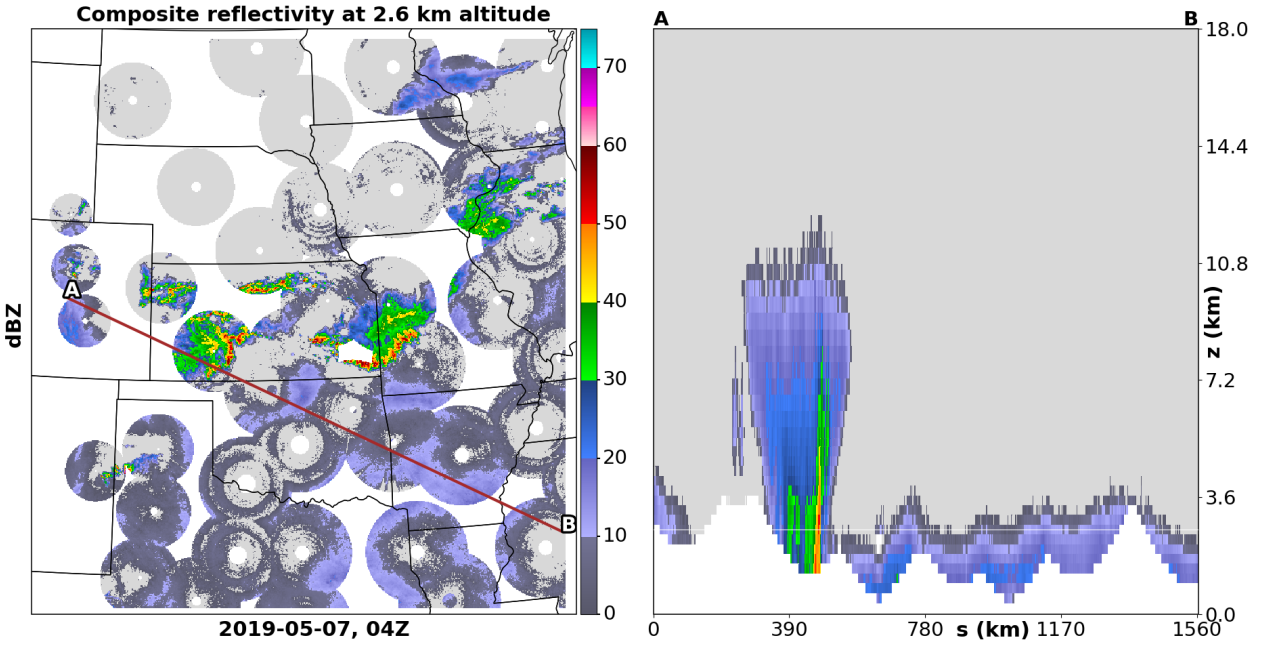

Figure 3.12: Composite reflectivity at 2.6 km altitude (left) at May 7, 2019, 4Z, without applying quality control to remove nonprecipitation echoes. Also shown in a vertical cross section (right). Cf. figure 3.8a), for which quality control has been applied.

3.5.5 Partial coverage of radars

Given that the radar beam altitude increases with increasing range (under normal refraction), the availability of reflectivity measurements at lower altitudes is limited to annular regions surrounding radars. Figure 3.7a) shows this very clearly for the US NEXRADs for 2.6 km altitude. This limited coverage hinders the comparison between observed and simulated reflectivity at these lower altitudes.

In mountainous regions radar coverage can also be limited by beam blocking due to mountains, which can cut away certain sectors from a radar scan. These sectors should be excluded from the compositing process, to prevent contamination of the composite reflectivity. Here that was realized by excluding three radars for which substantial beam blocking occurred from contributing to the Central US reflectivity composite.

3.5.6 Other factors

A few other factors that could lead to errors in measured reflectivity include the precision of measured $\bar{P}_r$ (eq. 3.7, error typically $\sim$1 dB), and the calibration of $\bar{P}_r$ (error typically $\sim$2 dB) (Yuter, 2002).

Chapter 4

Data and methods

This chapter first describes the two main domains used for the model runs in 4.1, and the data used for the reflectivity composites in section 4.2. These domains are centered over the Netherlands and the Central United States.
Given that the coverage of dutch radars is limited, satellite images are included as an additional source of observations of convection, and are described in section 4.3. Further, initiation and sustenance of convection is strongly dependent on the vertical structure of the troposphere. Therefore, area-averaged skew-T log-P diagrams (displaying temperature and dew point as a function of pressure) have been generated to compare output of model configurations between themselves, and the method for this is described in section 4.4.
Finally, the cases that have been analysed are described in section 4.5.

4.1 Model domains

4.1.1 The Netherlands

Simulations for the Netherlands have been performed on a domain that is centered at the Netherlands at 52.5° N, 0° W, and that has horizontal dimensions of about 2000×2000 km (800 grid points in both x and y direction, with 2.5 km horizontal resolution). It thus covers a large part of western Europe. The model grid has a lambert conformal conic projection, with reference longitude and latitude at 0.0° E and 52.5° N, and both standard parallels at 52.5° N.
A few simulations have been performed with a higher horizontal resolution, which for computational reasons have been limited to a subset of the domain described above.

4.1.2 Central United States

The domain over the Central United States is centered at the state of Kansas at 37.5° N, −100° W, and it has the same horizontal dimensions as the grid for the Netherlands. The reference longitude and latitude are −100° W and 37.5° N, with both standard parallels at 37.5° N. The complete domain is shown in for instance figure 3.8.

4.2 Radar composites

4.2.1 The Netherlands

Reflectivity composites for the Netherlands are based on data from three precipitation radars operated by the KNMI, located in De Bilt, Den Helder and Herwijnen. Effectively only two radars where operating at the same time however, as the location Herwijnen has replaced De Bilt in January 2017, when the KNMI replaced both its single-polarization radars by dual-polarization radars. Archived data is freely available at `https://data.knmi.nl/datasets?q=radar`. An overview of the scanning strategies that the KNMI used for the old and new radars is provided in table 4.1.
While the elevation angles under which is scanned are almost equal for both scanning strategies, the order in which they are scanned is completely different. For the new radars one could effectively divide the volume in two subvolumes, that consist of series of scans for which the elevation angle decreases in time. Due to this fact, creating CAPPIs as described in section 3.4.2.4, with interpolation between subsequent scans in the vertical, leads to averaging between reflectivities that are obtained at times that differ by about 2.5 minutes. In case of fast-moving precipitation this leads to the undesired data smoothing described in the introduction

of section 3.4. For this reason we preferred to use data from the old radars, except for cases with slow-moving precipitation, for which the data smoothing is less pronounced.

Table 4.1: Elevation angle and start time (relative to the start of the volume) for every scan in a single radar volume of the old (columns 2 and 3) and new (columns 4 and 5) radars.

Scan	$\theta(^\circ)$	$\mathbf{t_{start}}$ **(MM:SS)**	$\theta(\theta)$	$\mathbf{t_{start}}$ **(MM:SS)**
1	0.3	00:12	12.0	00:16
2	0.4	00:40	8.0	00:28
3	0.8	01:01	4.5	00:40
4	1.1	01:22	2.0	00:54
5	2.0	01:42	0.8	01:11
6	3.0	02:03	0.3	01:28
7	4.5	02:19	25.0	02:01
8	6.0	02:35	20.0	02:13
9	8.0	02:50	15.0	02:25
10	10.0	03:04	10.0	02:37
11	12.0	03:16	6.0	02:49
12	15.0	03:28	2.8	03:03
13	20.0	03:41	1.2	03:20
14	25.0	03:53	0.3	03:37
15			0.3	03:59

4.2.2 United States

Reflectivity composites for the United States are based on data from the NEXRAD network, operated by the National Weather Service (NWS), an agency of the National Oceanic and Atmospheric Administration (NOAA). This network covers the United States and currently comprises 160 dual-polarization radars. Archived data is freely available, and can be obtained from `http://doi.org/10.7289/V5W9574V`.
Different scanning strategies can be selected by the radar operator, which are named Volume Coverage Patterns (VCPs). An example of such a VCP was already shown in figure 3.6. Volume completion times typically range from about 4.5 to 10 (in case of little precipitation) minutes.

Given that the model domain does not span the whole United States, only a subset of radars is needed. A radar is selected to contribute to the composite when its location is not more than 150 km away from the domain boundaries. Three of the radars that satisfied this condition where excluded from contribution because of substantial beam blocking by mountains, as described in section 3.5.5.
Because the archived data is not yet filtered for nonprecipitation echoes, it was necessary to do that within this project. The procedure for this is described in appendix B.

4.3 Satellite images

Because the radar composites span only an area slightly larger than the Netherlands, it was decided to also include data from the second generation of satellites operated by EUMETSAT in the comparison, which is available for the whole model domain. These geostationary satellites have 12 spectral channels, and provide most data (11 channels) at a resolution of 3 km for the sub-satellite point above the equator (with lower resolution towards the boundaries of the part of the earth that is scanned). The exception is the HRV channel, which has a resolution of 1 km. Data is provided every 15 minutes. As with radar data, the satellite data is reprojected onto the HARMONIE grid.

4.4 Box-averaged skew-T log-P diagrams

Skew-T log-P diagrams are plotted to explore the effect of different model configurations on the vertical profiles of temperature and moisture, which are both very important for shower/thunderstorm initiation and sustenance. These skew-T log-P diagrams display temperature and dew point as a function of pressure, with often additional curves added that represent lines of constant mixing ratio, and dry and wet adiabats. Because these profiles will vary from point to point, they have sometimes been averaged over a rectangular grid box here, in order to get profiles that are representative for larger regions.

For temperature, the box-averaged value at a certain height h_k (AGL) is calculated as

$$\bar{T}(h_k) = \frac{1}{N} \sum_{i=1}^{N} T_i(h_k), \tag{4.1}$$

with N the number of grid points within the box (the summation is in fact over two dimensions). For specific humidity the same procedure is used. Dew points are subsequently computed from the box-averaged specific humidities.
For pressure this procedure is different. First, the pressure at the mean surface elevation within the box is calculated, as the average pressure within the box at that altitude. Next, pressures at higher levels are calculated by integrating the hydrostatic balance, using the box-averaged temperature profile. Calculating pressure in this way ensures consistency with the hydrostatic balance and ideal gas law.

4.5 Case selection

4.5.1 The Netherlands

Except for the two cases of 10 September 2011 and late October 2017 presented in Tijm (2018), with known issues with simulating convection, additional cases for comparison have been selected based on known occurrence of showers/storms. Table 4.2 provides an overview of all 11 cases that have been considered in this comparison, including a short description of what happened.

Table 4.2: Cases with showers/storms over the Netherlands and/or surroundings that have been considered in the comparison between model and observations.

Case (yyyy-mm-dd)	**Description**
2008-06-22	Severe thunderstorms including supercells producing hail up to about 5 cm
2009-07-21	Severe thunderstorms including supercells producing hail up to about 5 cm
2010-07-10	Severe thunderstorms evolving into a squall line
2011-09-10	Severe thunderstorms including a supercell that produced hail up to about 5 cm
2013-11-03	Strong thunderstorms including supercells during a cold air outbreak, producing at least 3 tornadoes
2014-06-09	Severe thunderstorms, including supercells and an intense squall line that evolved into a severe bow echo
2015-08-24	Severe thunderstorms including supercells, of which one produced a tornado
2015-08-30	Severe thunderstorms including supercells that produce hail up to 8 cm
2016-06-23	Severe thunderstorms including supercells, of which one produces hail up to 10 cm
2017-10-29	Shallow showers during a cold air outbreak
2018-05-29	Strong slow-moving thunderstorms that locally dump large amounts of rain

4.5.2 United States

For this domain only cases with severe thunderstorms have been considered. These 12 cases are shown in figures 6.1-6.3.

Chapter 5

Issues apparent in case studies

5.1 Underestimation of number of shallow showers

Only one case with shallow showers has been considered, as indicated in table 4.2. The reason is that the issue of the underestimation of the number of shallow showers was already clearly established by Tijm (2018). The focus here is therefore mainly on understanding its cause. First however, its appearance on 29 October 2017 is presented.

5.1.1 Overview

Figure 5.1 shows observed and simulated reflectivity on 29 October 2017, 12Z. Figure 5.2 shows the HRV (High-Resolution Visible) satellite channel for the same time, together with the simulated net downward longwave radiation flux at the top of the atmosphere (TOA). Though certainly not one-to-one comparable, both images have as similarity that regions with clouds appear brighter than regions without clouds, making them suitable for the identification of clouds.
Both figures clearly show that the model is not able to simulate the pattern of open cell convection that was present in reality. Section 5.1.2 discusses the influence of the shallow convection scheme on the development of these shallow showers.

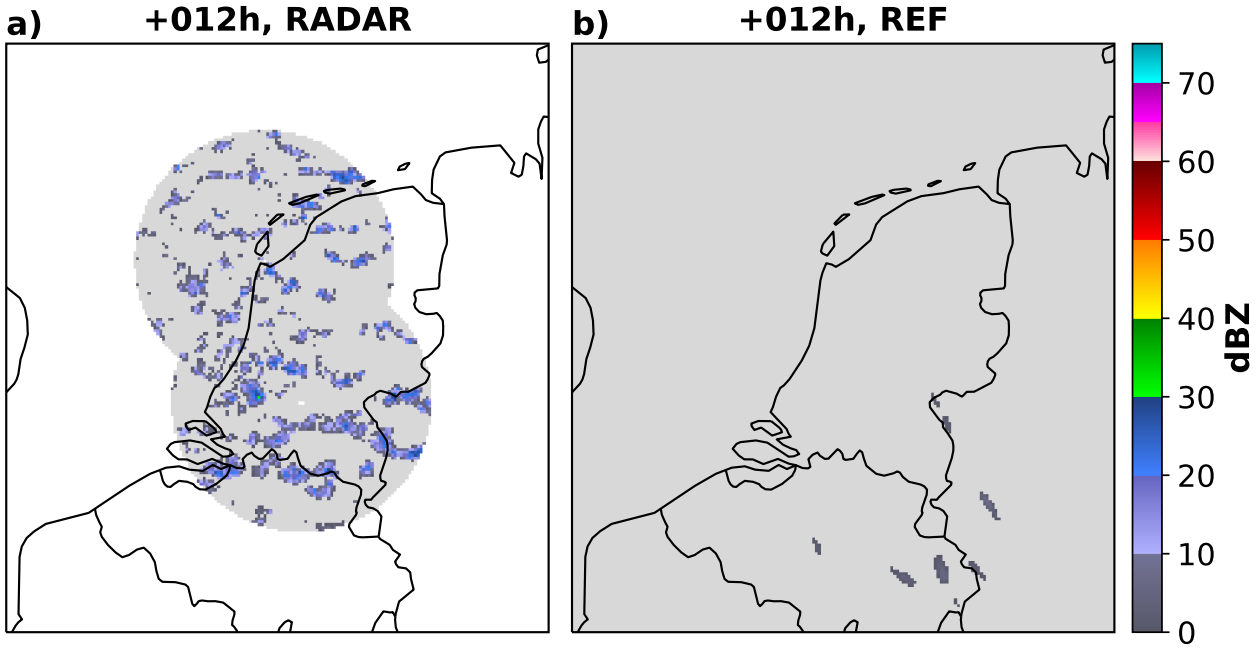

Figure 5.1: Observed (a) and simulated (b) reflectivity at 1.4 km altitude at 2017-10-29, 12Z. Simulated reflectivity is obtained by running the REF configuration, starting at 2017-10-29, 00Z.

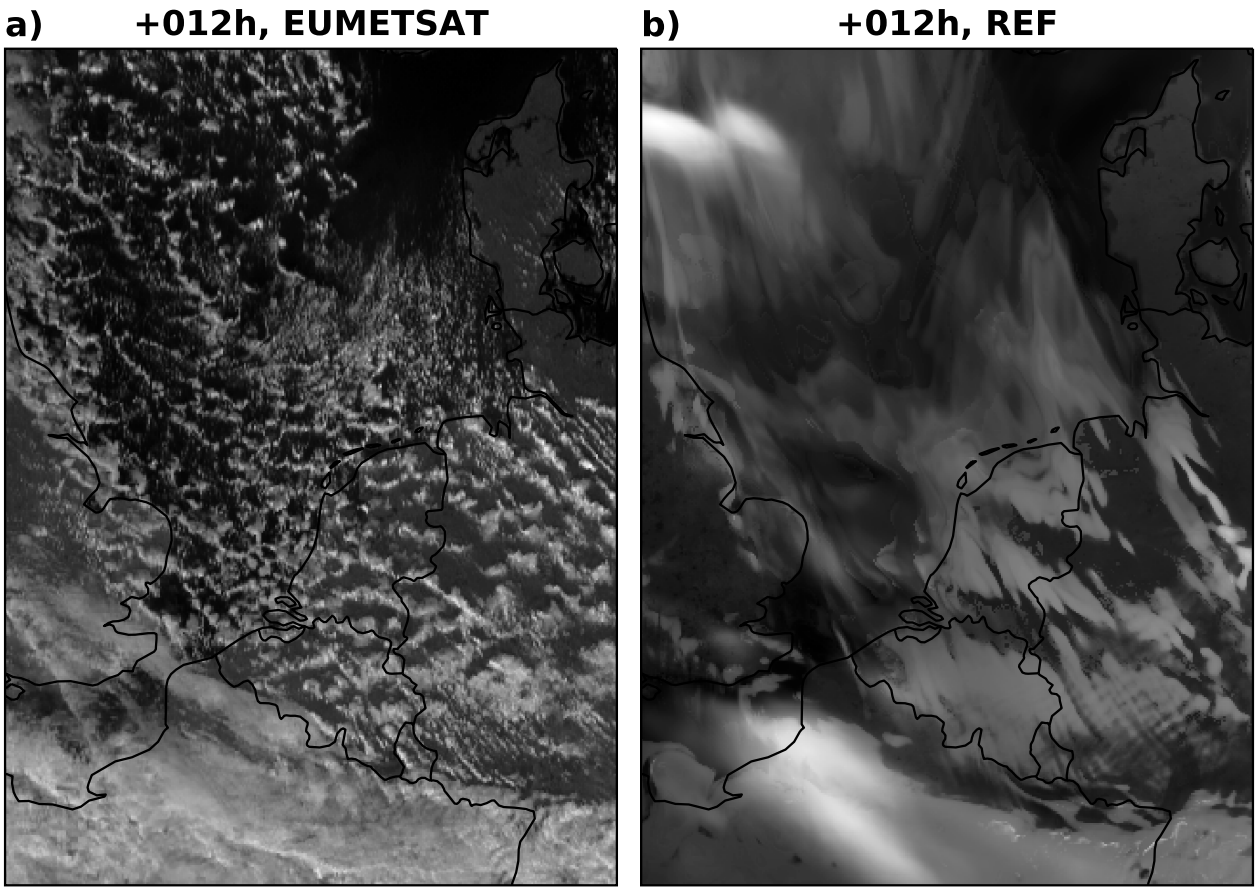

Figure 5.2: HRV satellite channel (a) and simulated net downward longwave radiation flux at the TOA (b) at 2017-10-29, 12Z. The image in (b) is obtained from the same run as in figure 5.1.

5.1.2 Influence of shallow convection scheme

Figures 5.3 and 5.4 show simulated reflectivity and net downward longwave radiation flux for the REF, NOHAR, NOSHAL and NOHAR_NOSHAL (cf. section 2.5) configurations. These figures immediately show that disabling the shallow convection scheme results in simulating many more shallow showers. Thus apparently, the shallow convection scheme changes the vertical structure of the atmospheric boundary layer (ABL) in such a way that initiation of explicitly resolved convection is suppressed.

To examine this, a rectangular box is positioned over the North Sea in the region just upstream of where initiation of shallow showers occurs in the NOSHAL configurations, and is displayed in figures 5.3 and 5.4. Box-averaged temperature and dew point profiles have been determined, and are displayed in figure 5.5. The two most striking differences between the configurations are the lower temperatures at the top of the ABL, and a dew point profile that follows more closely the lines of constant mixing ratio in the ABL in the SHAL (with shallow convection scheme enabled) configurations. Also, near-surface dew points (lowest data points are at about 13 m AGL, around lowest hybrid model level) are slightly higher in the NOSHAL configurations. Both the slightly higher near-surface dew points and the slightly lower temperatures at the top of the ABL are favourable for the initiation of convection, making this easier in the NOSHAL configurations.
Compared to the NOSHAL configurations, the temperature profile is clearly smoother at the top and above the ABL in the SHAL configurations, up to an altitude of about 2 km. This is an indication that more mixing takes place in the SHAL configurations at these levels, which in the NOSHAL configurations seems to be limited to the ABL itself. Given that the SHAL configurations greatly underestimate the number of shallow showers, this mixing by the shallow convection scheme should probably be reduced.

Finally, it is clear from figures 5.3 and 5.4 that initiation of the shallow showers is also easier in the NOHAR configuration than in the REF configuration. This is also observed for severe thunderstorms, as described in section 5.3.

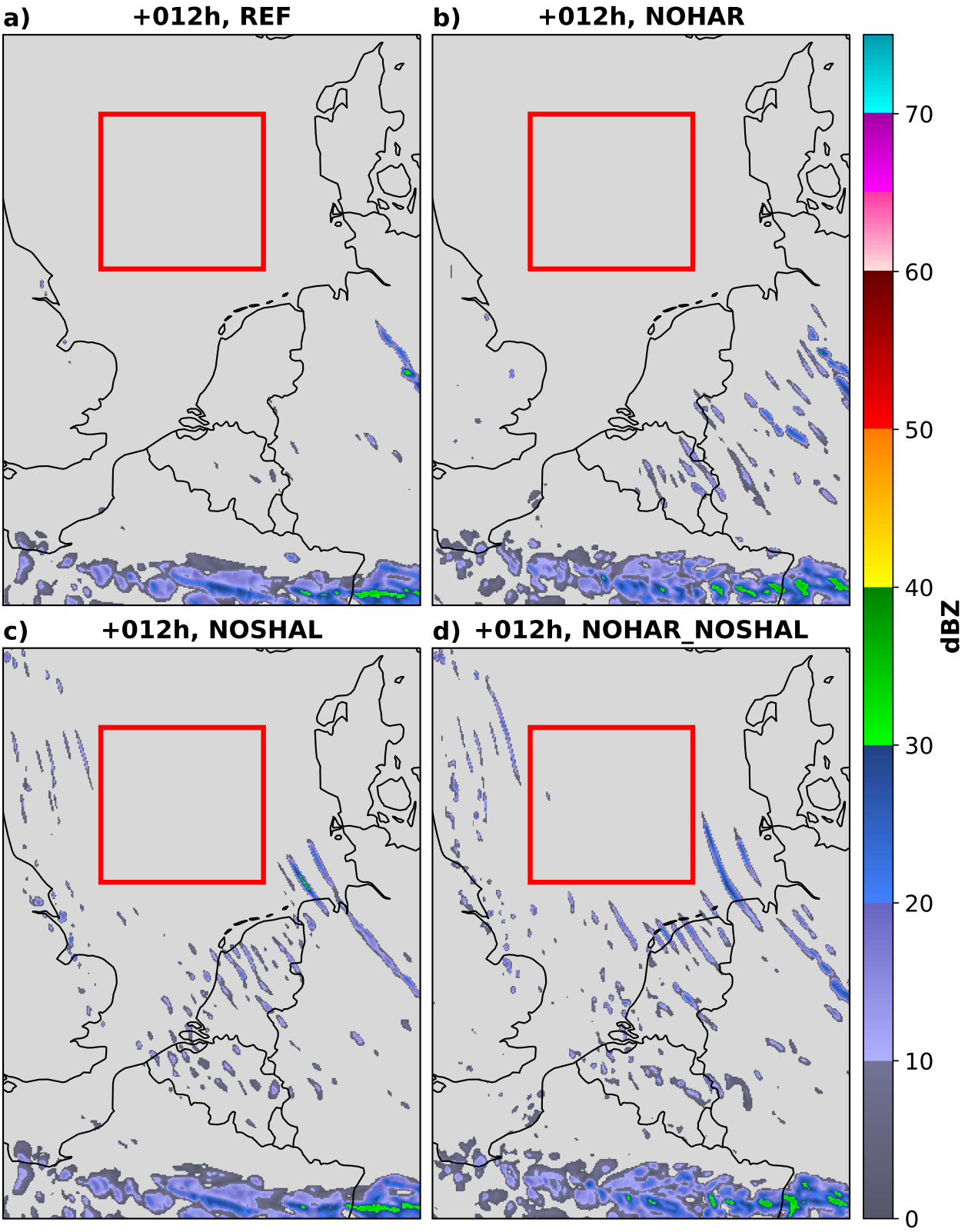

Figure 5.3: Simulated reflectivity at 1.4 km altitude at 2017-10-29, 12Z, obtained from a run with the a) REF, b) NOHAR, c) NOSHAL, and d) NOHAR_NOSHAL configuration. All runs started at 2017-10-29, 00Z. The red box indicates the region for which box-averaged skew-T log-P diagrams are shown in figure 5.5.

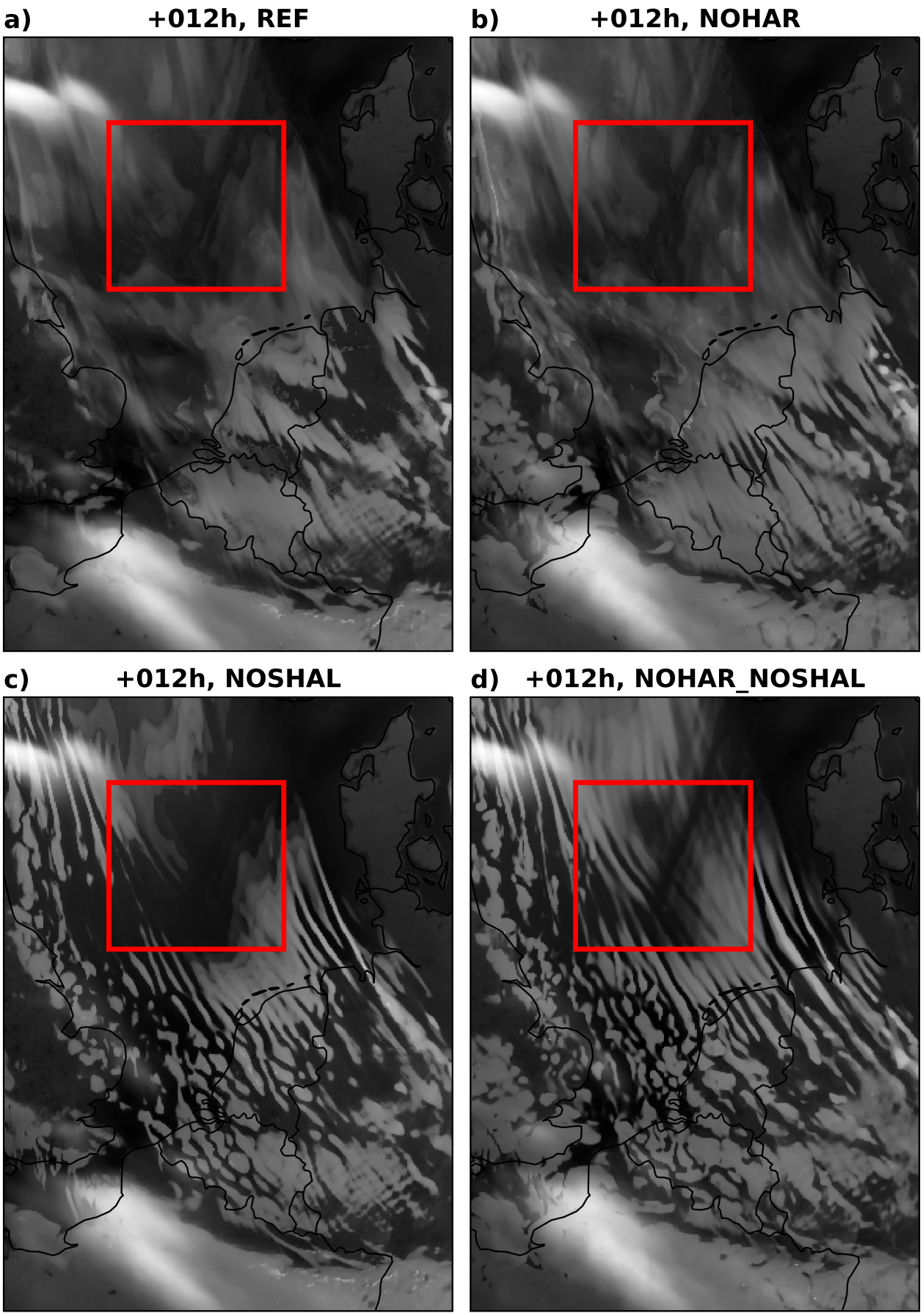

Figure 5.4: Simulated net downward longwave radiation flux at the TOA at 2017-10-29, 12Z. Further details as for figure 5.3.

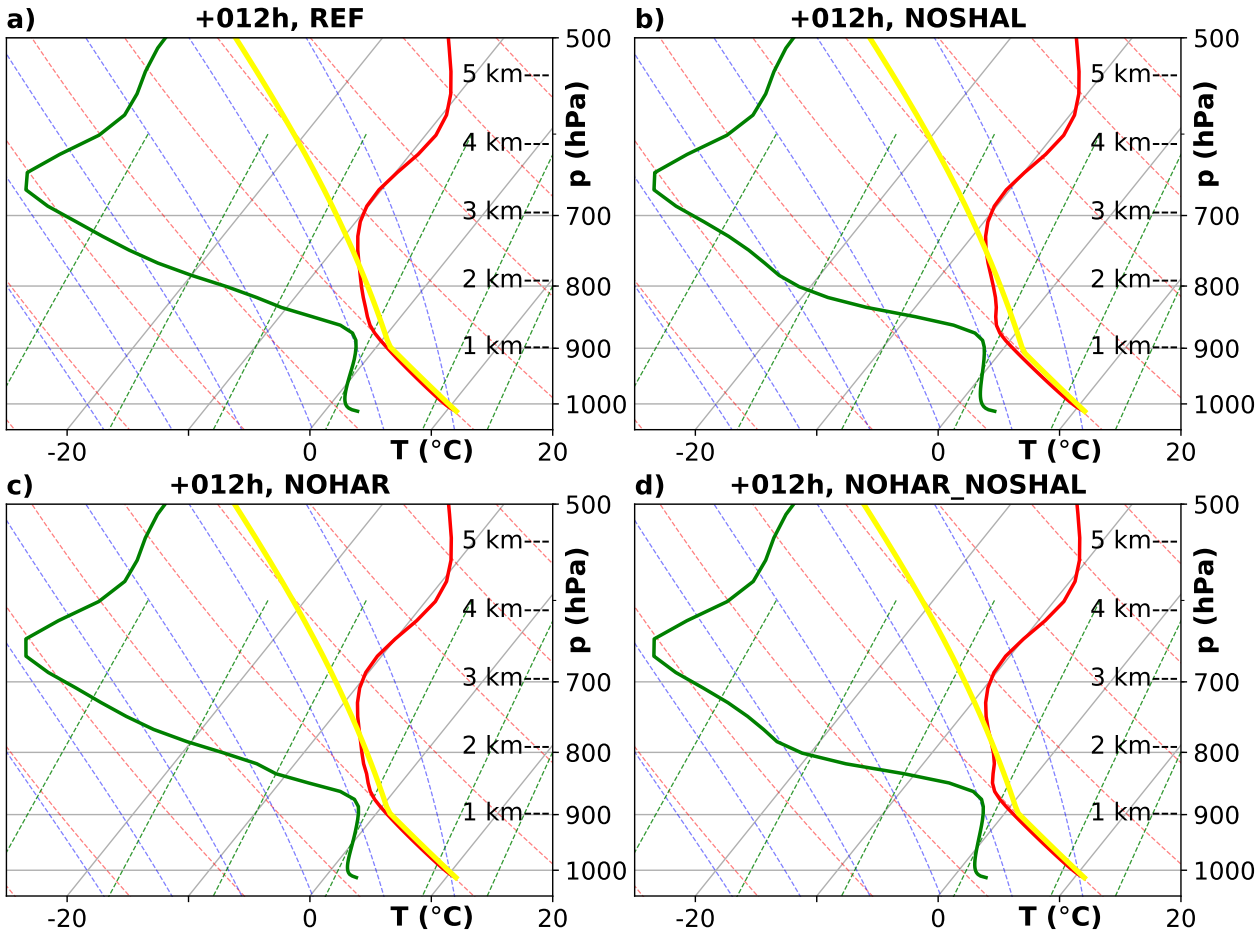

Figure 5.5: Box-averaged skew-T log-P diagrams at 2017-10-29, 12Z, for the red boxes shown in figures 5.3 and 5.4. The red and green thick lines represent profiles of temperature and dew point. Grey lines are lines of constant temperature, green dashed lines are lines of constant water vapour mixing ratio, and red (blue) dashed curves are dry (moist) adiabats. The yellow curve indicates the path of a parcel that is released from the 'surface' (lowest model level at about 13 m AGL), and first travels dry-adiabatically upward until saturation, and then continues moist-adiabatically.

5.2 Too linear structure of simulated shallow showers

In the configurations for which the model does simulate many shallow showers, i.e. the NOSHAL configurations, the model is still not able to simulate the pattern of open cell convection. Figure 5.6 compares data from the HRV channel of EUMETSAT with simulated net downward longwave radiation flux at the TOA in the NOSHAL configuration. The simulated 'satellite image' clearly shows a more linear structure in the clouds than observed in reality. Given the width of these 'cloud streets', the horizontal resolution of the model will of course be important in this, but its effect has not been examined.

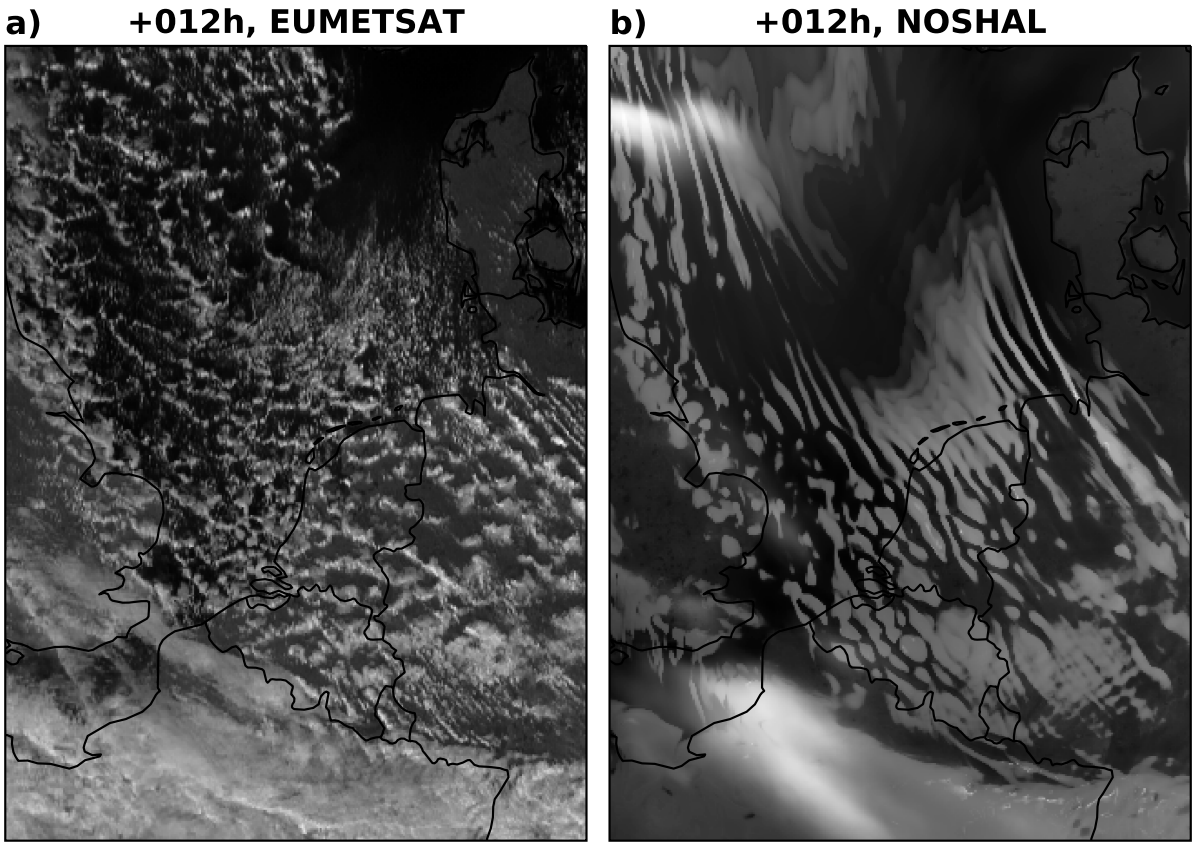

Figure 5.6: HRV satellite channel (a) and simulated net downward longwave radiation flux at the TOA (b) at 2017-10-29, 12Z.

5.3 No initiation of severe thunderstorms in certain cases under HARATU

Tijm (2018) discussed the case of 10 September 2011, where a severe supercell moved from Belgium into the Netherlands, producing hail up to about 5 cm. The REF configuration did not let a severe thunderstorm develop, whereas the NOHAR configuration did. Figure 5.7 shows observed and simulated reflectivity for this case, and another example with lacking initiation of severe thunderstorms in the REF configuration is shown in figure 5.8, for the case of 21 July 2009.
A similarity shared by both cases is that surface-based convection develops in the late afternoon or early evening. Such late initiation implies the presence of a substantial capping inversion, in which case small differences in the vertical structure of the boundary layer, due to the use of a different turbulence scheme, can be critical in determining whether or not storms initiate.

Examination of whether there is a real issue with initiating convection in the REF configuration requires however a much more extensive analysis. Chapter 6 provides a more detailed analysis of simulated precipitation patterns, that also gives some information the number of convective cells simulated by the different configurations. This analysis is however mainly aimed at analysing the issue described in section 5.4, and a good examination of whether there is indeed an issue with initiating convection has yet to be performed.

The last part of this section examines box-averaged skew-T log-P diagrams for the case of 10 September 2011, in an attempt to understand the effect of HARATU on initiation of thunderstorms.

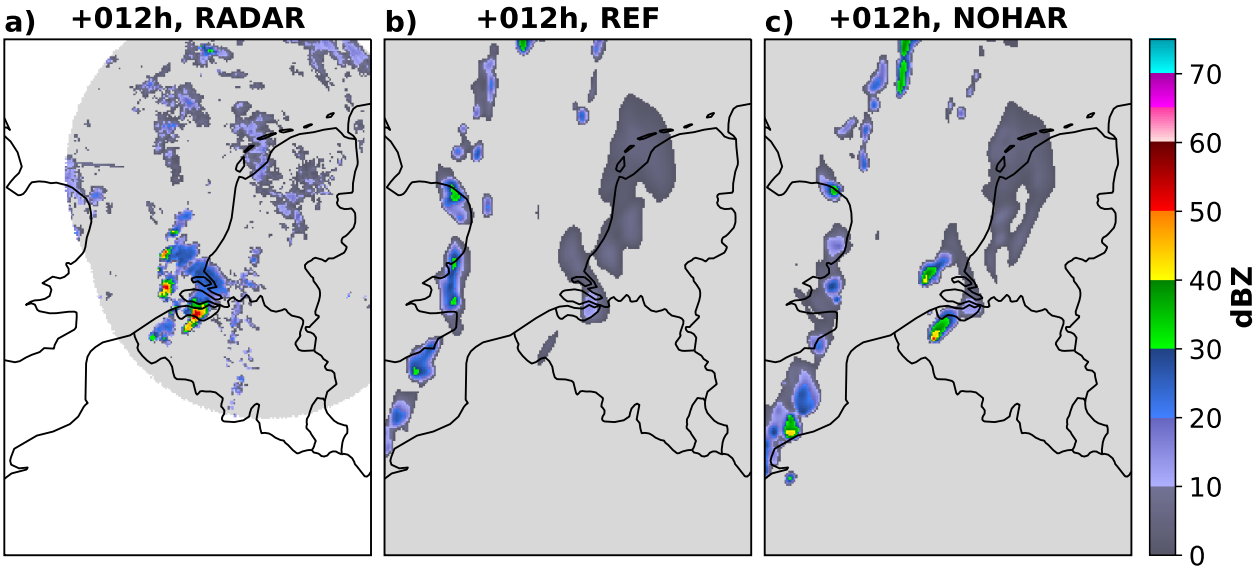

Figure 5.7: Observed (a) and simulated (b and c) reflectivity at 5 km altitude at 10 September 2011, 18Z. Model runs started at 06Z.

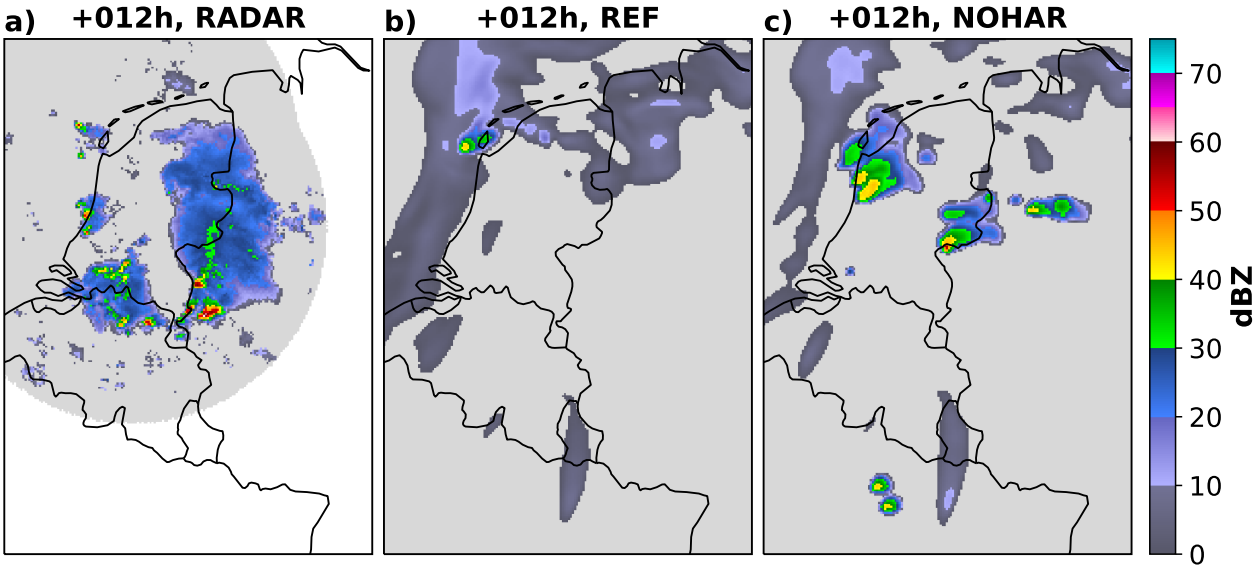

Figure 5.8: As in figure 5.7, but for 21 July 2009, 18Z.

Figure 5.9 shows simulated reflectivity at 0.8 km altitude at 15Z for the REF and NOHAR configurations, about 1 hour before initiation of the severe thunderstorm in northwestern France. It includes a red box, for which box-averaged skew-T log-P diagrams are shown in figure 5.10 for both configurations.
Comparing the diagrams leads to the conclusion that NOHAR has a slightly moister boundary layer than the REF configuration. Though not well visible in figure 5.10, overlaying both diagrams shows on the other hand that the atmosphere is slightly drier in NOHAR in the layer between 1 and 3 km. Regarding temperature, the main difference between the profiles is the presence of weaker temperature lapse rates (vertical gradient of temperature) in NOHAR between about 1 and 2 km altitude, which is just above the boundary layer. These weaker temperature lapse rates lead to higher temperatures between about 1 and 2.5 km altitude.

Together these differences indicate that HARATU produces more mixing at the top of the boundary layer than the old CBR turbulence scheme. A moister boundary layer is favourable for thunderstorm initiation, whereas smaller temperature lapse rates are not. The net effect of differences between REF and NOHAR is apparently positive for thunderstorm initiation in NOHAR for this case. However, concluding whether this is mainly due to these differences in vertical profiles of temperature and dew point, or maybe due to differences in convergence at the surface, requires further examination. That is however beyond the scope of this research.

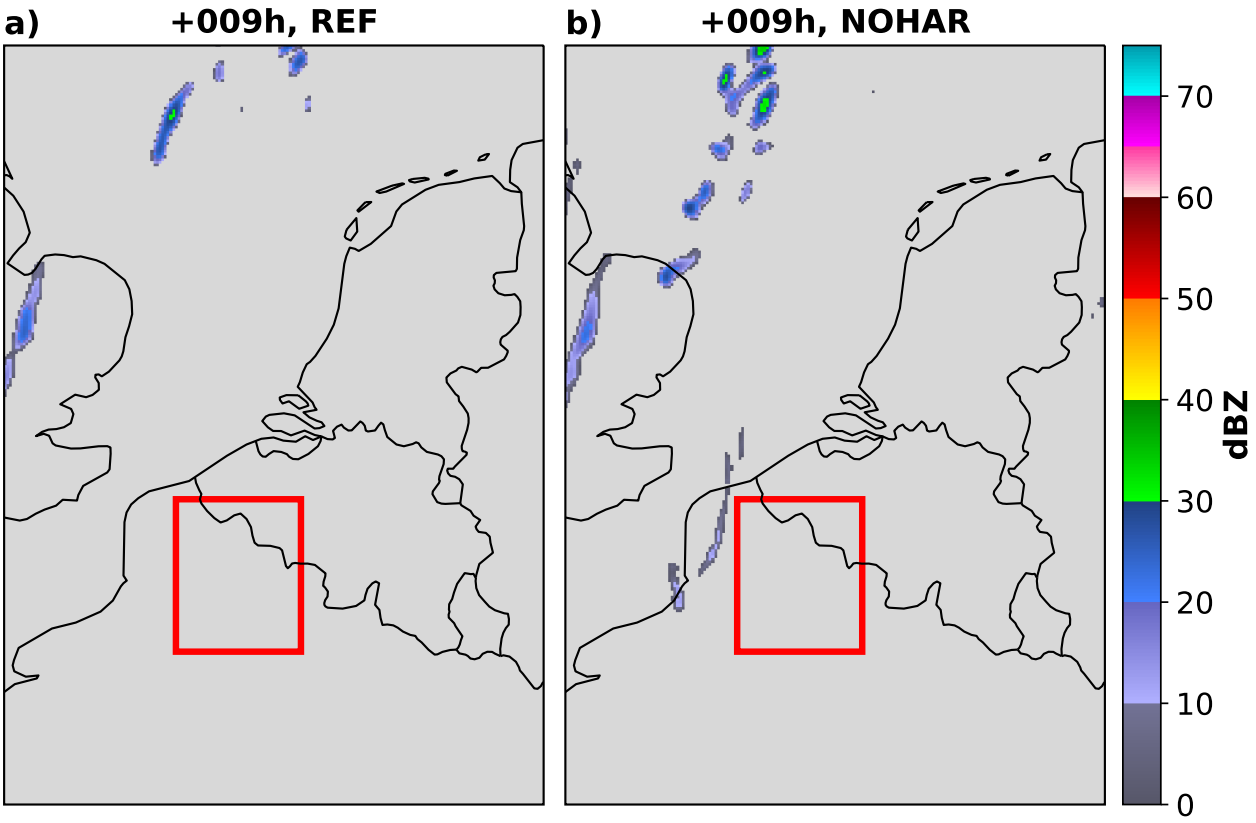

Figure 5.9: Simulated reflectivity at 0.8 km altitude at 10 September 2011, 15Z. The red box indicates the region for which box-averaged skew-T log-P diagrams are shown in figure 5.10. Model runs started at 06Z.

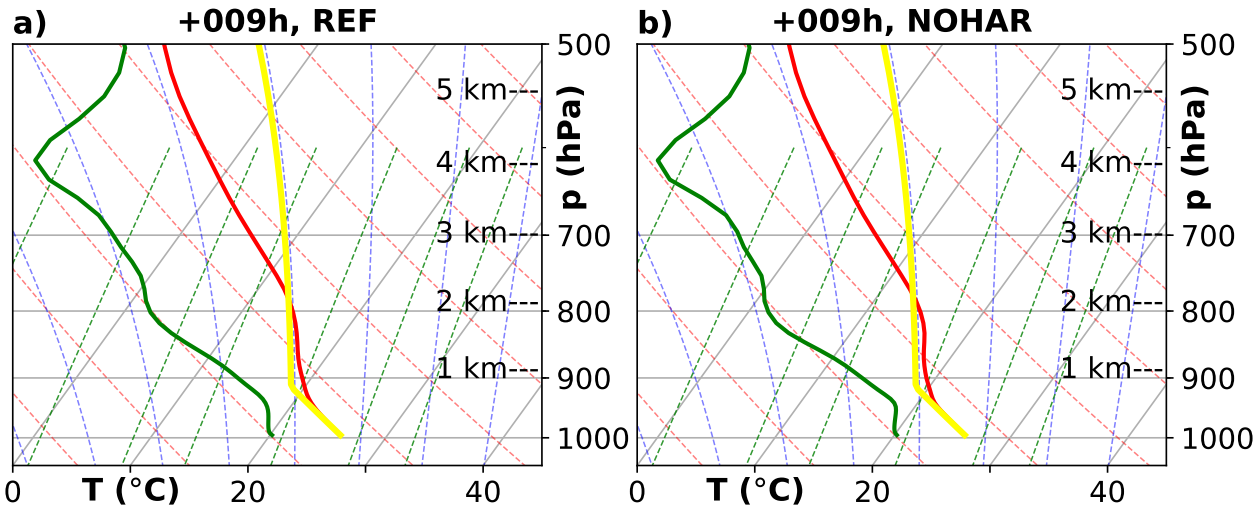

Figure 5.10: Box-averaged skew-T log-P diagrams at 2011-09-10, 15Z, for the red boxes shown in figure 5.9.

5.4 Too small (large) areas with weak (intense) precipitation

Examination of all 24 cases clearly showed that the model simulates smaller (larger) regions with weak (intense) precipitation than observed in reality. As an example, figure 5.11 shows observed and simulated reflectivity for a case with an extensive squall line over eastern Kansas and Oklahoma. The squall line is captured by the model, but there are large discrepancies between observed and simulated sizes of regions with weak and intense precipitation. This issue is analysed further in chapter 6.

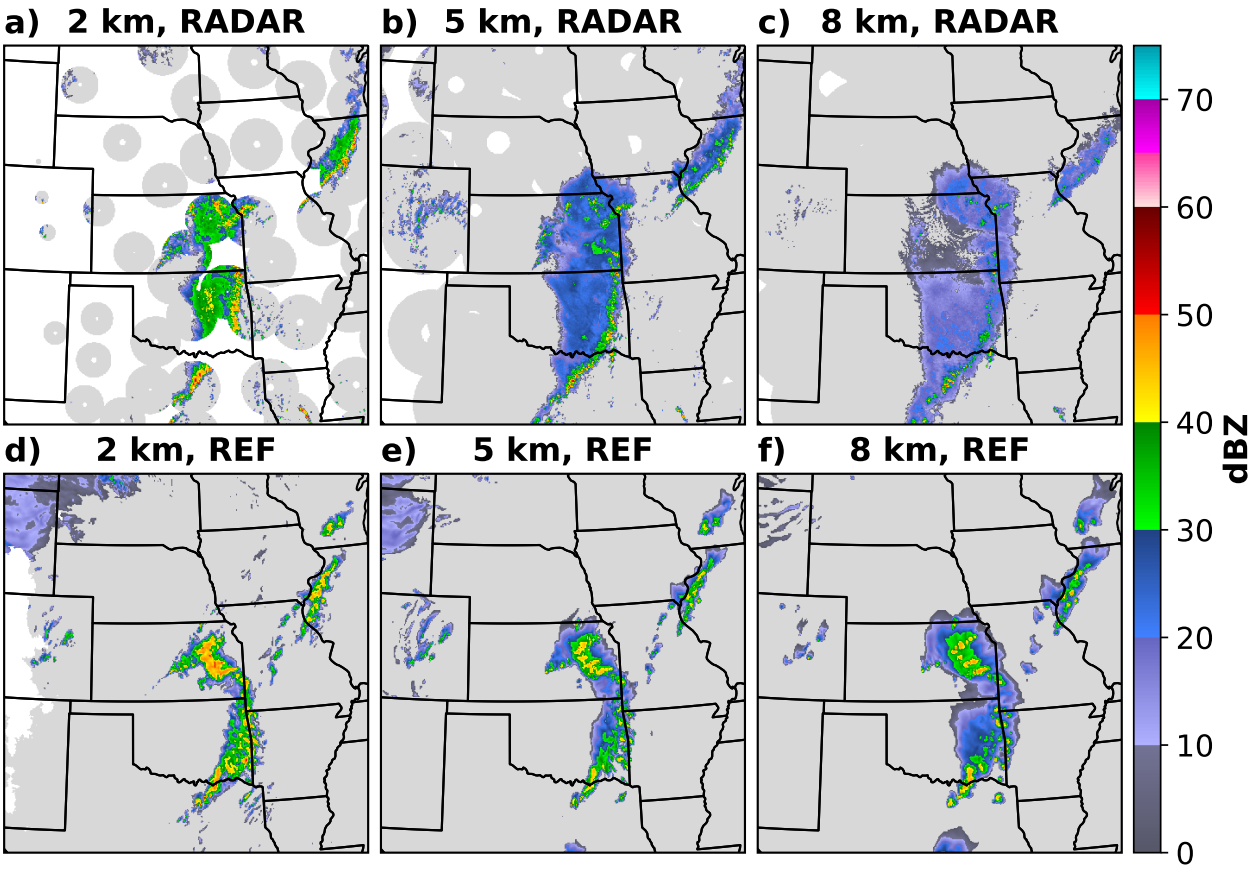

Figure 5.11: Observed (a, b and c) and simulated reflectivity (d, e and f) at 18 May 2019, 18Z, for altitudes of 2, 5 and 8 km. Model runs started at 06Z.

5.5 Intense convection reaching model top in higher-res runs

Running the REF configuration at 1.25 km horizontal resolution for the case of 9 June 2014 showed peculiar behaviour, with precipitation in some intense storms reaching extreme heights. The most extreme example is shown in figure 5.12, where precipitation is present even at the highest hybrid model level, centered at about 30 km altitude.

For precipitation to reach that far into the stratosphere, there must be substantial (to minimise entrainment of dry stratospheric air) upward motion above the tropopause. Figure 5.13 shows vertical velocity at the model top and in a vertical cross section. There indeed is substantial upward motion in the stratosphere, and its magnitude is almost independent of altitude in the upper three model levels.

It seems that this issue must be related to the formulation of the upper boundary conditions, but this has not been further analysed.

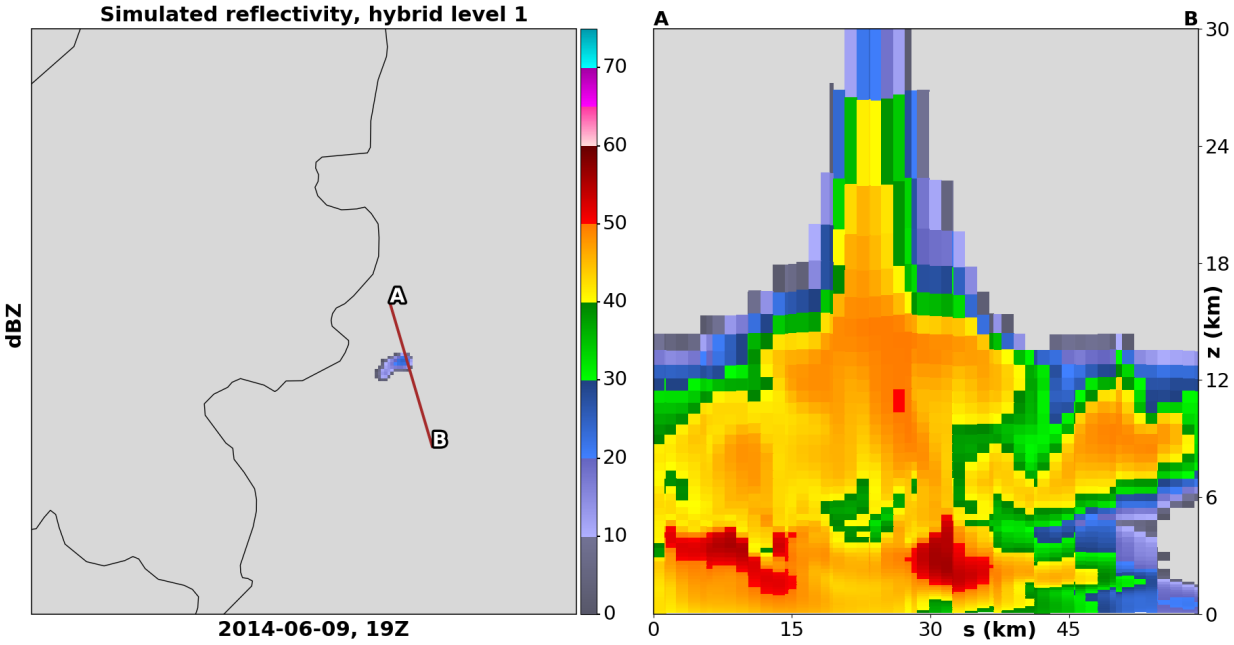

Figure 5.12: Simulated reflectivity at the model top from a run with the REF configuration at 1.25 km horizontal resolution. The run started at 2014-06-08, 12Z.

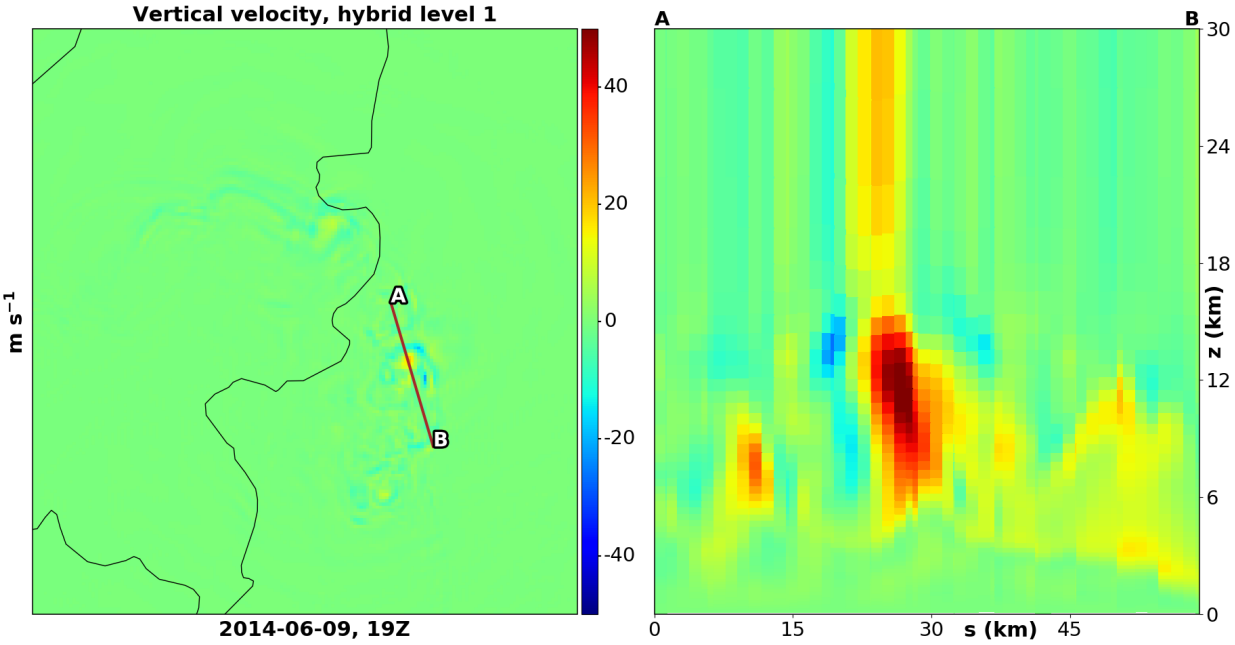

Figure 5.13: As in figure 5.12, but for the vertical velocity.

Chapter 6

Detailed analysis of simulated precipitation patterns

The discrepancies between sizes of observed and simulated areas with weak and intense precipitation, described in section 5.4, can be quantified by computing distributions of reflectivity. This was done for observed and simulated reflectivity (REF, NOHAR and NOOC configurations), and the method and results are described in section 6.1. Because distributions of simulated reflectivity might be dependent on the model's horizontal resolution, this dependency is examined in section 6.2. Section 6.3 examines vertical profiles of modelled hydrometeor contents for the REF and NOOC configuration, in order to understand the apparent differences between the reflectivity distributions for these configurations. Finally, section 6.4 discusses possible consequences and causes of the apparent differences between distributions of observed and simulated reflectivity. In addition, the potential issue of section 5.3 with initiating storms in the REF configuration is briefly touched too.

6.1 Distributions of observed and simulated reflectivity

6.1.1 Method

To calculate distributions of reflectivity, first the interval ranging from 10 to 65 dBZ was divided into bins with a width of 2.5 dBZ. Next, the area covered with reflectivities within each bin's range was computed for a given time. To create a composite picture, these areas where summed over a selectable set of dates and times (output is available hourly), giving an integrated area. This area was finally normalized by the total integrated area for reflectivities between 10 and 65 dBZ.

6.1.2 All 12 US cases

These distributions where first computed over all available US cases. The domain over the Central US was chosen instead of that over the Netherlands, because the S-band NEXRADs are much less sensitive to attenuation than the C-band radars in the Netherlands. In addition to that, the NEXRADs cover almost the entire domain over the Central US, whereas the radars in the Netherlands cover only a small part of that domain.
To first give an overview of these 12 cases, figures 6.1 - 6.3 show observed and simulated reflectivity at 6 km altitude for forecast hour 12 for all of them. These figures do already clearly show a much larger extent of regions with weak precipitation in the observations, compared to in simulations. The resulting reflectivity distributions are displayed in figure 6.4, for altitudes of 6, 8, 10 and 12 km. Lower altitudes have not been included in this composite analysis, because of the presence of the bright band.

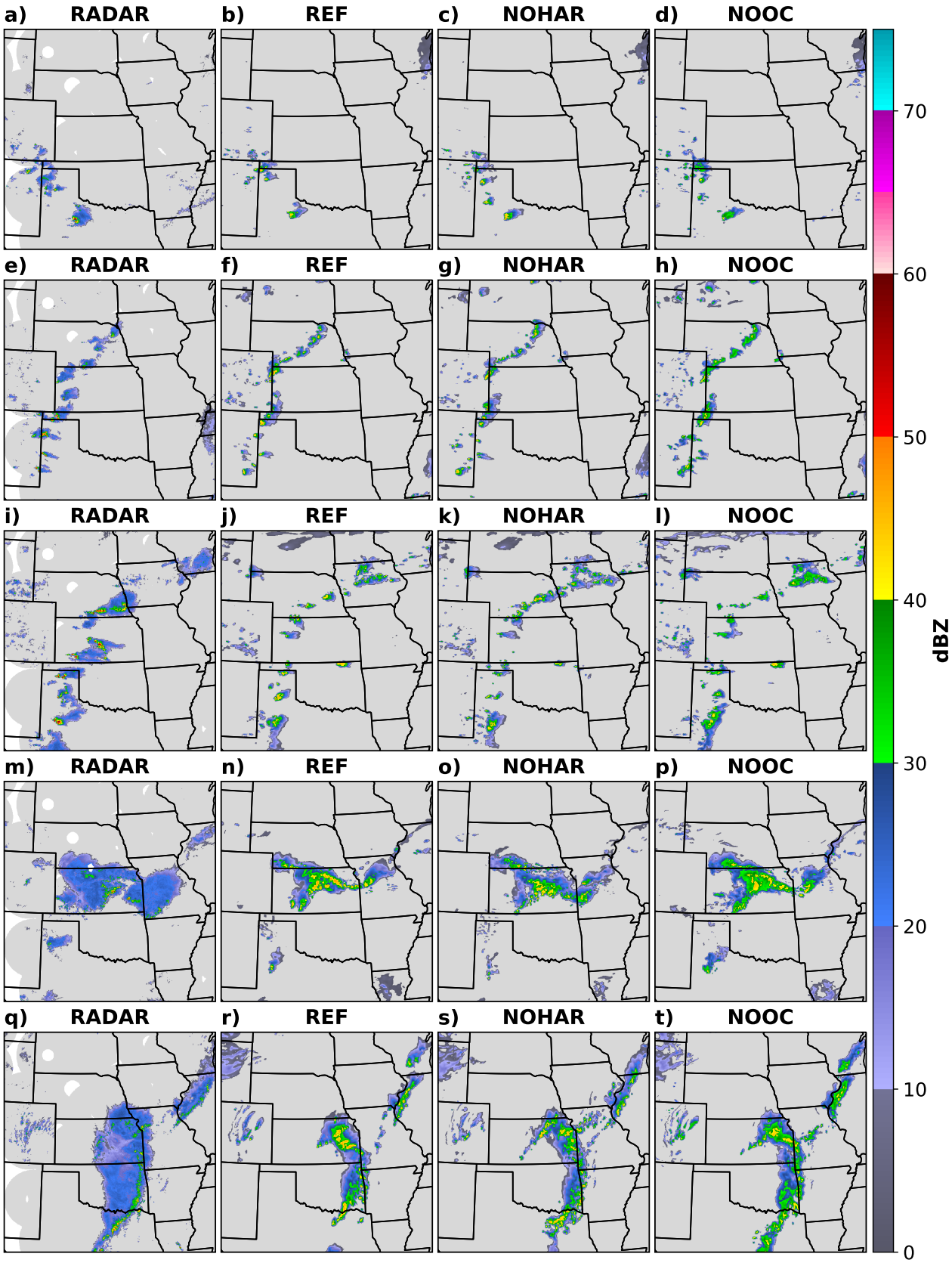

Figure 6.1: Observed and simulated reflectivity at 6 km altitude, for runs with the REF, NOHAR and NOOC configurations. Shown is the +12h forecast from runs starting at (b-d) 2019-04-27, 12Z, (f-h) 2019-05-04, 12Z, (j-l) 2019-05-05, 12Z, (n-p) 2019-05-06, 18Z, and (r-t) 2019-05-18, 06Z.

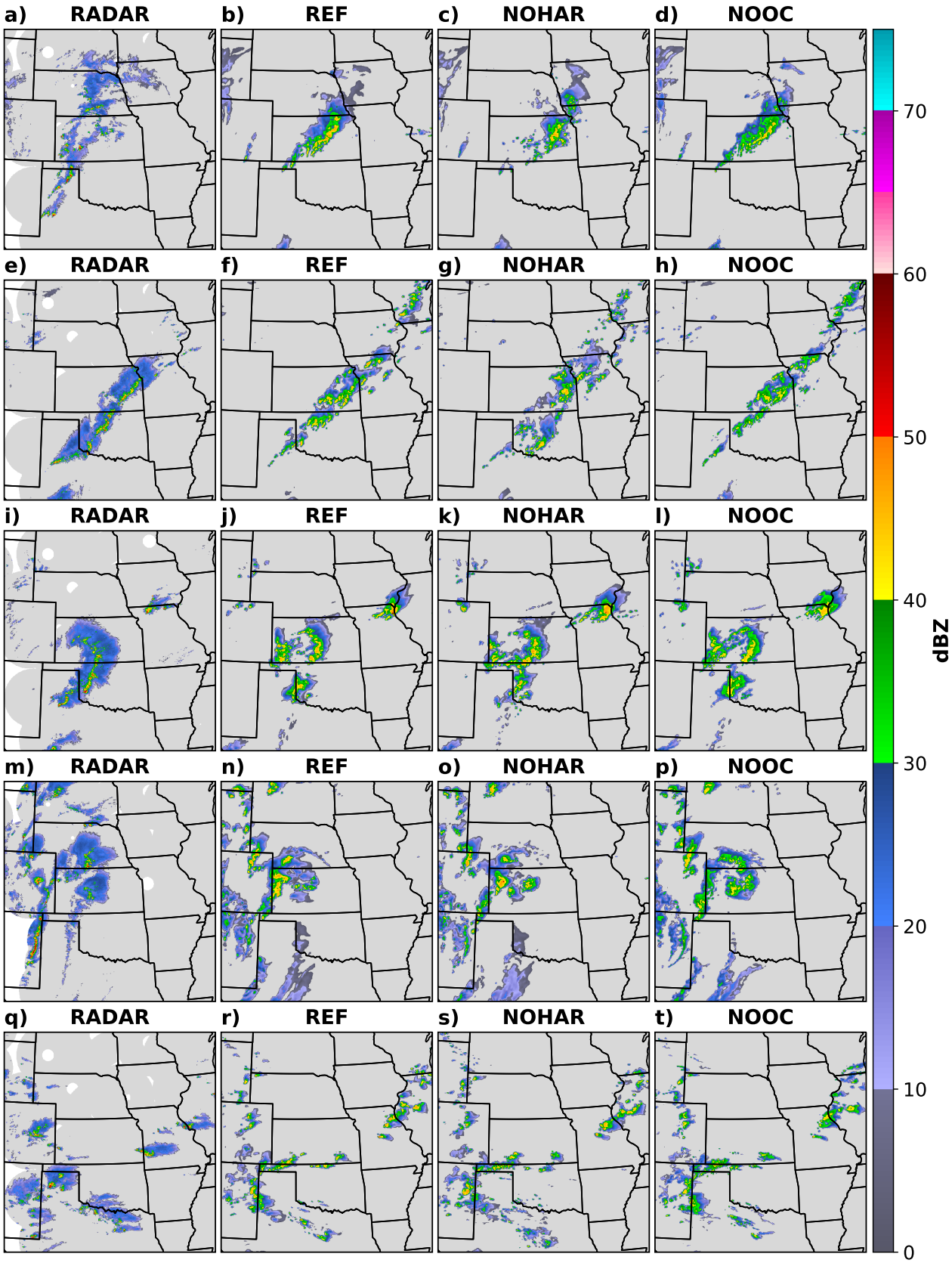

Figure 6.2: As in figure 6.1, but for (b-d) 2019-05-23, 12Z, (f-h) 2019-05-24, 12Z, (j-l) 2019-05-25, 12Z, (n-p) 2019-05-26, 12Z, and (r-t) 2019-06-01, 12Z.

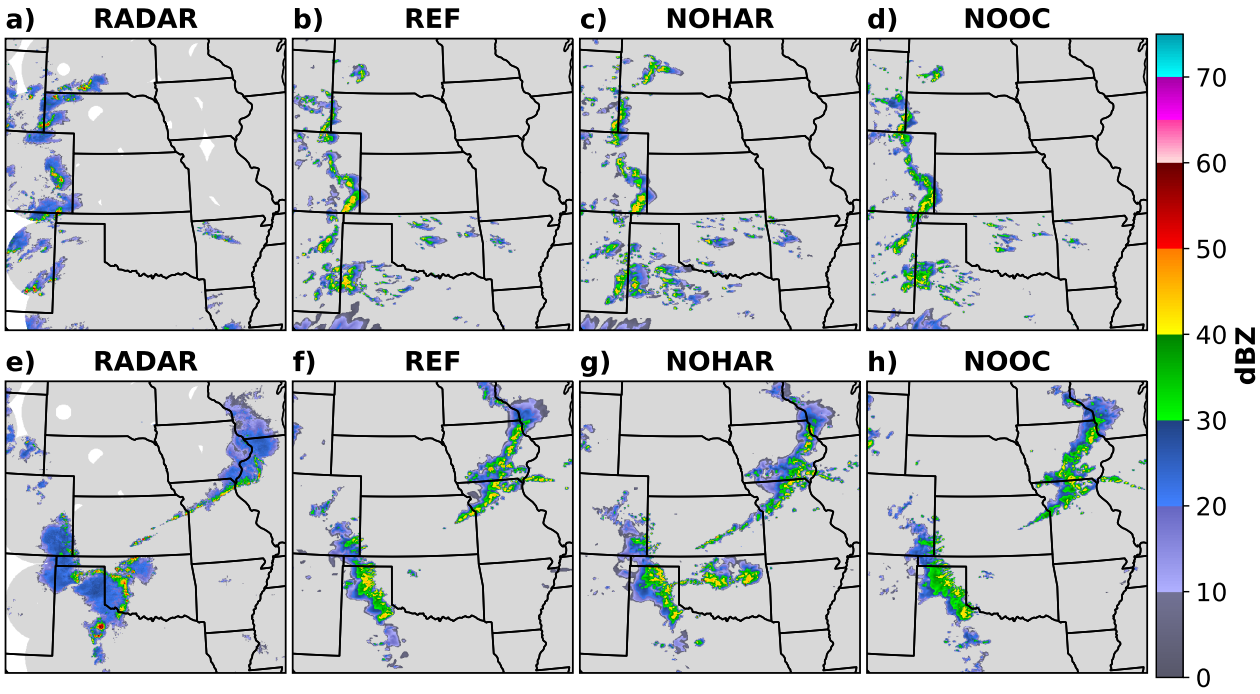

Figure 6.3: As in figure 6.1, but for (b-d) 2019-06-02, 12Z, and (f-h) 2019-06-15, 15Z.

From the normalized distributions in figure 6.4 it is clear that there is indeed a large discrepancy between distributions of observed and simulated reflectivity. Reflectivities below 30 dBZ are far more common in the observations, whereas the opposite is the case for reflectivities above 30 dBZ.

Further, observed distributions show a pronounced peak at relatively low reflectivities for all three altitudes, that moves towards lower reflectivities with increasing altitude. Inspection of figures 6.1-6.3 learns that this peak must be associated with the large areas of stratiform precipitation present below anvils of thunderstorms or thunderstorm complexes (Mesoscale Convective Systems). The fact that this relatively sharp peak is apparent in a composite analysis over 12 cases, suggests that the observed vertical profile of reflectivity in these regions of stratiform precipitation is relatively similar among these cases.
The model is clearly not able to reproduce the observed peak in the distributions, although the NOOC configuration produces a small peak for 6 km altitude, centered at about 25 dBZ. Instead, distributions of simulated reflectivity decrease almost linearly with increasing reflectivity, except for NOOC at 6 km altitude.

When we look at absolute integrated areas, we see that observed values in the peak of the distribution exceed values from the REF configuration by more than a factor 2 for 6 km altitude. On the contrary, modelled values are larger by at least a factor 2 for reflectivities above 30 dBZ. In this comparison it should be taken into account that not the whole domain is covered by radars, such that in fact actual values over the whole domain will be slightly larger.
Figure 6.5 shows total integrated reflectivity area above 10 dBZ (calculated by summing over all reflectivity bins) for 6, 8, 10 and 12 km altitude. The REF configuration substantially underestimates this area by a factor of about 1.5 for 6 km altitude (in fact even more given limited radar coverage), while for altitudes of 10 and 12 km it overestimates this area. Though for these high altitudes it should be taken into account that the vertical resolution of radar data decreases with increasing altitude, reducing the accuracy of the reflectivity composites here.

The NOHAR and NOOC configurations show larger total integrated areas than the REF configuration, indicating the influence of the turbulence and microphysics schemes. For NOHAR the differences are due to use of a different turbulence scheme, i.e. HARATU in the REF configuration. These differences suggest that more storms initiate in the NOHAR configuration, and/or that they become larger, and/or live longer.
For NOOC these differences are due to the OCND2 update to the microphysics, which has altered the distribution of hydrometeors. This effect of OCND2 is examined in section 6.3, where vertical profiles of hydrometeor contents are shown.
In the remainder of this section one case is examined in more detail, mainly to also obtain distributions at an altitude below the bright band, which for this case is at a relatively constant altitude. It is the case of 18 May 2019, when an extensive squall line formed over the states of Texas and Oklahoma.

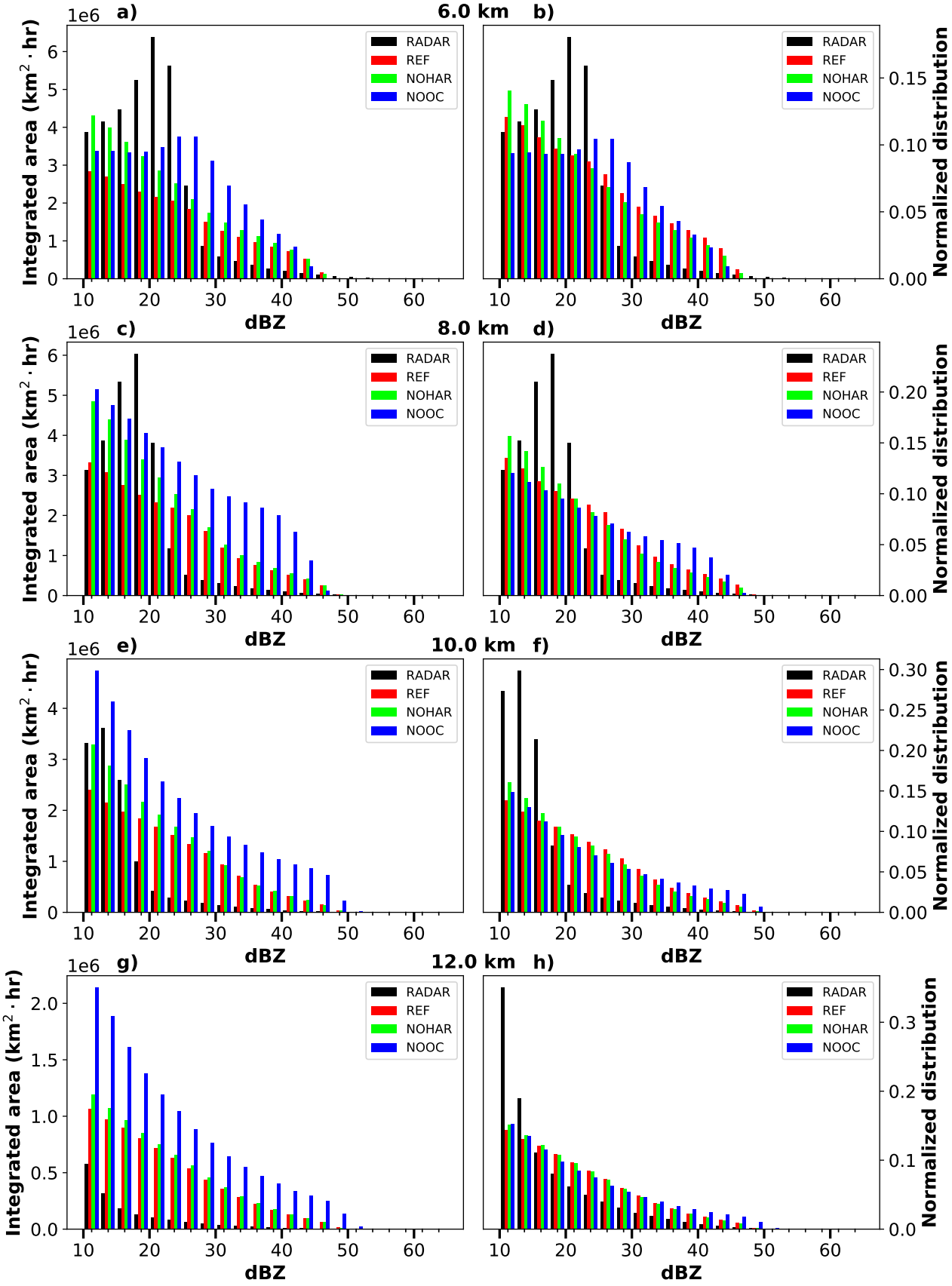

Figure 6.4: Observed and simulated distributions of integrated reflectivity area (left) over all 12 cases (using forecast hours 3-24), together with the corresponding normalized distributions (right), at (a-b) 6, (c-d) 8, (e-f) 10 and (g-h) 12 km altitude. For each case, hours 3-24 of the simulations where included.

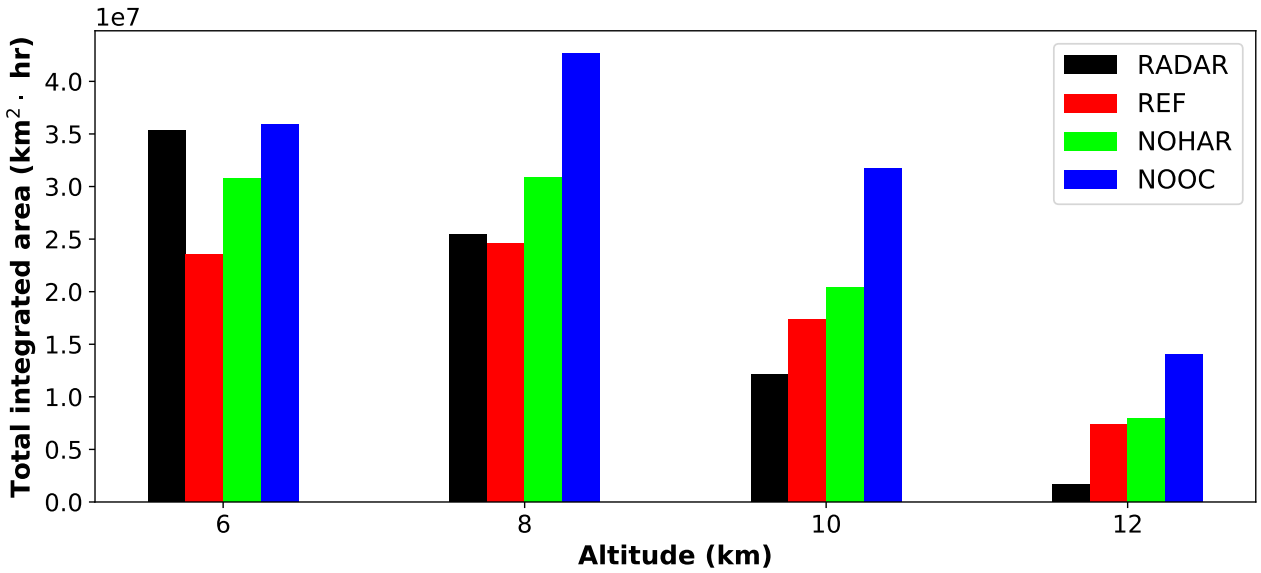

Figure 6.5: Total integrated reflectivity area above 10 dBZ for altitudes of 6, 8, 10 and 12 km.

6.1.3 Squall line of 18 May 2019

On 18 May 2019 an extensive squall line formed over Texas and Oklahoma, which continued on the next day. Figure 6.6 shows the evolution of the squall line, and displays observed and simulated reflectivity (REF and NOOC) at forecast hours 3, 10 and 18, for altitudes of 2 and 6 km. NOHAR is not included, because the focus here is specifically on the normalized distributions reflectivity distributions, which are very similar for NOHAR and REF based on figure 6.4.
In order to calculate these distributions for only the squall line, and not for other areas of precipitation within the domain (in regions with varying freezing levels, and thus varying altitudes of the bright band), the domain considered for calculating these distributions was made dependent on the forecast hour. It was taken to be a rectangular area that encompassed mainly the squall line, and that moved with the squall line to the east in time, increasing in size. Forecast hours 3-18 were included. Thereafter discrepancies in evolution of the squall line became quite large between model and observations, with observations showing more rapid weakening than model runs. Inside the domains considered, the freezing level was located around 4 km altitude. It was therefore deemed safe to compute distributions for 2 km altitude, without much contamination by the presence of the bright band. It should however be noted that radar coverage is relatively scarce for 2 km altitude, limiting the accuracy of distributions of observed reflectivity to some extent.

Figure 6.7 shows the resulting normalized distributions of integrated reflectivity area for altitudes of 2, 6, 9 and 12 km. For 2 km altitude there are substantial differences between 20 and 50 dBZ, with the model underestimating the occurrence of reflectivities between 20 and 35 dBZ, and overestimating it between 35 and 50 dBZ. Above 50 dBZ the model again underestimates the occurrence, but these reflectivities are relatively uncommon. But as they represent the intense storm cores, they might be considered important to simulate.
For 6 km altitude the differences between model and observations become much larger, and then remain fairly similar for 9 km. For 12 km altitude the model performs better, though there is a pronounced peak in the distribution of observed reflectivity around 10 dBZ, which is not visible in the model distributions.
The pronounced peaks of figure 6.4 in the distributions of observed reflectivity are also present in figure 6.7, where the additional distributions for 2 km altitude further confirm that this peak shifts to higher reflectivities with decreasing altitude. This peak is associated with the extensive area of stratiform precipitation behind the leading edge of the squall line.

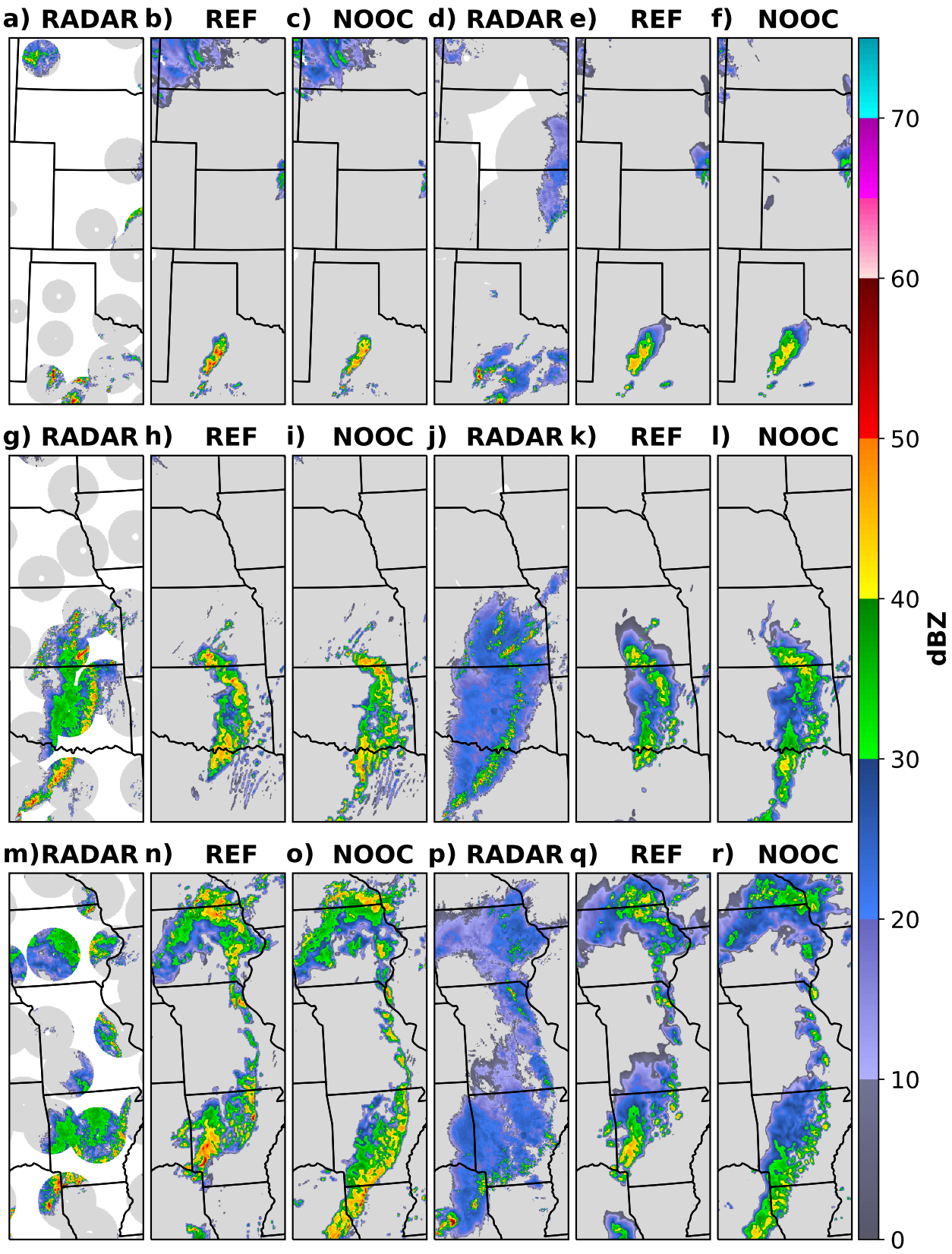

Figure 6.6: Observed and simulated reflectivity for the squall line of 18 May 2019 for forecast hours 3 (a-f), 10 (g-i) and 18 (m-r), with runs starting at 06Z. Columns 1-3 show reflectivities at 2 km altitude, and columns 4-6 at 6 km.

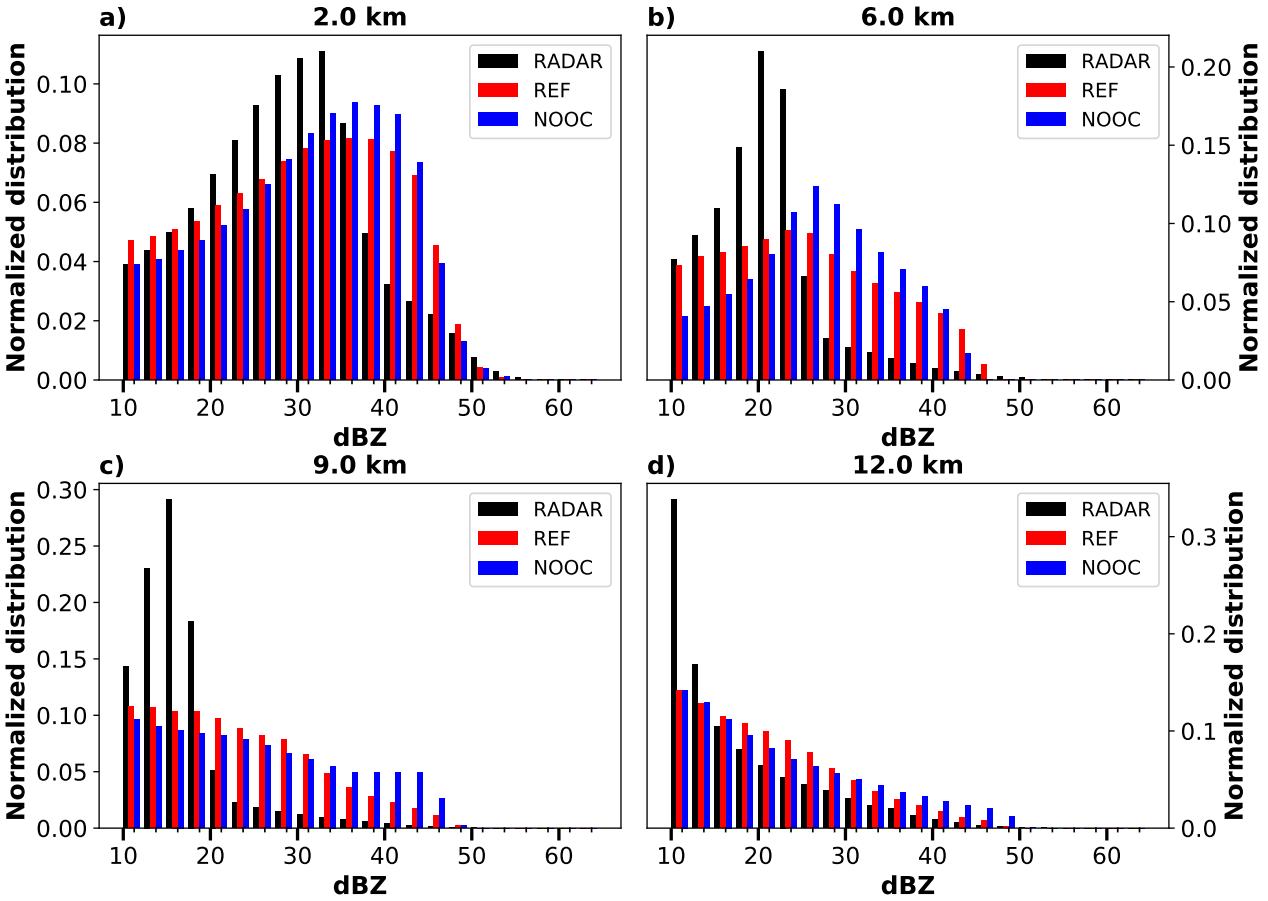

Figure 6.7: Normalized distributions of integrated reflectivity area for a squall line at 18 May 2019, at altitudes of 2, 6, 9 and 12 km. Based on forecast hours 3-18 froms runs starting at 06Z.

6.2 Influence of horizontal resolution

One might expect some dependence of the reflectivity distributions on the model's horizontal resolution, because a higher horizontal resolution might allow the model to better resolve the most intense precipitation cores. To examine whether there is indeed such a dependency on resolution, the REF configuration was run at 2.5, 1.25 and 1.0 km horizontal resolution. This was done for 29 May 2018, a case in the Netherlands.
To give an overview of this case, figure 6.8 shows simulated reflectivity at 2 and 6 km altitude for three forecast hours, for the runs at 2.5 and 1.0 km resolution. The corresponding normalized distributions of integrated reflectivity area are shown in figure 6.9. It is clear that the model's horizontal resolution has very little effect on the distributions of simulated reflectivity.

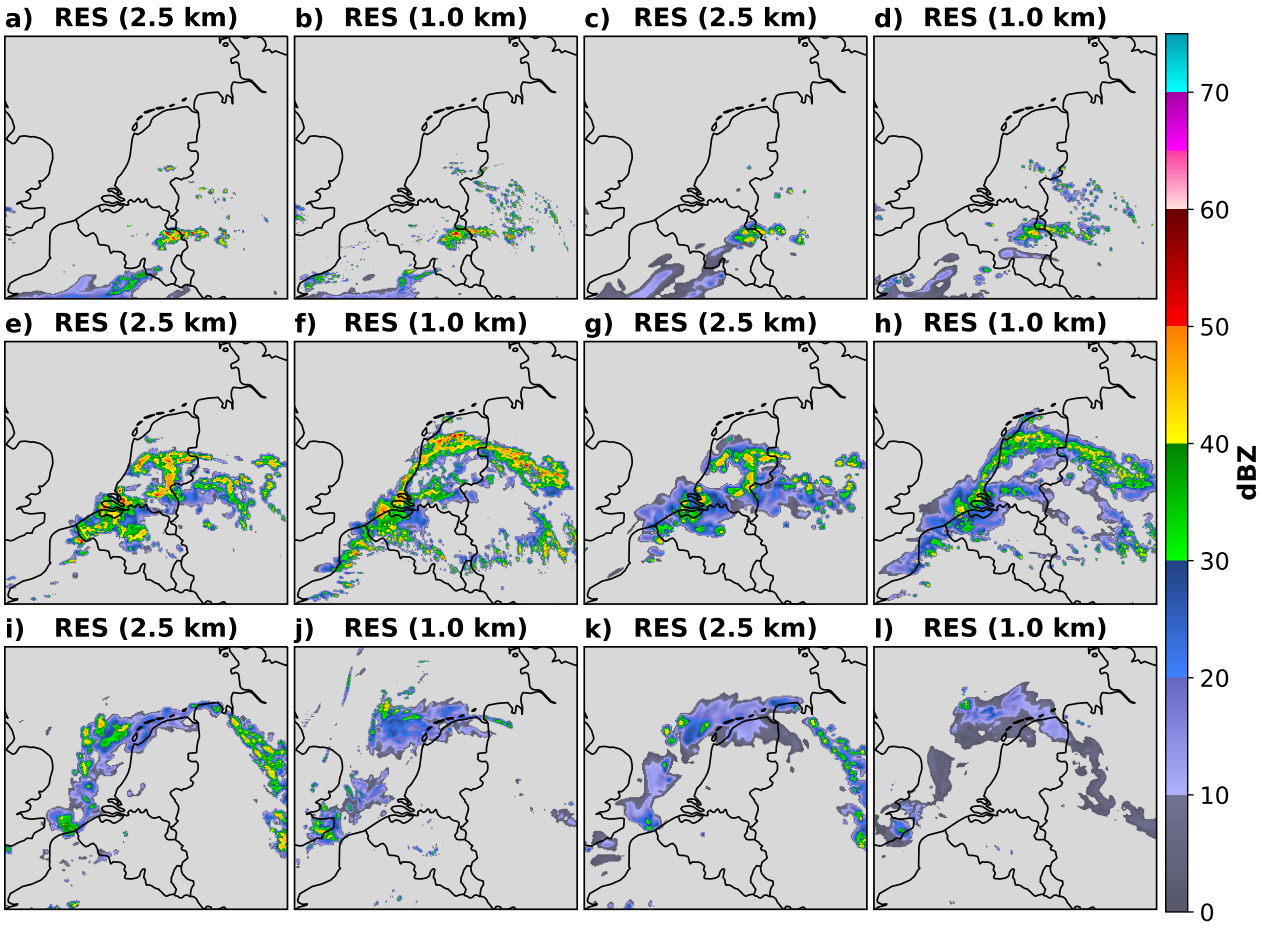

Figure 6.8: Simulated reflectivity at 2 (columns 1-2) and 6 (columns 3-4) km altitude for 29 May 2018 from runs with the REF configuration at 2.5 and 1.0 km horizontal resolution, for forecast hour (a-d) 7, (e-h) 11 and (i-l) 16. Runs started at 06Z.

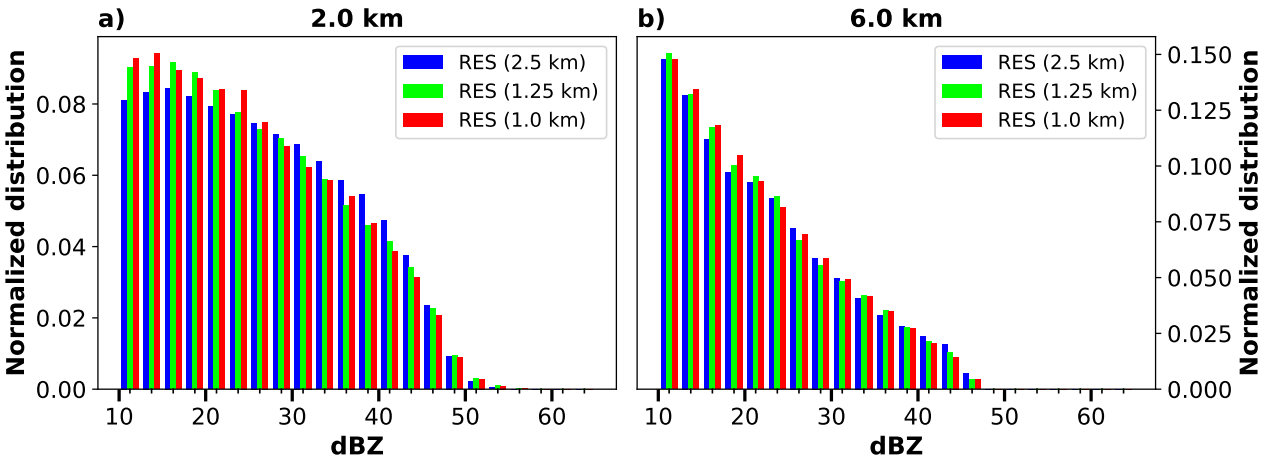

Figure 6.9: Normalized distributions of integrated reflectivity area for 29 May 2018 at altitudes of 2 and 6 km, from runs with the REF configuration at 2.5, 1.25 and 1.0 km horizontal resolution. Based on forecast hours 4-18 from runs starting at 06Z.

6.3 Vertical profiles of modelled hydrometeor contents

In order to understand the differences between the reflectivity distributions for the REF and NOOC configurations, vertical profiles of hydrometeor contents have been calculated for the squall line case of 18 May 2019. Figure 6.10 shows vertical profiles of integrated (in space and time) hydrometeor mass (per meter in the vertical) for both configurations, for rain, snow, graupel and cloud ice. Especially for snow and cloud ice there are very pronounced differences. Apparently the old microphysics scheme (without the OCND2 update) generates much more snow and cloud ice, and in general more precipitating particles, given that the NOOC configuration produced more rain.
Figure 6.11 shows vertical profiles of maximum (over space and time) hydrometeor contents for both configurations, which are representative for the most intense storms. Compared to the integrated hydrometeor masses in figure 6.10, these profiles of maximum hydrometeor content show a smaller difference between both configurations for snow, whereas for graupel the difference has become much larger. Further, rain is observed at higher altitudes in the REF configuration, up to about 7.5 km. This is far above the freezing level, indicating that the OCND2 update results in more liquid water above the freezing level, presumably in the strong updrafts of the intense storms that produce the maximum hydrometeor contents.

Based on these results it seems that the differences between the reflectivity distributions for the REF and NOOC configurations are mainly caused by the production of much more cloud ice in NOOC, which results in the production of about twice as much snow than in REF, and also more precipitation in general.

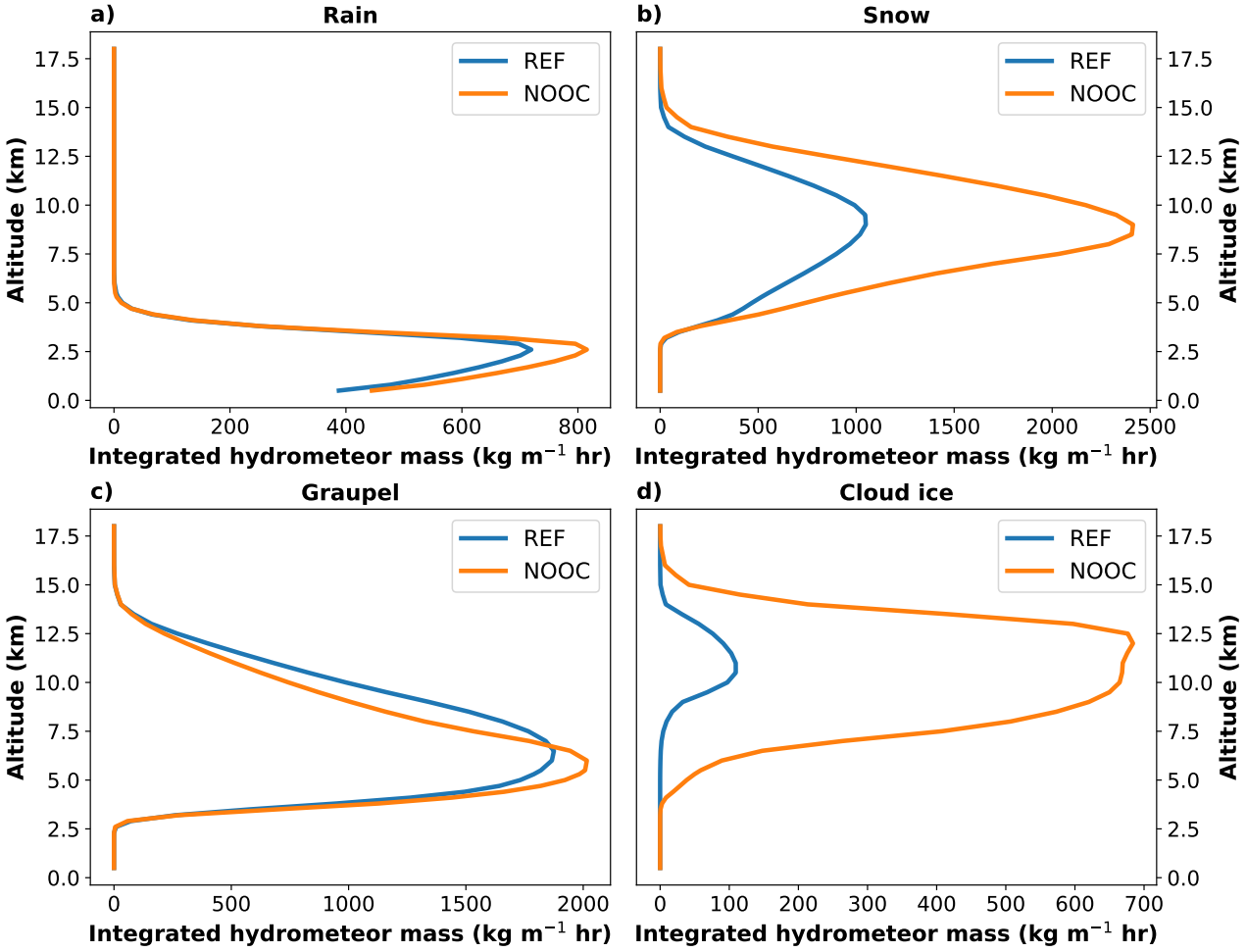

Figure 6.10: Integrated (both in space and time) hydrometeor mass (per meter in the vertical) for the squall line of 18 May 2019, for rain, snow, graupel and cloud ice. Integration in time is performed over forecast hours 3-18, and in space over the variable domain described in section 6.1.3.

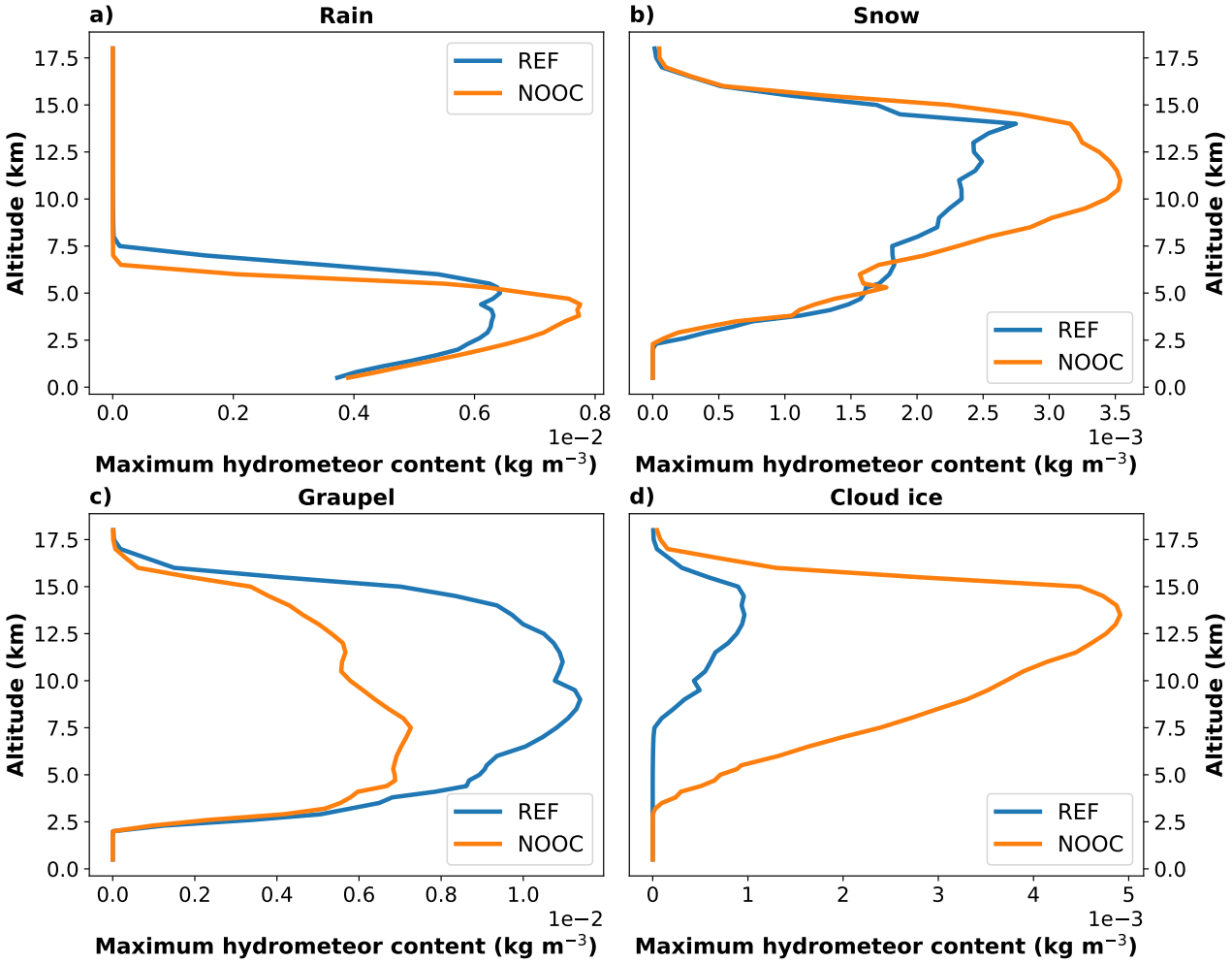

Figure 6.11: Maximum hydrometeor content over space and time for the squall line of 18 May 2019, using the same domain as for figure 6.10.

6.4 Discussion

The analysis of reflectivity distributions in section 6.1 has shown large differences between model and observations. While distributions of observed reflectivity show a large peak for relatively low reflectivities, this peak is absent in distributions of simulated reflectivity. The exception is the NOOC configuration at 6 km altitude, that does show a small peak. Inspection of radar composites for the 12 cases that contributed to the distributions has learned that the peak in the observations is associated with large areas of stratiform precipitation, below anvils of thunderstorms or thunderstorm complexes. These areas apparently have a fairly similar vertical profile of reflectivity, and appear to be simulated badly by the model.
Related to missing the peak in the distribution of observed reflectivity is the overestimation of the occurrence of higher reflectivities. The distributions of both absolute and normalized time-integrated reflectivity area show overestimation of the occurrence of these reflectivities by at least a factor 2.
Calculation of total integrated reflectivity areas showed that the REF configuration substantially underestimated this at 6 km altitude, by a factor of at least 1.5. The other configurations performed better at this altitude, although the opposite is the case for altitudes of 8, 10 and 12 km, where these total integrated reflectivity areas were overestimated by all configurations (except for REF at 8 km).
Comparing the model configurations between themselves shows that the REF configuration produces the smallest total integrated reflectivity areas.

Regarding the cause of these differences, section 6.2 showed that horizontal resolution has very little effect on the distributions of simulated reflectivity, indicating that improvement on this issue should mainly come from improvement of the microphysics. Section 6.3 showed that there are pronounced differences between vertical profiles of hydrometeor contents for the REF and NOOC configurations, expecially for cloud ice and snow. These differences are responsible for the differences in the distributions of reflectivity between REF and NOOC, apparent in figures 6.4 and 6.7.

The remainder of this section discusses the consequences of these findings for both the issues described in sections 5.3 and 5.4. For the issue of section 5.4, which was focused on in this chapter, potential causes and options for improvement are described too.

6.4.1 Too small (large) areas with weak (intense) precipitation

The results in this chapter have clearly shown that the model underestimates the areas covered by weak, stratiform precipitation produced by thunderstorms and thunderstorm complexes, and overestimates the areas covered by intense precipitation. In addition, the currently operationally used REF configuration also substantially underestimates the total area covered by precipitation at the lowest considered altitude of 6 km, as is apparent when comparing total integrated reflectivity areas.
Given that precipitation influences temperature and moisture by processes such as condensation and evaporation (and many ice-involving processes), these fields will be influenced by the deficiencies in the microphysics of the model. And indirectly therefore also the pressure and wind fields, because these are related to the temperature and moisture fields. In this way the precipitation fields influence the structure of the atmosphere and its evolution, which is for instance important for the evolution of the thunderstorms that produce the precipitation, and for formation of new storms. A correct representation of precipitation fields in thunderstorms is therefore important, and improvement of the microphysics is desired.

Fan et al. (2017) and Han et al. (2019) performed an intercomparison study of a squall line event over the state of Oklahoma and surroundings in detail, and considered in particular the convective updrafts (Part I, Fan et al.) and stratiform precipitation properties (Part II, Han et al.). They ran the Weather Research and Forecasting (WRF) model at 1 km resolution with eight different cloud microphysics schemes to investigate processes that contribute to the large variability in simulated cloud and precipitation properties. Similar to our findings, they found a wider area of high reflectivity (defined by them as $Z_e > 45$ dBZ) than observed and a much narrower stratiform area. Corresponding plots of observed and simulated reflectivity are shown in figure 6.12.

In an attempt to understand these results they analysed many different aspects of the simulated convection, and compared these with observations when available. These aspects include surface rain rates, ice (IWC) and rain (RWC) water contents and updraft velocities and areas.
Han et al. (2019) found that the majority of simulations overestimate IWC above 7 km altitude but underestimate IWC right above the melting level, which leads to underestimation of RWC below 3 km altitude because melting is the primary source of stratiform RWC. They concluded that the overestimation of IWC at upper levels may be related to detrainment that is too high as a result of overestimated convective intensity, found by Fan et al. (2017), especially since IWC magnitudes correspond well with convective condensate detrainment fluxes. They also concluded that underestimated IWC just above the melting level could also be related to simulated convective updrafts that are too intense, which detrain condensate and water vapor too high at upper levels, increasing the probability that ice particles will excessively sublimate before reaching the melting level.
Based on these and other results they concluded that the magnitude and variability of stratiform precipitation among schemes are ultimately related to the magnitude and variability of ice particle mass fluxes above the melting level. They stated that these fluxes are significantly impacted by the kinematic and microphysical properties of convective regions, which are the primary source for ice in the stratiform region, while local ice growth processes in the stratiform region play a secondary role in model spread. Based on this they concluded that accurate simulation of convective regions is critical to better simulating stratiform precipitation.
They also found that the only single-moment scheme used in their intercomparison, has the largest overestimation of convective intensity and the largest underestimation of stratiform precipitation area and total stratiform precipitation among all the schemes. Based on that they concluded that increasing the complexity of the microphysics scheme from single-moment to double-moment, where also the total number concentration of at least some hydrometeor species is predicted, clearly helps to improve model performance.

As mentioned above, for the convective regions Fan et al. (2017) found that the model overestimates vertical velocity in updrafts. They also found that the model underestimates the area of updrafts at upper levels.

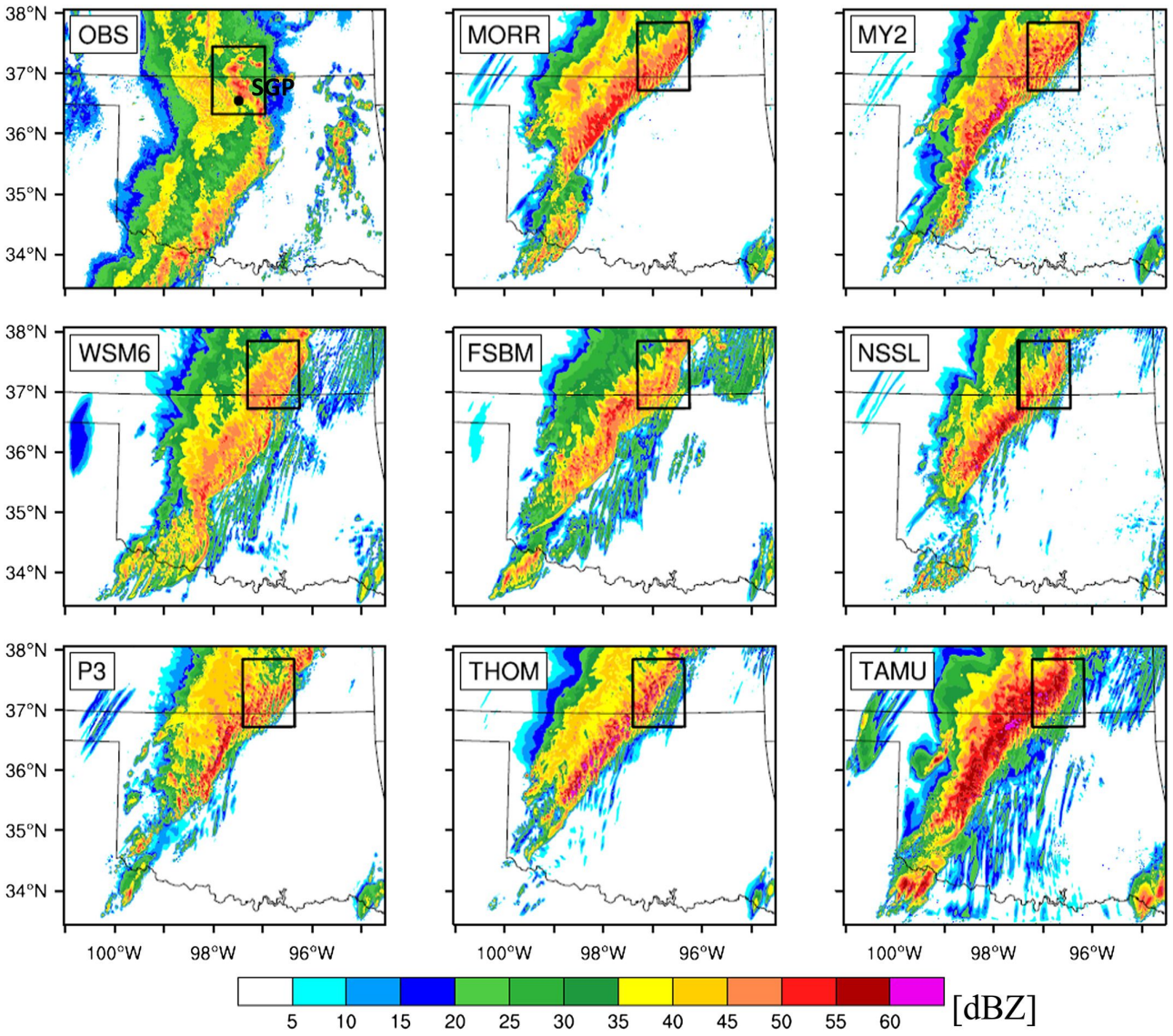

Figure 6.12: Spatial distribution of composite reflectivity for NEXRAD data at 1100 UTC and simulations at 1000 UTC. From Fan et al. (2017).

Based on the results of this intercomparison study it seems that some improvement of HARMONIE on this issue should come from moving from the current single-moment to a double-moment microphysics scheme, where also the total number concentration of hydrometeors is predicted. This would come at the price of increased computational cost. Another major conclusion of this study is that further improvement should come for a large part from a better representation of the convective regions within thunderstorms. This should indirectly improve the vertical profiles of ice water content, which were found to be very important for the magnitude and variability of stratiform precipitation.
If we focus purely on the two microphysics configurations considered in this research, i.e. those with (REF) and without (NOOC) the OCND2 update, it is clear from the results in this chapter that they both produce too large areas with intense precipitation and too small areas with weak precipitation. The main differences between the simulated precipitation fields are the production of substantially more precipitation by NOOC, and the simulation of a (larger) peak in the normalized reflectivity distributions by NOOC at lower altitudes. The latter difference is in favour of NOOC, as observations show a clear peak in the distributions, which is however located at lower reflectivities. The former difference is in favour of REF, especially at high altitudes, as NOOC greatly overestimates the total integrated reflectivity areas at these altitudes.

6.4.2 No initiation of severe thunderstorms in certain cases under HARATU

Results in this chapter showed that the NOHAR configuration produced larger integrated reflectivity areas than the REF configuration, over the 12 US cases considered. Figure 6.4 shows that this result is valid for almost every reflectivity bin, although differences are largest for low reflectivities, indicating that NOHAR mainly produces more weak precipitation. As stated in section 6.1.2, the production of larger integrated reflectivity

areas indicates that more storms initiate in NOHAR and/or they become larger and/or live longer. The cases studied in section 5.3 suggest that at least the first option is true, but as stated in that section, this issue requires further investigation.

Chapter 7

Conclusions

The performance of the high-resolution weather model HARMONIE on simulating convective storms has been evaluated in this study. This was done by comparing (simulated) three-dimensional fields of radar reflectivity and (simulated) satellite images for multiple cases with convective storms. Four different main model configurations where considered, which are named REF, NOHAR, NOOC and NOSHAL. These represent resp. the reference or current model configuration, REF with old turbulence scheme (no HARATU), REF without OCND2 update to microphysics, and REF with shallow convection scheme disabled.
A total of 11 cases was considered over a domain covering the Netherlands and surroundings, and an additional 12 cases were considered over a domain covering the Central United States. This latter domain was added because of issues with radar beam attenuation for the C-band precipitation radars in the Netherlands, which is only a minor issue for the S-band radars in the US.

A result of the evaluation is an overview of five (potential) issues that are currently present in the model, which expanded the overview provided by Tijm (2018). These issues are:

1. A large underestimation of the number of shallow showers in e.g. cases with shallow cold air outbreaks over the North Sea.

2. A too linear structure of simulated shallow showers when they get simulated after disabling the shallow convection scheme.

3. Lacking initiation of severe thunderstorms under the new turbulence scheme HARATU, whereas they are observed in reality and get simulated when using the old CBR turbulence scheme.

4. The simulation of too small areas with weak precipitation and too large areas with intense precipitation.

5. When run at a higher resolution of 1.25 km, there is a case for which precipitation in a severe thunderstorm reaches the model top.

Three of these issues have been analysed in (slightly) more detail. In the case of issue 1 it was already shown by Tijm (2018) that disabling the shallow convection scheme leads to the formation of much more shallow showers. Here we showed that the effect of the shallow convection scheme is to reduce near-surface dew points and to increase temperature at the top of the boundary layer due to more vertical mixing, by analysing box-averaged skew-T log-P diagrams. Both these effects are unfavourable for the initiation of convection, and might together explain the large influence of the shallow convection scheme on initiating shallow showers.

Issue 3 was also mentioned by Tijm (2018), and has here been analysed in slightly more detail. Establishment of this issue is however still based on only a few case studies, and a more detailed examination of whether there is in general a problem with initiating convection under HARATU has yet to be performed. For this reason this issue is listed as a potential issue.
Box-averaged skew-T log-P diagrams were plotted for one particular case with lacking initiation of a severe thunderstorm under HARATU. It was found that the HARATU turbulence scheme produces more vertical mixing at the top of the boundary layer, leading to a slightly drier boundary layer and slightly steeper temperature lapse rates just above the boundary layer. The former effect is positive for initiation of convection, whereas the latter is negative.

Finally, an extensive analysis of precipitation patterns was performed in order to quantify issue 4. This was done by calculating distributions of (normalized) integrated reflectivity area over all 12 US cases over, using reflectivity bins with a width of 2.5 dBZ over the interval from 10 to 65 dBZ. Altitudes of 6, 8, 10 and 12

km were considered. Lower altitudes were excluded because distributions of observed reflectivity would be contaminated by the presence of the bright band.
Results showed large differences between distributions of observed and simulated reflectivity. Whereas distributions of observed reflectivity show a large peak for relatively low reflectivities between 10 and 30 dBZ, such a peak is (almost) absent for simulated reflectivities. This peak appears to be associated with large areas of stratiform precipitation below the anvils of thunderstorms. Related to the underestimation of the occurrence of low reflectivities is the overestimation of the occurrence of higher reflectivities, by at least a factor 2.
Calculation of total integrated reflectivity areas (within the 10-65 dBZ interval) showed that these were underestimated by at least a factor of 1.5 for the REF configuration at 6 km altitude. On the other hand, substantial overestimation occurs at altitudes of 10 and 12 km.

Running the REF configuration at three different horizontal resolutions of 2.5, 1.25 and 1 km showed that resolution has very little impact on the distributions of reflectivity. This indicates that improving simulated reflectivity distributions should mainly come from improvement of the microphysics.
Based on an intercomparison study performed by Fan et al. (2017) and Han et al. (2019), who considered the influence of eight different cloud microphysics schemes on simulating convective updrafts and stratiform precipitation, it seems that improvement of the microphysics should mainly come from moving to a double-moment scheme and from a better representation of convective regions within thunderstorms.

Bibliography

[1] Bengtsson, L., Andrae, U., Aspelien, T., Batrak, Y., Calvo, J., de Rooy, W., Gleeson, E., Hansen-Sass, B., Homleid, M., Hortal, M., Ivarsson, K.-I., Lenderink, G., Niemelä, S., Nielsen, K. P., Onvlee, J., Rontu, L., Samuelsson, P., Muñoz, D. S., Subias, A., Tijm, S., Toll, V., Yang, X., and Ødegaard Køltzow, M. (2017): The HARMONIE-AROME model configuration in the ALADIN-HIRLAM NWP system, *Monthly Weather Review*, 145, 1919-1935.

[2] Caniaux, G., 1993: Paramétrisation de la glace dans un modèle non-hydrostatique de nuage: Application à une ligne de grain tropicale. Thèse de Doctorat de l'Université Paul-Sabatier, 257 pp.

[3] Caumont, O., Ducrocq V., Delrieu G., Gosset M., Pinty J.-P., Parent du Châtelet J., Andrieu H., Lemaître Y., Scialom G., 2006: A radar simulator for high-resolution non-hydrostatic models. *J. Atmos. Oceanic Technol.*, 20, 1049-1067.

[4] Cuxart, J., P. Bougeault, and J.-L. Redelsperger, 2000: A turbulence scheme allowing for mesoscale and large-eddy simulations. *Quart. J. Roy. Meteor. Soc.*, 126, 1-30.

[5] Doviak, R. J., D. S. Zrnić, 1993: Doppler Radar and Weather Observations, second edition. *Academic Press*, 562 pp.

[6] Fan, J., et al. (2017), Cloud-resolving model intercomparison of an MC3E squall line case: Part I - Convective updrafts, *Quart. J. Roy. Meteor. Soc.*, 122, 9351-9378.

[7] Han, B., Fan, J., Varble, A., Morrison, H., Williams, C. R., Chen, B., et al. (2019). Cloud-resolving model intercomparison of an MC3E squall line case: Part II. Stratiform precipitation properties. *Quart. J. Roy. Meteor. Soc.*, 124.

[8] Homeyer, C. R., and K. P. Bowman, 2017: Algorithm Description Document for Version 3.1 of the Three-Dimensional Gridded NEXRAD WSR-88D Radar (GridRad) Dataset. Retrieved from `http://gridrad.org/pdf/GridRad-v3.1-Algorithm-Description.pdf`.

[9] Kessler, E., 1969: On the Distribution and Continuity of Water Substance in Atmospheric Circulation. *Meteor. Monogr.*, No. 32, Amer. Meteor. Soc., 84 pp.

[10] Khairoutdinov, M., and Y. Kogan, 2000: A new cloud physics parameterization in a large-eddy simulation model of marine stratocumulus. *Mon. Wea. Rev.*, 128, 229-243.

[11] Langston, C., J. Zhang and K. Howard, 2007: Four-dimensional dynamic radar mosiac. *J. Atmos. Oceanic Technol.*, 24, 776-790.

[12] Lascaux, F., E. Richard, and J.-P. Pinty, 2006: Numerical simulations of three different MAP IOPs and the associated microphysical processes. *Quart. J. Roy. Meteor. Soc.*, 132, 1907-1926.

[13] Lenderink, G., and A. Holtslag, 2004: An updated length-scale formulation for turbulent mixing in clear and cloudy boundary layers. *Quart. J. Roy. Meteor. Soc.*, 130, 3405-3427.

[14] Marshall, J. S., and K. L. S. Gunn, 1952: Measurement of snow parameters by radar. *J. Meteor.*, 9, 322-327.

[15] Mascart, P. J., and P. Bougeault, 2011: The Meso-NH atmospheric simulation system: Scientific documentation. Part III: Physics. Météo-France Tech. Rep., 153 pp.

[16] Melnikov, V. M., and D. S. Zrnić, 2007: Autocorrelation and crosscorrelation estimators of polarimetric variables. *J. Atmos. Oceanic Technol.*, 24, 13371350.

[17] Müller, M., and Coauthors, 2017: AROME-MetCoOp: A Nordic convective-scale operational weather prediction model. *Wea. Forecasting*, 32, 609-627.

[18] Pinty, J.-P., and P. Jabouille, 1998: A mixed-phase cloud parameterization for use in a mesoscale non-hydrostatic model: Simulations of a squall line and of orographic precipitation. *Preprints, Conf. on Cloud Physics*, Everett, WA, Americ. Meteor. Soc., 217-220.

[19] de Rooy, W. C., 2014: The fog above sea problem: Part 1 analysis. *ALADIN-HIRLAM Newsletter*, No. 2, Mto-France, Centre National de Recerches Meteorologiques, Toulouse, France, 9-15.

[20] de Rooy, W. C., and H. de Vries, 2017: Harmonie verification and evaluation. HIRLAM Tech. Rep. 70, 79 pp.

[21] Seity, Y., Brousseau, P., Malardel, S., Hello, G., Bénard, P., Bouttier, F., Lac, C. and Masson, V. (2011), The AROME-France convective-scale operational model. *Monthly Weather Review*, 139(3), 976-991. Preprints, *Conf. on Cloud Physics*, Everett, WA, Amer. Meteor. Soc., 217-220.

[22] Shelton, M. L., 2009: Hydroclimatology: perspectives and applications. *Cambridge University Press*, 426 pp.

[23] Smith, P. L., 1984: Equivalent radar reflectivity factors for snow and ice particles. *J. Climate Appl. Meteor.*, 23, 1258-1260.

[24] Tang, L., J. Zhang, C. Langston, J. Krause, K. Howard, and V. Lakshmanan, 2014. A physically based precipitation-nonprecipitation radar echo classifier using polarimetric and environmental data in a realtime national system. *Weather and Forecasting*, 29, 1106-1119.

[25] Tijm, S., 2018: Forecast model progress. ALADIN-HIRLAM meeting 2018, `http://www.umr-cnrm.fr/aladin/IMG/pdf/20180417_fm_tijm.pdf`.

[26] Yuter, S. E., 2002: 'Precipitation radar'. Pp. 1833-1852 in Encyclopedia of Atmospheric Sciences. Ed. J. R. Holton, J. A. Curry and J. A. Pyle. Academic Press, London, UK.

[27] Zhang J., K. Howard, and J. J. Gourley, 2005: Constructing three-dimensional multiple radar reflectivity mosaics: Examples of convective storms and stratiform rain echoes. *J. Atmos. Oceanic Technol.*, 22, 30-42.

Appendix A: Warm and cold microphysical processes parameterized in HARMONIE

Table 1: Mechanism and description for all warm (top) and cold (bottom) processes in ICE3 that involve a conversion of hydrometeor species. Subscript letters refer to the hydrometeor classes listed in the caption of figure 2.5. Adapted from Mascart and Bougeault (2011).

Mechanism	Description
$r_v \Longrightarrow r_c$	Condensation on cloud droplets (CON)
$r_c + r_c \Longrightarrow r_r$	Autoconversion of cloud droplets (AUT)
$r_c + r_r \Longrightarrow r_r$	Accretion of cloud droplets by raindrops (ACC)
$r_r \Longrightarrow r_v$	Evaporation of rain droplets (EVA)
$r_v + r_r \Longrightarrow r_r$	Condensation on rain droplets (CND)
$r_v \Longrightarrow r_i$	Heterogneous nucleation (HEN)
$r_c \Longrightarrow r_i$	Homogeneous nucleation (HON)
$r_r \Longrightarrow r_g$	Homogeneous nucleation (HON)
$r_c \Longrightarrow r_i$	Bergeron-Findeisen effect (BER)
$r_v + r_i \Longrightarrow r_i$	Deposition (DEP)
$r_v + r_s \Longrightarrow r_s$	Deposition (DEP)
$r_v + r_g \Longrightarrow r_g$	Deposition (DEP)
$r_i \Longrightarrow r_v$	Sublimation (SUB)
$r_s \Longrightarrow r_v$	Sublimation (SUB)
$r_g \Longrightarrow r_v$	Sublimation (SUB)
$r_i + r_i \Longrightarrow r_s$	Autoconversion of pristine ice (AUT)
$r_i \Longrightarrow r_s$	Aggregation of pristine ice (AGG)
$r_i + r_r \Longrightarrow r_g$	Raindrops contact freezing (CFR)
$r_c + r_s \Longrightarrow r_s$	Light riming of aggregates (RIM)
$r_c + r_s \Longrightarrow r_g$	Heavy riming of aggregates (RIM)
$r_r + r_s \Longrightarrow r_s$	Accretion of rain and aggregates (ACC)
$r_r + r_s \Longrightarrow r_g$	Accretion of rain and aggregates (ACC)
$r_c + r_g \Longrightarrow r_g$	Dry growth of graupels (DRY)
$r_i + r_g \Longrightarrow r_g$	Dry growth of graupels (DRY)
$r_r + r_g \Longrightarrow r_g$	Dry growth of graupels (DRY)
$r_s + r_g \Longrightarrow r_g$	Dry growth of graupels (DRY)
$r_c + (r_g) \Longrightarrow r_r$	Partial freezing & water shedding (SHD)
$r_r + (r_g) \Longrightarrow r_g$	Partial freezing & water shedding (SHD)
$r_i + r_g \Longrightarrow r_g$	Wet growth of graupels (WET)
$r_s + r_g \Longrightarrow r_g$	Wet growth of graupels (WET)
$r_i \Longrightarrow r_c$	Melting (MLT)
$r_g \Longrightarrow r_r$	Melting (MLT)
$r_s \Longrightarrow r_g$	Conversion melting (CVM)

Appendix B: Quality-control algorithm for NEXRAD data

Quality control (QC) of NEXRAD data is necessary to remove nonprecipitation echoes. Tang et al. (2014) developed a physically based QC algorithm, that uses a set of six rules to classify echoes as either precipitation (P) or nonprecipitation (NP). Though this algorithm is used as a source of inspiration, it has for speed of implementation been decided to create a new QC algorithm for this project. This new algorithm uses three rules for P-NP classification, and is based on the following four quantities:

- Correlation Coefficient (CC): A measure of the consistency of the shapes and sizes of targets within the resolution volume. Values range from 0 to 1, with higher values indicate higher consistency (Melnikov and Zrnić, 2007).
- Differential reflectivity (ZDR): Base 10 logarithm of the ratio of horizontally polarized reflectivity (equivalent reflectivity factor) to the vertically polarized reflectivity. Positive values indicate that the dominant hydrometeors are larger in the horizontal (Melnikov and Zrnić, 2007).
- Echo top height (ET): Height (above radar level) of the highest scan for which $Z_e > 18.5$ dBZ.
- Top height of lowest echo (ETL): Echo top height of the lowest echo at each grid cell, defined here as a vertically continuous region of reflectivities of at least 0 dBZ. It is used instead of the normal echo top height to 'detect' NP echoes below regions of precipitation higher in the atmosphere.
  To calculate it, first reflectivities are mapped onto a common horizontal polar grid, after which the algorithm iterates through all scans in the upward direction. In these iterations it first checks whether any reflectivity in lower scans exceeds 0 dBZ, and if true, then it checks whether the condition $Z_e \geq 0$ dBZ is still satisfied. If not, ETL is reached at the scan below.
  Sometimes however echoes gradually transform from NP to P, without the termination criterion $Z_e \leq 0$ dBZ being satisfied anywhere inbetween. For this reason an additional criterion is added to determine that ETL is reached at scan i: If $CC[i] - CC[i-1] > 0.1$, $ET > 4$ km and $Z_e[i-1] < 10$ dBZ, then ETL is reached at scan $i-1$. This criterion is based on the increase in CC that is usually observed when going from NP to P echoes, with the last two conditions checking whether the echoes below are NP (usually less than 10 dBZ at their top), and that there are P echoes located above ($ET > 4$ km).

Based on these four quantities, the following four rules have been defined for NP classification:

1. $CC < 0.95$, as in Tang et al. (2014). This simple rule is the basis for P-NP distinction, and is based on the observation that NP echoes usually have a relatively low correlation coefficient.
2. $ETL < 4$ km. This rule is based on the observation that NP echoes are usually confined to the lowest 4 km AGL. Thus $ETL > 4$ km usually indicates precipitation.
   If the highest scan does not reach 4 km above radar level, the requirement changes to $ETL < h(i_{max} - 1)$, where $i_{max} - 1$ is the index of the second highest scan and $h(i_{max} - 1)$ the corresponding beam altitude above radar level. This prevents removal of P echoes that do extend above 4 km, but that are within the radar's cone of silence.
3. $ZDR > 4$ dBZ & $Z < 30$ dBZ. This rule is based on the observation that $ZDR > 4$ dBZ does not occur or barely occurs for P echoes with $Z_e < 30$ dBZ, indicating that the echoes are probably NP.

These three rules are combined in the following way to arrive at the final NP classification:

NP = ((1 & 2) | 3) & ($h < 4$km).

The condition $h < 4$ km implies that only echoes below 4 km above radar level can get removed. Conditions 1 and 2 are combined because $CC < 0.95$ can also occur for P echoes, for instance in a bright band, in regions with large hail or regions with non-uniform beam filling. If however also $ETL < 4$ km, it becomes very likely that echoes are NP.

An example of composite reflectivity before and after applying the QC algorithm is shown in figure 1. Most NP echoes are removed in figure 1b), although at least one area remains in eastern Texas. Examination of three-dimensional reflectivity learns that here P echoes are located above NP echoes, without a region with $Z_e < 10$ dBZ in between. This causes the routine that calculates ETL to fail to distinguish the overlying P echoes from the underlying NP echoes. Occurrence of this is however uncommon, so this should not lead to severe amounts of NP echoes that not get removed.

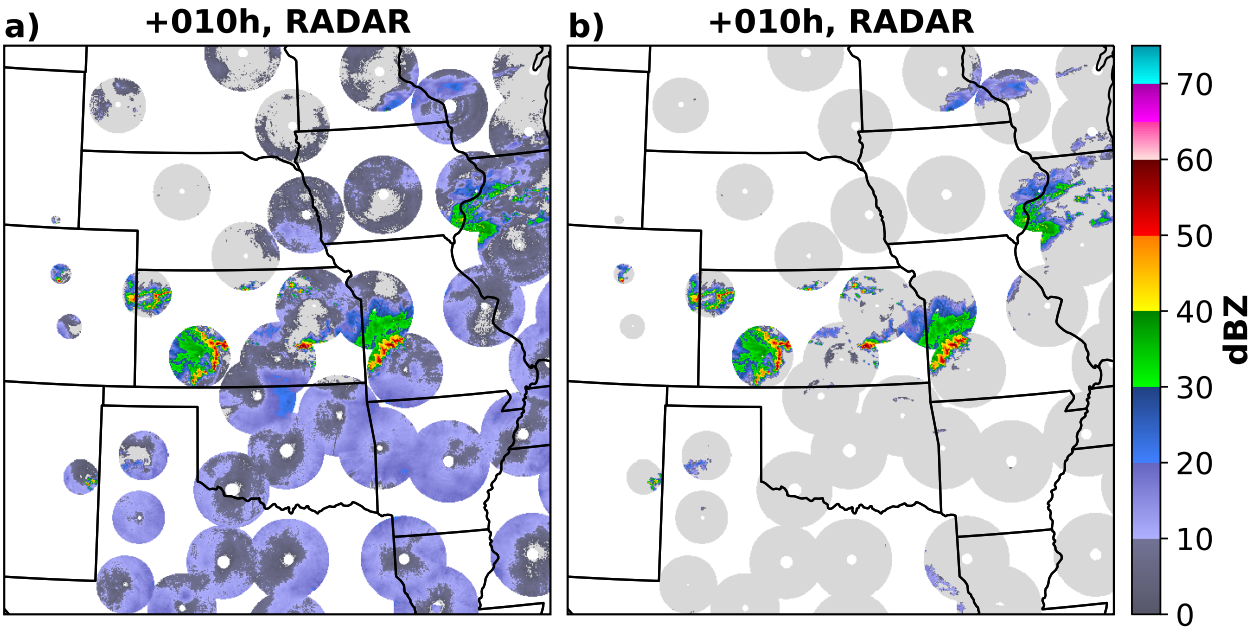

Figure 1: Composite reflectivity at 2 km altitude before (a) and after (b) applying the quality-control algorithm.